Studies of One-Dimensional Carbon-Based Metals: AC_{60} and Carbon Nanotubes

by

James Curtis Hone

B. S. (Yale University) 1990
M. S. (University of California at Berkeley) 1994

A dissertation submitted in partial satisfaction of the requirements for the degree of

Doctor of Philosophy
in

Physics

in the

GRADUATE DIVISION

of the

UNIVERSITY OF CALIFORNIA, BERKELEY

Committee in charge:

Professor Alex Zettl, Chair
Professor Paul McEuen
Professor Paul Alivisatos

Fall 1998

Studies of One-Dimensional Carbon-Based Metals: AC_{60} and Carbon Nanotubes

by

James Curtis Hone

The dissertation of James Curtis Hone is approved:

Chair _____ Date 7/14/98

_____ Date 7/28/98

_____ Date 7/30/98

University of California, Berkeley
Fall 1998

Abstract

Studies of One-Dimensional Carbon-Based Metals: AC_{60} and Carbon Nanotubes

by

James Curtis Hone

Doctor of Philosophy in Physics

University of California, Berkeley

Professor Alex Zettl, Chair

This thesis describes studies of two carbon-based metals, AC_{60} and carbon nanotubes. AC_{60} is an alkali metal (A = K, Rb, or Cs) fullerene intercalation compound, in which the C_{60} molecules polymerize into linear chains. Carbon nanotubes are single or multiple graphene sheets wrapped into cylindrical tubes with diameters varying from one to tens of nm, and lengths of up to a few microns. Because of their structures, both materials have significantly reduced dimensionality. The AC_{60} materials have a quasi-1D electronic structure, and the Rb and Cs compounds display a low-temperature antiferromagnetic ordering which is likely related to this low dimensionality. Nanotubes are true 1-D electronic systems because of their small radii: the circumferential component of the electron wavevector is quantized. In fact, the small diameter of nanotubes also affects their phonon spectrum: they also have a 1-D phonon structure at low temperature.

The first part of this thesis deals with the AC_{60} materials. Chapter 1 gives an introduction to fullerenes in general and AC_{60} in particular. Chapter 2 describes the synthesis of AC_{60} crystals in our laboratory, and their characterization using x-ray diffraction and

transmission electron microscopy. Chapter 3 describes electrical and thermal transport measurements of AC_{60}. These measurements include temperature-dependent resistivity under zero and applied pressure; magnetoresistance; constant-volume resistivity; resistivity of mixed-intercalant species; and thermopower. Chapter 4 is an x-ray diffraction study of the structure of the AC_{60} materials at high pressure in a diamond anvil cell.

The second part of this thesis deals with carbon nanotubes. Chapter 5 is an introduction to their structural and electronic properties. Chapter 6 is a study of the thermopower of single-walled nanotubes (SWNT's). The thermopower of as-grown SWNT's is measured and interpreted according to a number of models. The behavior of the thermopower of SWNT's at high temperature and the thermopower of acid-treated and Br-intercalated SWNT's are described. Chapter 7 is a study of the thermal conductivity of nanotubes. The magnitude of the thermal conductivity of a single tube is inferred from the thermal conductivity of bulk samples, and the temperature-dependence of the thermal conductivity is modeled using Boltzmann transport theory, taking the low dimensionality of the nanotubes into account explicitly. Chapter 8 describes the alkali-metal intercalation of individual SWNT bundles.

Finally, two appendices have been included in the thesis. The first describes techniques developed in the Zettl lab for the measurement of thermopower and thermal conductivity. The second describes the synthesis of ^{13}C-enriched C_{60} from amorphous ^{13}C powder.

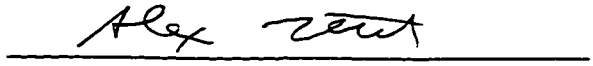

Contents

Chapter 5.

Chapter 6.

Chapter 7.

Chapter 8.

Appendix A.

Appendix B.

Figures

Chapter 1.

Introduction to Fullerenes and Polymerized AC_{60}.

1.1 Discovery and Synthesis of C_{60}.

The discovery of fullerenes, a third class of all-carbon materials, has sparked a tremendous amount of research into their electronic, chemical, and structural properties. Fullerenes were originally observed by Richard Smalley and collaborators at Rice University, who discovered peaks in the mass-spectrum of the soot from laser-ablated graphite[1]; in 1985[2] it was proposed that the peaks were due to closed-cage carbon structures, which were termed fullerenes. The most common fullerene, and the only one that will be discussed in this thesis, is C_{60}, consisting of 60 carbon atoms in a nearly spherical shell approximately 7Å in diameter.

Intensive research into the properties of fullerenes and fullerene-based materials was made possible by the discovery by Krätschmer *et al.*[3] of techniques for the bulk synthesis and purification of C_{60} and other fullerenes. In the Krätschmer-Huffman technique, fullerenes are created in the plasma of a carbon arc discharge. Their apparatus has been duplicated in our laboratory and used for the synthesis of numerous materials, including fullerenes, nanotubes, and non-carbon nanotubes.

Figure 1.1 shows the apparatus used for the synthesis of C_{60} in the Zettl laboratory. A graphite rod (usually 1/4" in diameter, obtained from Poco Graphite), is attached to a water-cooled copper anode inside a water-cooled chamber filled with helium. A cathode,

usually also made of graphite, is fed in from the other side. A high-current power supply, attached to the anode and cathode, provides a dc current (typically 100 A) when the two are touched. When the anode and cathode are moved apart slightly, a high-temperature plasma arc forms between the two. This arc is maintained by adjusting the size of the gap (usually 2-5 mm for production of C_{60}) between the anode and cathode. After the anode is consumed, the chamber is opened and soot collected from the walls.

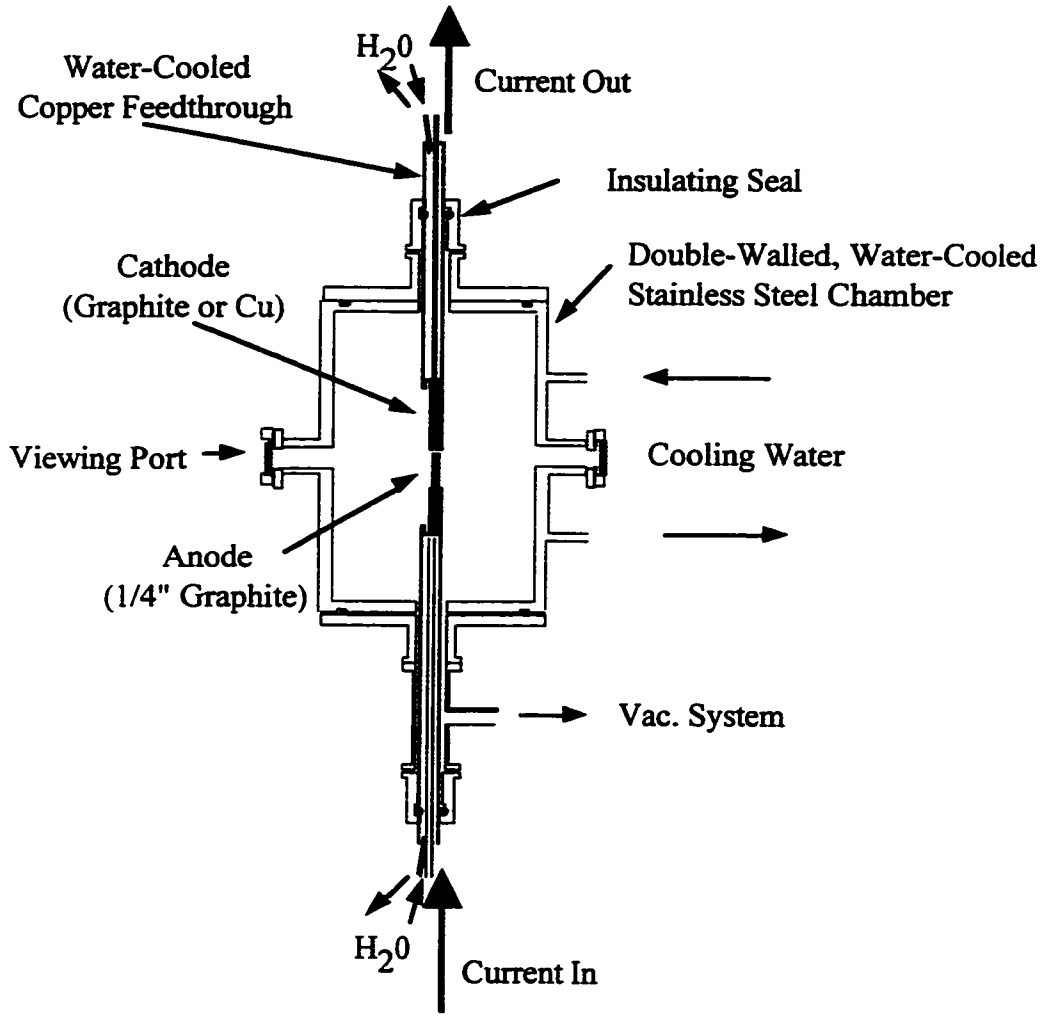

Figure 1.1. Arc-discharge apparatus for the synthesis of fullerenes

C_{60} is purified from the fullerene-containing soot by a two-step process. C_{60} and higher fullerenes such as C_{70} are soluble in a number of solvents, such as toluene, and therefore can be removed by sonicating the soot in toluene and filtering the suspension. The toluene and dissolved fullerenes pass through the filter, yielding a solution which has a burgundy color. Alternatively, a solvent reflux system can be used; this system extracts a higher proportion of fullerenes from the soot and uses less solvent. The second step in the purification of individual fullerene species uses column chromatography to separate species of different masses. C_{60}, the smallest species, passes through the column most quickly, and produces a solution which is a purple color. The next species, C_{70}, can be seen as a redder solution. C_{60} powder is then collected by evaporation of the solvent from the C_{60} solution.

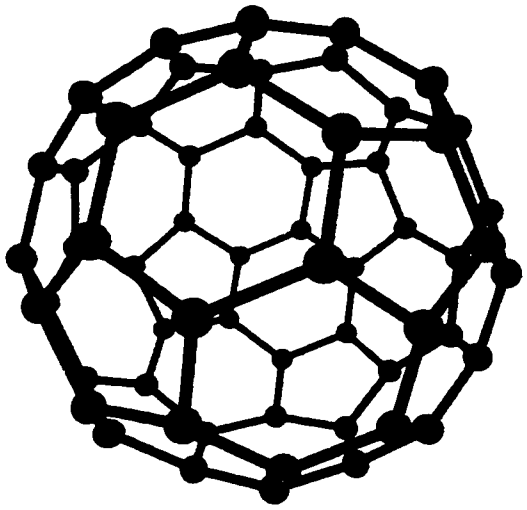

Figure 1.2. Structure of the C_{60} molecule

1.2 Structure of C_{60}: Molecule and Solid Fullerite[4]

Figure 1.2 depicts a single molecule of C_{60}. As discussed earlier, it is highly spherical, with a diameter of 7Å. The closed structure is obtained by the addition of pentagons to a hexagonal graphene sheet. A closed molecule is required to have 12 pentagons; C_{60} is the smallest possible fullerene[5] in which each pentagon is bordered only by hexagons (an example of the so-called isolated pentagon rule), of which it contains 20. C_{60} has the highest discrete point group symmetry possible, with 120 elements in the icosahedral I_h point group. Although it was originally expected that C_{60} would be highly unreactive, this is not the case, due to the curvature-induced admixture of sp^2 and sp^3 bonding between neighboring carbon atoms. There are now a large number of chemical species which can be attached to C_{60}.

C_{60} in its purified form forms a molecular crystal, with neighboring balls Van der Walls bonded, in contrast to the strong on-ball covalent bonding. These crystals can be synthesized by a number of methods, including the vapor transport method used in our lab and described in section 3.2. At room temperature, these crystals have an FCC crystal structure, with a lattice constant of 14.2 Å. The nearest-neighbor distance in this structure is 10 Å; the balls are separated by a distance of 3 Å, close to the graphite interlayer spacing of 3.35 Å. The exact room-temperature structure of crystalline C_{60} was a matter of some debate for a time, because it was difficult to determine the relative orientations of the individual molecules. X-ray diffraction (XRD), nuclear magnetic resonance (NMR), theoretical, and other studies have since provided conclusive evidence that the balls rotate in a nearly free manner at temperatures above about 260 K Below 260 K, crystalline C_{60}

undergoes a first-order orientational-ordering transition, with a concurrent change in the crystal symmetry to simple cubic and a decrease in the lattice constant of 0.049 Å. In the low-temperature phase, the C_{60} molecules are still not completely fixed, but instead 'ratchet' between preferred positions, in which the electron-rich double bonds of adjoining hexagons are 'nested' in the electron-poor pentagonal faces of neighboring molecules.

Electronically, C_{60} fullerite is a semiconductor. Its valence band is derived from the highest-occupied molecular orbitals (HOMO), while the conduction band, located 1.5 eV above the valence band, is formed from the lowest-unoccupied molecular orbitals (LUMO). Because of the weak interaction between neighboring C_{60} molecules, both of these bands are highly flat, and thus display a high density of states.

1.3 Intercalation of C_{60}: the Fullerides[4]

Because of the large size of the C_{60} molecule and the large spacing between the molecules, there exist large empty spaces in the C_{60} lattice. There are three major sites per C_{60} molecule: one octahedrally-coordinated site and two tetrahedral sites, with radii of 2.1 and 1.1 Å respectively. These sites can accommodate a large variety of intercalant atoms and molecules. Of particular interest to the physics community have been the A_xC_{60} materials, formed by intercalation of alkali metals (Na, K, Rb, Cs) into the C_{60} lattice. The alkali atoms donate electrons into the LUMO band of the C_{60} crystal, resulting in drastic changes in its electronic properties. For K, Rb, and Cs, there are four distinct line phases: those with x = 1,3,4, and 6 (the x=2 phase has been reported only for Na). The A_4 and A_6 materials are insulators. In 1991, Hebard and coworkers[6] reported the dis-

covery of superconductivity at 18 K in thin films of K-doped C_{60}; it was soon discovered that the superconducting phase corresponded to metallic K_3C_{60}; superconductivity in Rb_3C_{60} was discovered soon after. A great deal of work has been done on the superconducting A_3C_{60} family, which comprises K_3C_{60} (T_c = 19.8 K), Rb_3C_{60} (T_c = 30.8 K), Cs_3C_{60}(T_c = 40 K), and a large number of species with mixtures of K, Rb, Cs, and Na, as well as inert intercalants such as ammonia. Figure 1.3 shows the crystal structure of the different A_xC_{60} phases.

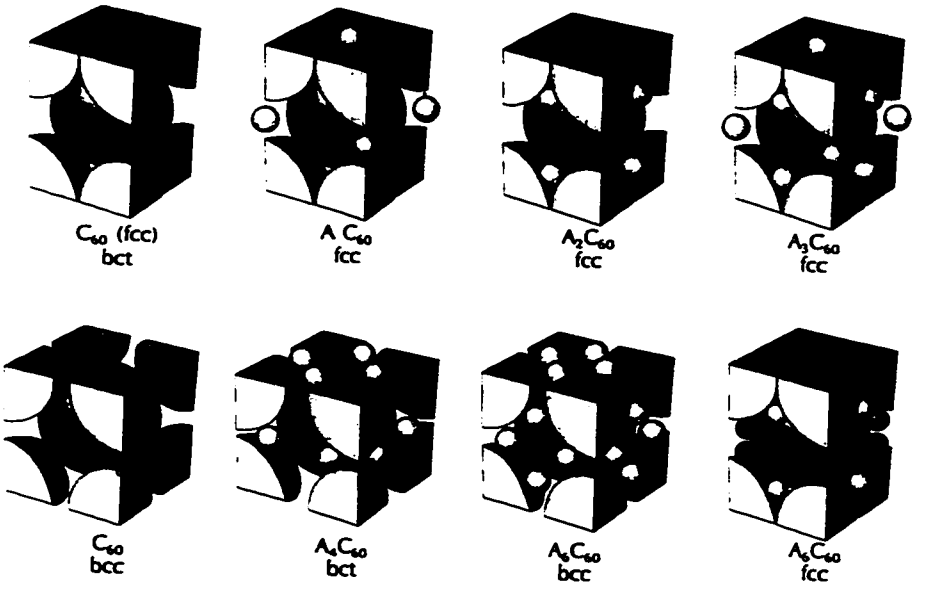

Figure 1.3. Crystal structure of A_xC_{60}.[4]

1.4 The AC_{60} Phase

It was nearly two years after the original discovery of A_3C_{60} that another stable metallic phase of alkali-doped C_{60} was discovered[7]. This material, with the stoichiometry A_1C_{60}, has proved to have a rich phase diagram and electronic structure[8], which is dia-

grammed in figure 1.4. At high temperature (above ~80 °C), the AC_{60} phase has an FCC rocksalt structure[9-11], with the alkali ions occupying the octahedral sites of the C_{60} lattice. Upon cooling, AC_{60} can undergo a number of different structural phase transitions. When cooled quickly to room temperature, the material forms a metastable dimer phase. When slow-cooled, however, AC_{60} forms an orthorhombic phase in which the C_{60} molecules polymerize into long chains. The o-AC_{60} polymer phase is the subject of the experimental work detailed in this thesis.

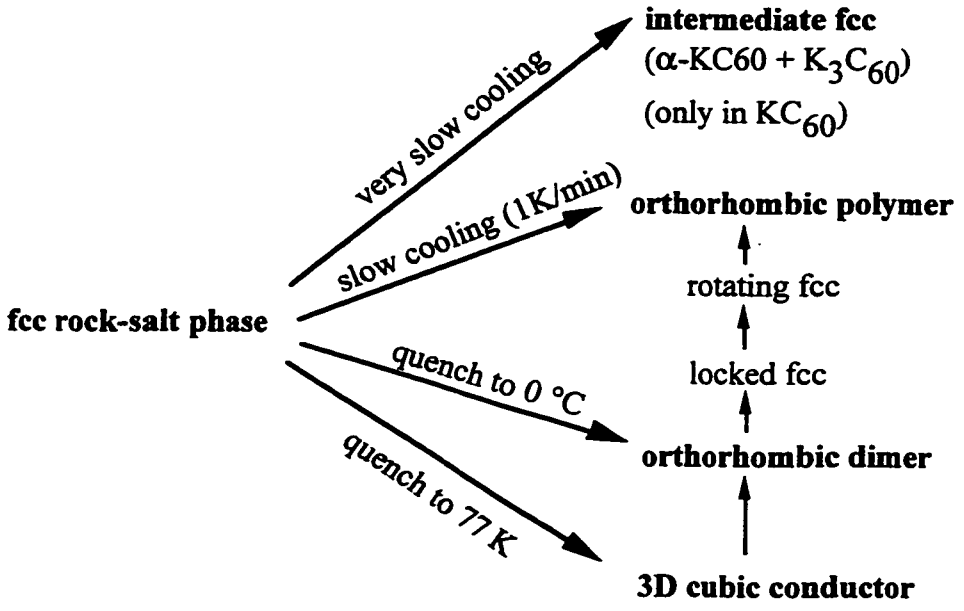

Figure 1.4. Structural phases of AC_{60}.[8]

Polymeric AC_{60} is remarkable in a number of ways. First, although C_{60} had been observed to polymerize upon exposure to light (photopolymerization), AC_{60} was the first instance of fullerene polymerization due to alkali intercalation. The family of fullerene polymers is now known to be quite diverse, comprising both linear and 2-d polymers[12],

with polymerization occurring due to exposure to light, application of high temperature and pressure, and intercalation. Second, the AC_{60} polymer phase is the only alkali-fulleride which is stable in air[13] and solvents such as toluene, a property we exploited to synthesize phase-pure material. Third, the linear polymer structure of o-AC_{60} creates the possibility of a highly anisotropic electronic structure[10].

1.5 Structure of the AC_{60} Polymer

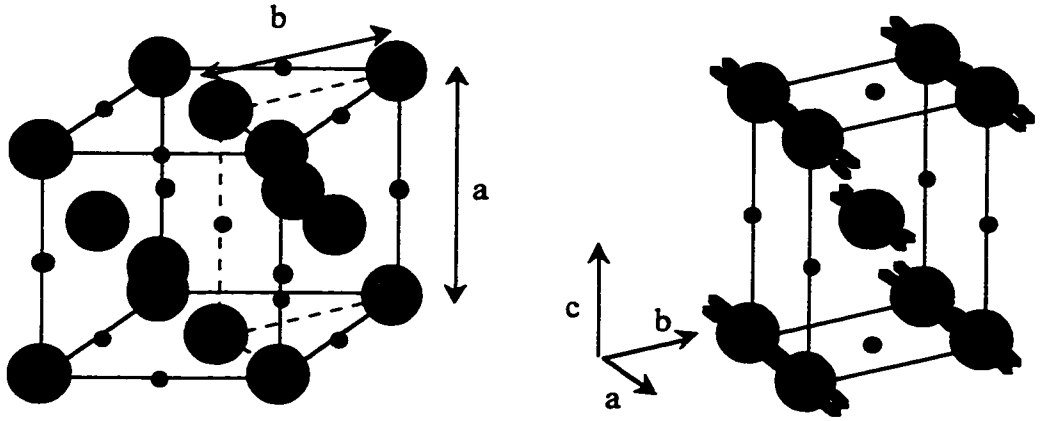

High-T Rocksalt Phase Low-T Orthorhombic Polymer

Figure 1.5. High- and low- temperature phases of AC_{60}.

Material	High-T a	High-T b	Polymer a	Polymer b	Polymer c
KC_{60}	14.07 Å	9.94 Å	9.11 Å	9.95 Å	14.32 Å
RbC_{60}	14.08 Å	9.96 Å	9.13 Å	10.11 Å	14.23 Å
CsC_{60}	14.13 Å	9.99 Å	9.10 Å	10.21 Å	14.17 Å

Figure 1.6. Lattice Parameters of the AC_{60} high-T and polymer phases

Figure 1.5 shows the high- and low- temperature structure of AC_{60}[10, 11]. As was

discussed above, AC_{60} has an FCC 'rocksalt' structure above 80 °C. When the material cools, the polymer chains form along the face diagonals of the high-temperature cubic unit cell. This results in an orthorhombic structure, with the **a** direction along the polymer chains. The **b** vector is derived from the other fcc face diagonal, while the **c** vector is along the original cubic lattice vector perpendicular to the face. The polymerization results in a dramatic contraction along the **a** direction, while the there is a slight expansion in the **b** and **c** directions. The lattice parameters for KC_{60}, RbC_{60}, and CsC_{60} in the high-T and polymer phases are shown in figure 1.6. Although the three materials are virtually identical in the polymer direction, the differing size of the alkali intercalants causes significant differences in the **b** and **c** directions, with the chains separated by larger distances for larger intercalants. This inter-chain separation is expected to significantly affect the electronic structure of the material[14].

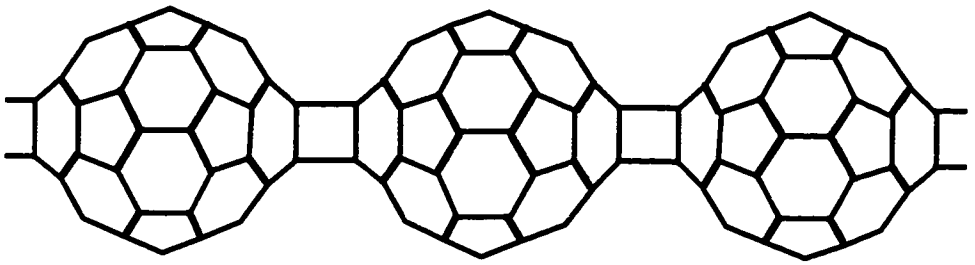

Figure 1.7. Projection of the structure of the fullerene polymers in AC_{60}, showing the square 2+2 cycloaddition bonds[15]

Figure 1.7 shows the structure of an individual polymer chain. Neighboring C_{60} molecules are bonded by 2+2 cycloaddition reaction which results in a square structure comprising a pair of atoms on each C_{60} molecule. Reitveld analysis of x-ray diffraction spectra[11] shows that the distance between these pairs is $\approx$ 1.6 Å, consistent with covalent

bonding. In addition, NMR studies[16, 17] show four sp^3 carbon sites per C_{60} molecule, consistent with the 2+2 cycloaddition picture. Of considerable interest has been the relative orientation of neighboring chains in a crystal of AC_{60}. XRD suggests that the planes formed by the inter-fullerene bonds are tilted at an angle of 45° to the **b** axis, and that nearest-neighbor chains are tilted in opposite directions; however, it is extremely difficult to make a definitive assignment of the orientational ordering from a powder diffraction study. Because the electronic overlap between neighboring chains should be highly sensitive to their relative orientation[14, 18, 19], a more exact determination of this orientation is highly desirable. In fact, recent NMR investigations[20] have provided evidence that the chain orientation is KC_{60} is different from that of the Rb and Cs compounds. We will return to this issue in the next chapter.

Crystalline samples of AC_{60} were first synthesized by Pekker, *et al.*[21] using a coevaporation method. Coevaporated crystals, when exposed to air and dissolved in toluene, broke apart into parallel fibers consisting only of polymerized AC_{60}. It was originally thought that the polymers were aligned with the long axis of the fiber. Detailed analysis using electron diffraction later determined[22] that the polymers were in fact oriented along the short axis of the fibers, in a 'zigzag' twinning structure which eliminates any bulk anisotropy in the material. By twinning, the crystal minimizes the stress created by the contraction in the polymerization direction. We expect this twinning to be a generic feature of the AC_{60} materials.

1.6 Electronic Properties of the AC_{60} Polymer Phase

The electronic properties of the AC_{60} materials have been observed using a number of methods, including electrical transport[23-25], microwave conductivity[26], infrared spectroscopy[27, 28], NMR[17, 20, 29-34], electron spin resonance (ESR)[10, 13, 26, 35-39], and muon spin rotation (μSR)[37, 40, 41]. The high-temperature rocksalt phase of AC_{60} is conducting, with a resistivity of $\approx$ 18 mΩ-cm, as determined from infrared-transmission experiments[27]. The same measurements show that the polymer phase has a room-temperature resistivity of $\approx$ 9 mΩ-cm. When cooled, however, the polymer phase displays highly interesting behavior, with the KC_{60} material showing substantially different behavior from that of the RbC_{60} and CsC_{60} polymers. A transition to an insulating state below 50 K was first observed for the Rb and Cs materials by ESR[10] as a dramatic reduction in the conduction electron spin susceptibility, which indicates a freezing out of charge carriers; this transition is not observed in KC_{60}. It was conjectured at the time that the low-temperature nonmetallic state was a spin density wave (SDW) state which arises from a quasi-1D electronic structure. Later NMR[33] and ESR[39] experiments have confirmed that the low-T state is antiferromagnetically ordered, with a 3D ordering near 35 K and fluctuations above that temperature; infrared and microwave conductivity[26] measurements show evidence for a broad transition to an insulating state at low temperature. Neutron scattering experiments[42-44], on the other hand, see no superlattice peaks which should accompany a magnetic ordering, although a softening of certain phonon modes is observed. Still unresolved is the dimensionality of the electronic structure in the AC_{60} materials. KC_{60} seems to be a 3-D metal, but there is still some conflict over the dimensionality of RbC_{60} and

CsC_{60}. The ESR linewidth[10] in these materials is two orders of magnitude narrower than in the A_3C_{60} materials, and increases substantially under pressure[35], behavior which is consistent with a quasi 1-D electronic structure. On the other hand, the covalent bonding along the polymer chains should act to block conduction in the chain direction; electronic structure calculations[19] show that the electronic structure should be significantly closer to 3-D than 1-D.

Chapter 1 References

1. T. G. Deitz, M. A. Duncan, D. E. Powers, *et al.*, J. Chem. Phys. **74**, 6511 (1981).

2. H. W. Kroto, J. R. Heath, S. C. O'Brien, *et al.*, Nature **318**, 162-3 (1985).

3. W. Kratschmer, L. D. Lamb, K. Fostiropoulos, *et al.*, Nature **347**, 354-8 (1990).

4. H. Ehrenrich and F. Spaepen, *Fullerenes* (Academic Press, San Diego, CA, 1994), and references therein.

5. P. W. Fowler and D. E. Manolopoulos, *An atlas of fullerenes* (Oxford University Press, Oxford, 1995).

6. A. F. Hebard, M. J. Rosseinsky, R. C. Haddon, *et al.*, Nature **350**, 600 (1991).

7. J. Winter and H. Kuzmany, Solid State Communications **84**, 935-8 (1992).

8. P. W. Stephens, in *Physics and Chemistry of Fullerenes and Derivatives. Proceedings of the International Winterschool on Electronic Properties of Novel Materials*, edited by H. Kuzmany, J. Fink, M. Mehring and S. Roth, (World Scientific, River Edge, NJ, 1995), p. 291-6.

9. Q. Zhu, O. Zhou, J. E. Fischer, *et al.*, Physical Review B **47**, 13948-51 (1993).

10. O. Chauvet, G. Oszlanyi, L. Forro, *et al.*, Physical Review Letters **72**, 2721-4 (1994).

11. P. W. Stephens, G. Bortel, G. Faigel, *et al.*, Nature **370**, 636-9 (1994).

12. M. Nunez-Regueiro, L. Marques, J.-L. Hodeau, *et al.*, Physical Review Letters **74**, 278-281 (1995).

13. D. Koller, M. C. Martin, P. W. Stephens, *et al.*, Applied Physics Letters **66**, 1015-17 (1995).

14. S. C. Erwin, G. V. Krishna, and E. J. Mele, Physical Review B (Condensed Matter) **51**, 7345-8 (1995).

15. S. Pekker, L. Forro, L. Mihaly, *et al.*, Solid State Communications **90**, 349-52 (1994).

16. T. Kalber, G. Zimmer, and M. Mehring, Zeitschrift fur Physik B (Condensed Matter) **97**, 1-2 (1995).

17. H. Alloul, V. Brouet, E. Lafontaine, *et al.*, Physical Review Letters **76**, 2922-5 (1996).

18. K. Tanaka, T. Saito, Y. Oshima, *et al.*, Chemical Physics Letters **272**, 189-192 (1997).

19. E. J. Mele, G. V. Krishna, and S. C. Erwin, Physical Review B (Condensed Matter) **52**, 12493-6 (1995).

20. V. Brouet, H. Alloul, A. Janossy, *et al.*, in *Molecular Nanostructures: Proceedings of the International Winterschool on Electronic Properties of Novel Materials*, edited by H. Kuzmany (World Scientific, River Edge, NJ, 1997), p. 328-332.

21. S. Pekker, A. Janossy, L. Mihaly, *et al.*, Science **265**, 1077-8 (1994).

22. S. Pekker, M. Carrard, L. Forro, *et al.*, in *Fullerenes and Fullerene Nanostructures: Proceedings of the International Winterschool on Electronic Properties of Novel Materials*, edited by H. Kuzmany, J. Fink, M. Mehring and S. Roth, (World Scientific, River Edge, NJ, 1996), p. 110-14.

23. G. Oszlanyi, G. Baumgartner, A. Neuenschwander, *et al.*, in *Physics and Chemistry of Fullerenes and Derivatives. Proceedings of the International Winterschool on Electronic Properties of Novel Materials*, edited by H. Kuzmany, J. Fink, M. Mehring and S. Roth, (World Scientific, River Edge, NJ, 1995), p. 425-31.

24. J. Hone, M. S. Fuhrer, K. Khazeni, *et al.*, Physical Review B (Condensed Matter) **52**, R8700-2 (1995).

25. K. Khazeni, V. H. Crespi, J. Hone, *et al.*, Physical Review B (Condensed Matter) **56**, 6627-30 (1997).

26. F. Bommeli, L. Degiorgi, P. Wachter, *et al.*, Physical Review B (Condensed Matter) **51**, 14794-7 (1995).

27. M. C. Martin, D. Koller, X. Du, *et al.*, Physical Review B (Condensed Matter) **49**, 10818-21 (1994).

28. M. C. Martin, D. Koller, A. Rosenberg, *et al.*, Physical Review B (Condensed Matter) **51**, 3210-13 (1995).

29. K. F. Thier, M. Mehring, and F. Rachdi, in *Fullerenes and Fullerene Nanostructures: Proceedings of the International Winterschool on Electronic Properties of Novel Materials*, edited by H. Kuzmany, J. Fink, M. Mehring and S. Roth, (World

Scientific, River Edge, NJ, 1996), edited by H. Kuzmany, J. Fink, M. Mehring and S. Roth, 1996), p. 93-6.

30. K. F. Thier, M. Mehring, and F. Rachdi, Physical Review B (Condensed Matter) **55**, 124-6 (1997).

31. K. F. Thier, G. Zimmer, M. Mehring, *et al.*, Physical Review B (Condensed Matter) **53**, R496-9 (1996).

32. V. Brouet, Y. Yoshinari, H. Alloul, *et al.*, Physica C **235-240**, 2481-2 (1994).

33. V. Brouet, H. Alloul, Y. Yoshinari, *et al.*, Physical Review Letters **76**, 3638-41 (1996).

34. F. Rachdi, C. Goze, L. Hajji, *et al.*, Applied Physics A (Materials Science Processing) **64**, 295-9 (1997).

35. L. Forro, G. Baumgartner, A. Sienkiewicz, *et al.*, in *Fullerenes and Fullerene Nanostructures: Proceedings of the International Winterschool on Electronic Properties of Novel Materials*, edited by H. Kuzmany, J. Fink, M. Mehring and S. Roth, (World Scientific, River Edge, NJ, 1996), p. 102-9.

36. L. Granasy, T. Kemeny, G. Oszlanyi, *et al.*, Solid State Communications **97**, 573-8 (1996).

37. Y. J. Uemura, K. Kojima, G. M. Luke, *et al.*, Physical Review B (Condensed Matter) **52**, R6991-4 (1995).

38. V. A. Atsarkin, V. V. Demidov, G. A. Vasneva, *et al.*, Solid State Communications **98**, 977-80 (1996).

39. A. Janossy, N. Nemes, T. Feher, *et al.*, Physical Review Letters **79**, 2718-21 (1997).

40. W. A. MacFarlane, R. F. Kiefl, S. Dunsiger, *et al.*, Physical Review B (Condensed Matter) **52**, R6995-8 (1995).

41. M. Larkin, K. Kojima, G. M. Luke, *et al.*, in *7th International Conference on Muon Spin Rotation/Relaxation/Resonance*, (Nikko, Japan, 1996), Vol. 104, p. 325-9.

42. H. Schober, A. Tolle, B. Renker, *et al.*, Physical Review B (Condensed Matter) **56**, 5937-50 (1997).

43. B. Renker, R. Heid, F. Gompf, *et al.*, in *Fullerenes and Fullerene Nanostructures: Proceedings of the International Winterschool on Electronic Properties of Novel*

Materials, edited by H. Kuzmany, J. Fink, M. Mehring and S. Roth, (World Scientific, River Edge, NJ, 1996), p. 136-41.

44. B. Renker, H. Schober, and R. Heid, Applied Physics A (Materials Science Processing) **64**, 271-81 (1997).

Chapter 2.

Synthesis and Characterization of Crystalline AC_{60}.

2.1 Motivation

Our synthesis of crystalline AC_{60} was motivated by the method of Pekker *et al*,[1] who reported the synthesis of individual fibers of KC_{60}. They did this by placing stoichiometric amounts of C_{60} and K on opposite ends of an evacuated quartz tube, and then differentially heating the ends in order to grow doped crystals by vapor phase transport. When the resulting crystals were slow-cooled and immersed in toluene, they broke apart into parallel fibers which were composed of pure o-KC_{60}. It was thought that the polymerization direction was parallel to the long axis of the fibers, although further investigation revealed that the fibers had a lamellar twinning pattern, with the direction of polymerization actually perpendicular to the long axis.

Before cooling, the crystals grown in the above experiment were in the high-temperature rocksalt phase, with no preferred direction for polymerization. Therefore we guessed that this vapor-phase growth was not a unique route to the formation of AC_{60} crystals. We decided instead to grow high-quality single crystals of pristine C_{60}, intercalate them to the correct stoichiometry, and then cool them through the polymerization transition. These crystals could then be exposed to air and immersed in toluene to remove all of the non-polymerized material. The method described below was used to synthesize

crystalline (but highly twinned) samples of KC_{60}. RbC_{60}, CsC_{60}, and mixed-intercalant $Rb_{1-x}K_xC_{60}$.

2.2 Growth of Single-crystal C_{60}.

Single crystals of C_{60} were grown using a method developed in our laboratory by Michael Fuhrer. This method consists of a vapor-phase growth technique, as depicted in figure 2.1. A gold boat with C_{60} powder is inserted into a quartz tube, which is then inserted into an outer quartz tube in a three-zone furnace under flowing argon (10cc/min). The three zones of the furnace are set to 630, 565, and 500 °C, with the hottest zone at the end with the C_{60}. The C_{60} evaporates from the boat and condenses on the walls of the inner tube, which is necked to provide preferential sites for crystal growth. After a few days, millimeter-sized crystals grow, and can then be collected by removing the inner quartz tube from the furnace.

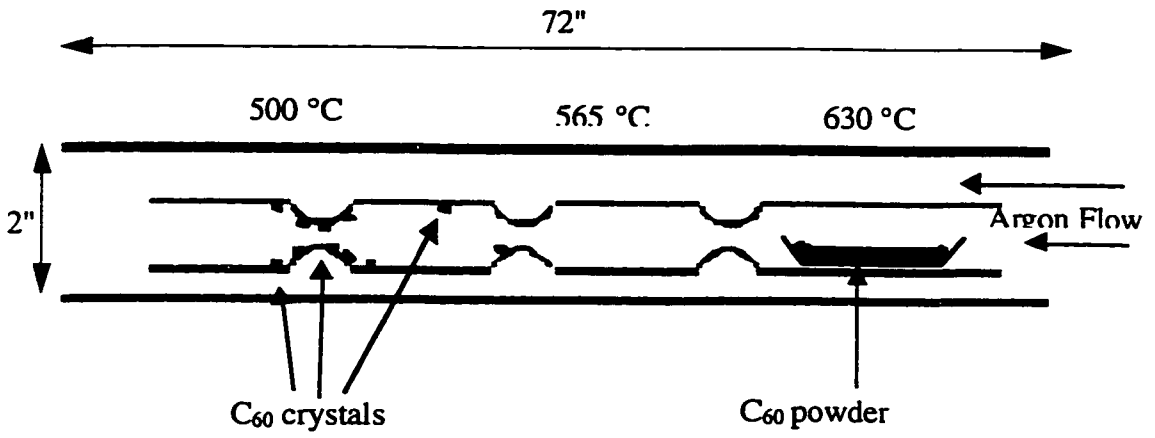

Figure 2.1 Vapor-transport growth of C_{60} crystals

2.3 Doping of C_{60} Crystals and Isolation of the AC_{60} Phase

To intercalate the previously-grown C_{60} crystals to the A_1C_{60} stoichiometry, stoichiometric amounts of C_{60} crystals and alkali metal were sealed into 1/2" pyrex tubes. This was done by first weighing out the desired amount of crystals, then baking them out in the pyrex tube at 250 °C overnight under a dynamic vacuum using a turbopump. After bake-out, the tube with crystals was closed off (using a valve) and loaded into an inert atmosphere (argon) glove box. In the glove box, the correct amount of alkali metal was inserted into the tube. Measuring the correct amount of alkali metal was difficult. The most straightforward method was to weigh it on a scale in the glove box. However, manipulating small pieces of potassium, rubidium, or cesium is tricky; the metals are quite soft, and tend to stick to everything; also, weighing materials in the glove box is somewhat imprecise because pressure variations lead to errors in the weight. Therefore, this method worked best when a relatively large amount of alkali metal (10 mg or more) was used. Another method was to measure out smaller amounts of metal volumetrically by inserting them into a narrow capillary. This requires melting the metal on a hot plate and heating the capillary so that the metal will flow without solidifying.

A final method which was used to obtain small amounts of alkali metals for intercalation was to use a getter source. A feedthrough was made using 1/4" pyrex tubing and two tungsten rods. The glass was melted over the tungsten rods at one end to make a vacuum seal; at the other end, stainless steel tubes were placed over the tungsten rods. A getter source (SAES getters) was spot-welded to the steel tubes; the entire assembly was fed through a vacuum fitting connected to a "T" junction so that it could be inserted into the 1/2" pyrex tube containing the C_{60} crystals while a dynamic vacuum was maintained. The

crystals and getter were baked out overnight, and then alkali metal was extracted from the getter by resistive heating. The pyrex tube was immersed in water for cooling, so that the alkali metal would condense on the walls of the pyrex tube. The getters were calibrated by running them in empty tubes, pouring a measured amount of water into the tube, and measuring the pH of the resulting alkali hydroxide solution. The getters were found to release 1.2, 2.2, 3.9, and 5.9 mg of Na, K, Rb, and Cs, respectively, if run at 7.5 A for 30 minutes. This method proved to be the best way to obtain small amounts of alkali metal, and as a side benefit did not require use of the glove box.

Once the required amounts of C_{60} crystals and alkali metal were inserted into a pyrex tube, the tube was evacuated and sealed with a torch. The tube was then inserted into an oven at 300 °C and left there for a few weeks. At the end of this time, the oven was cooled slowly (overnight) to room temperature. The sealed pyrex tube was opened and the crystals exposed to air. Finally, the crystals were immersed in toluene for at least ten days. This last step was performed in order to remove all of the impurity phases in the crystals; at the end, only the polymerized o-AC_{60} should remain. Initially, the toluene turned purple from dissolved C_{60}; therefore, the solvent was poured off and replaced every day or two, until the solvent remained clear. The remaining crystals were then removed from the toluene and stored in an evacuated desiccator to prevent any unnecessary oxidation of the surface

2.4 Characterization of AC_{60} crystals

Figure 2.2 shows a representative AC_{60} crystal after purification, alongside a pris-

tine C_{60} crystal. After the toluene purification process, the AC_{60} crystals generally have a shell structure—evidently, the alkali metal does not generally penetrate fully into the crystal in the allowed doping time. The material is slightly gray, in contrast to the shiny black of pristine C_{60}. Often, the crystals have a brown material on the surface; this is an impurity, and is not electrically conducting. The crystals exhibit no anisotropy or fibrous structure which might be associated with a preferred direction of polymerization; this is consistent with the expectation that the polymerization occurs in small domains, resulting in a multiple twinning of the resulting crystal.

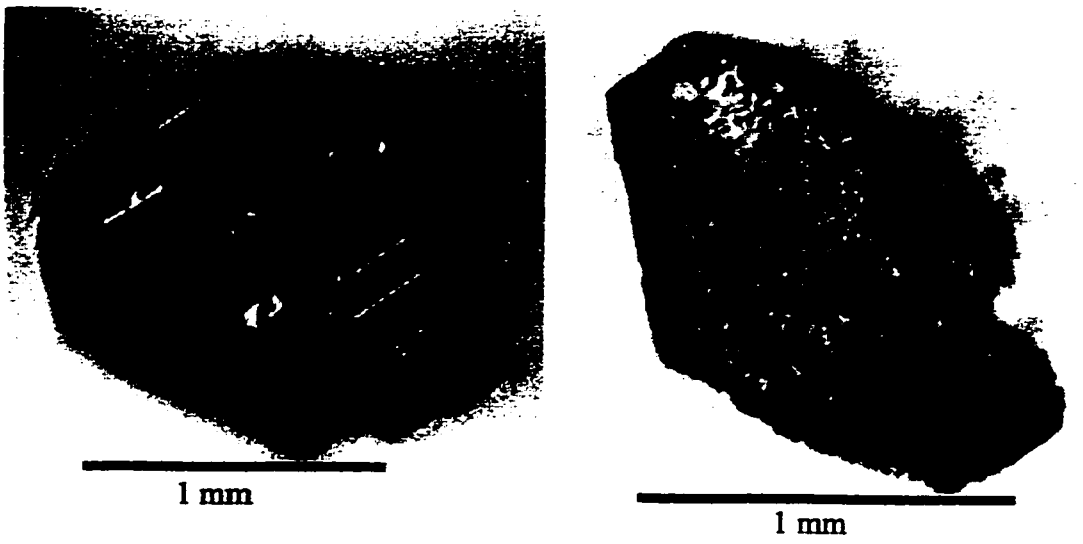

Figure 2.2 Pristine C_{60} crystal (left) and purified AC_{60} (right)

The crystal structure of the purified AC_{60} crystals was confirmed using x-ray diffraction, in collaboration with Jeffrey Nguyen in the group of Raymond Jeanloz. A powder diffraction spectrum of each material (K, Rb, and CsC_{60}) was obtained by placing a

crystal of the material in a rotating-anode spectrometer. Figure 2.3 shows the spectrum that was obtained for RbC_{60}. The solid lines are the major peaks in the reported diffraction spectrum[2] of RbC_{60}; the good agreement between our data for KC_{60}, RbC_{60}, and CsC_{60} and their published spectra confirms that the crystals of all three materials consist primarily of the polymerized o-AC_{60} phase.

2.5 Transmission Electron Microscopy Study of KC_{60} and RbC_{60}.

To further study the structure and bonding character of the AC_{60} crystals, a high-resolution transmission electron microscopy (HRTEM) study was undertaken[3]. The microscopy and much of the data analysis was performed by Nasreen Chopra. For the study, crystals were ground between glass slides and the powder deposited onto holey carbon grids. Imaging was done in a JEOL TEM 200CX microscope using a 200-keV accelerating voltage.

Figure 2.4 shows an image of KC_{60} under moderate magnification, taken under phase contrast imaging conditions. The fact that this image is possible is interesting in and of itself: previous HRTEM studies[4] of pristine C_{60} an C_{70} have demonstrated that pristine, unpolymerized fullerene materials turn amorphous within a matter of minutes of exposure to the electron beam. In contrast, we discovered that KC_{60} is stable in the electron beam for hours; RbC_{60}, while less stable than KC_{60}, is significantly more stable than the pristine material. The coherence of the lattice fringes over large distances shows that the KC_{60} samples are crystalline over fairly large domains. By counting the lattice fringes, we are able to extract lattice spacings of a=9.0 Å, b=10.1 Å, c=14.3 Å, which are in good agree-

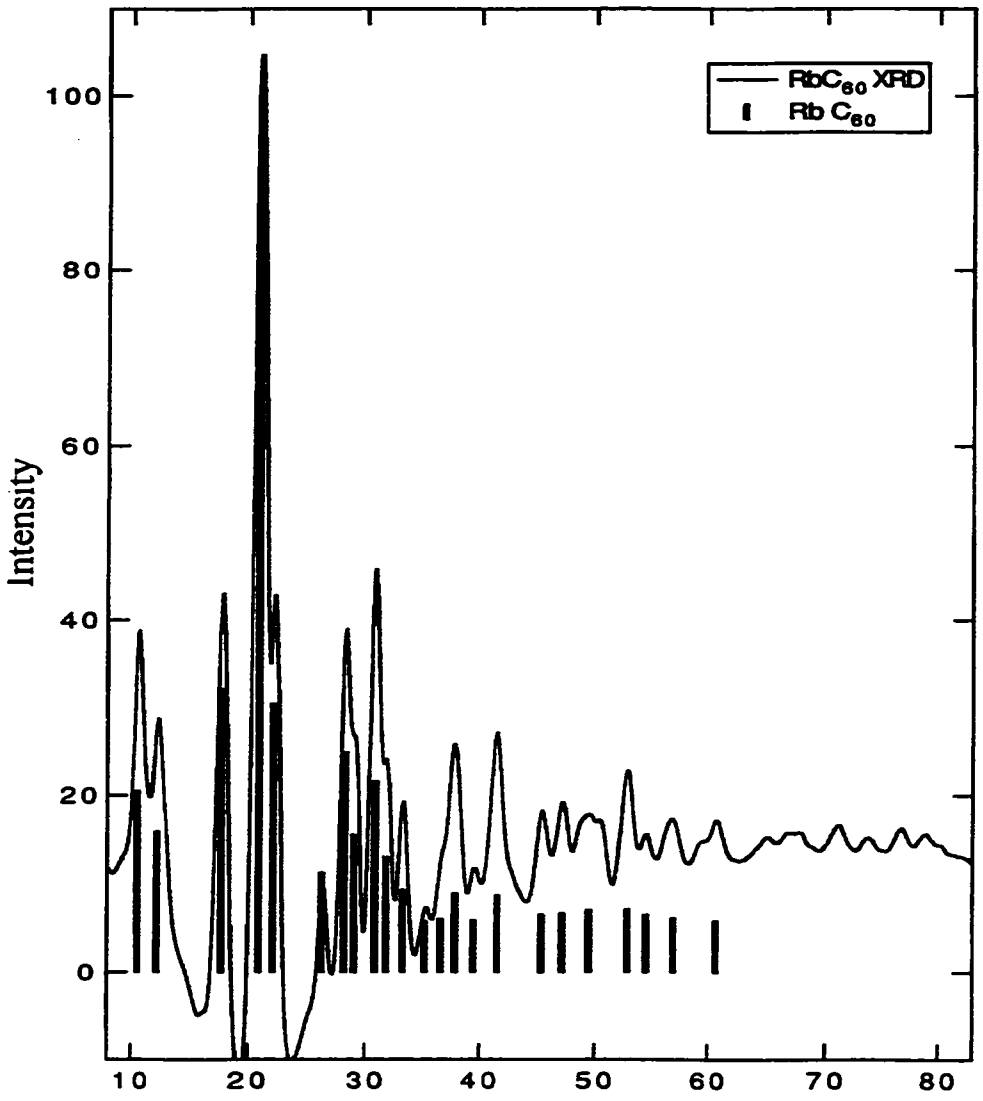

Figure 2.3 X-Ray Powder Diffraction Spectrum of RbC_{60}.

ment with the values obtained from x-ray diffraction studies[2].

Figure 2.5 is a high-magnification image of KC_{60}, with the polymerized direction (**a** axis) of this domain oriented roughly horizontally, and the **c** axis vertically. The different spacings in the vertical and horizontal directions reflect the orthorhombic structure of

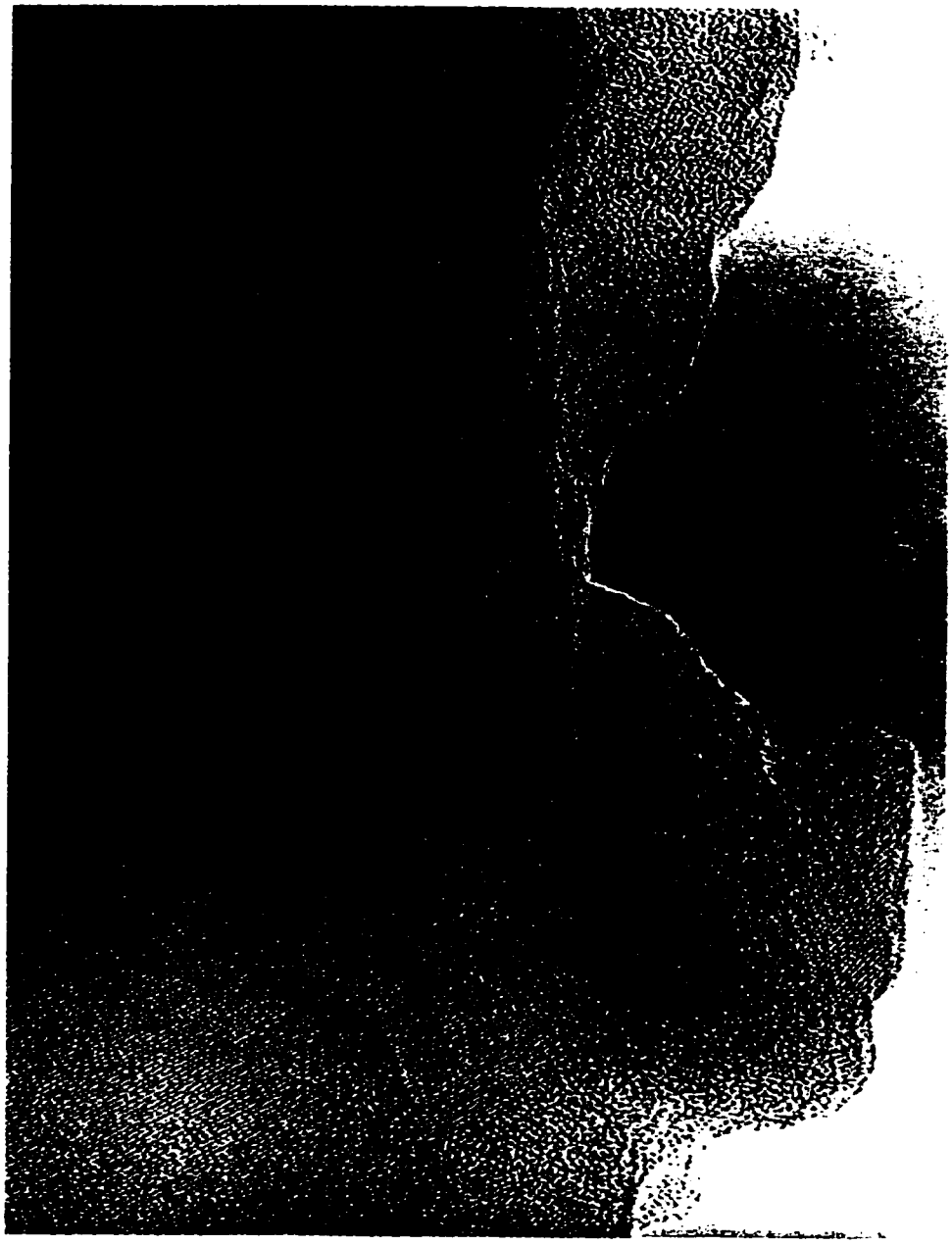

Figure 2.4 Transmission electron micrograph of KC_{60} (courtesy N. Chopra)

the KC_{60} crystal which results from contraction in the direction of polymerization. This image clearly shows the dominant components (individual C_{60} molecules) of the unit cell. It is difficult to image individual C_{60} molecules in pristine C_{60}, because of the motion of

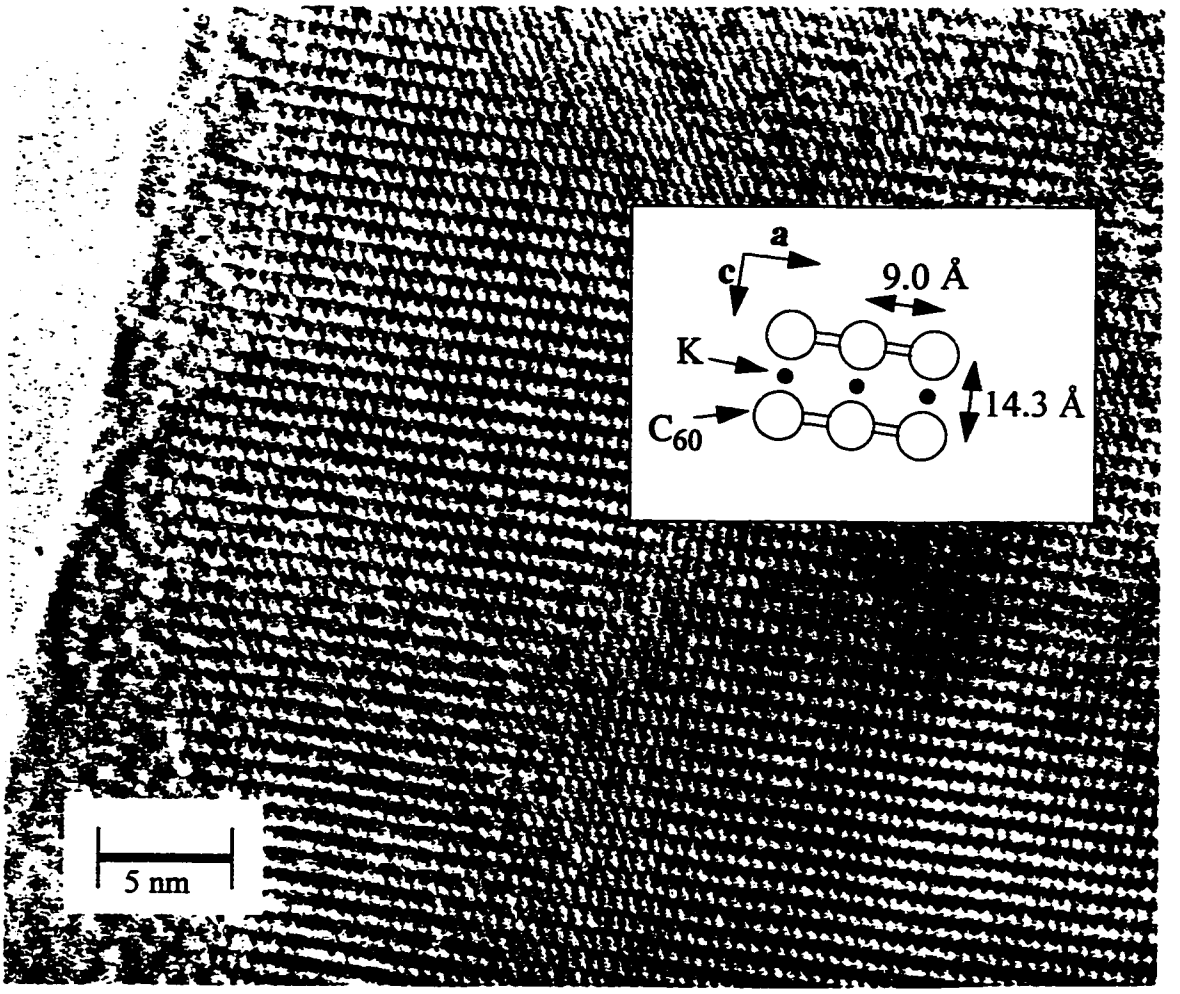

Figure 2.5 High-resolution TEM image of KC_{60} (courtesy N. Chopra)

the balls at room temperature; the clarity with which the C_{60} can be imaged in this material indicates that the C_{60} balls are not moving significantly in the lattice. This is additional evidence for the polymerization in KC_{60}.

In order to further study the bonding in KC_{60}, we conducted an electron-energy-loss spectroscopy (EELS) study. Figure 2.6 shows the EELS spectrum of KC_{60} obtained using 200 keV electrons. The spectrum shows the characteristic 284-eV K-edge onset for carbon, while the potassium L-edge at 294 rides on the carbon edge and cannot be

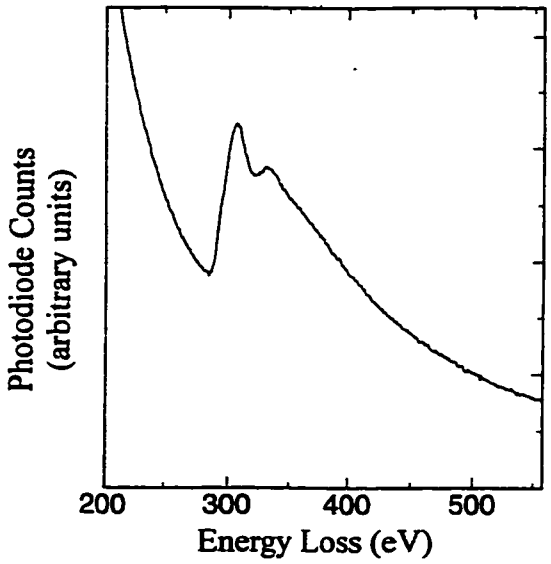

Figure 2.6 EELS spectrum of KC_{60} (Courtesy N. Chopra)

resolved. The fine structure of the carbon peak in this spectrum is different from that observed in sp^2-bonded carbon; we believe that this reflects the sp^3 character of the carbon atoms involved in the interfullerene bonds. Finally, we note that the EELS spectrum of KC_{60} is also stable for at least one hour, while that of pristine C_{60} degrades within a matter of minutes, reflecting the amorphization seen in imaging experiments.

2.6 Single-Crystal XRD Study of AC_{60}.

Because of the complexity of the unit cell in the AC_{60} materials, it proved difficult to completely establish their crystal structure from Reitveld refinement of power X-ray diffraction patterns. Specifically, the issue of the relative orientation of nearest-neighbor chains remains an open question, although NMR[5] studies indicate that the chain-chain orientation in KC_{60} is different than in Rb- and CsC_{60}. This issue was also unresolved in a

similar material--the orthorhombic linear polymer formed by pristine C_{60} after treatment at high temperature and pressure. A single-crystal XRD study[6] was able to determine the chain orientation in the pristine material. As a pressure-treated C_{60} crystal cools from above 300 °C, it polymerizes in the same way that the AC_{60} materials do. The original cubic symmetry of the crystal is strongly broken as it goes into an orthorhombic structure. The crystal develops a multi-domain structure, with 12 orientational domains: there are six possible choices for the **a** (polymer chain) direction, and for each of these chain directions there are two possible choices of the **b** (or **c**) axis orientation. Thus the diffraction patterns that were observed represented the superposition of 12 individual diffraction patterns; a detailed analysis of the diffraction patterns revealed that there was a 45° orientational difference between nearest neighbor chains.

Because of the success of single-crystal XRD in deconvolving the 12-fold superposed diffraction patterns in the pristine materials, we embarked upon a collaboration with the authors of the pristine C_{60} study, Pascale Launois and Roger Moret at the University of Paris. Figure 2.7 represents a single-crystal diffraction pattern of a KC_{60} crystal grown in our laboratory. The pattern shows the same 12-fold superposition as was seen in the pristine polymer. The width of the diffraction spots reflects the mosaicity of the crystal: the small size of individual domains leads to a broadening of the diffraction peaks. Their study of our KC_{60} and RbC_{60} crystals is ongoing, but initial results indicate that the orientation of nearest-neighbor chains is in fact different in KC_{60} and RbC_{60}. Thus there may be two factors which cause KC_{60} to have a different electronic structure from that of the Rb- and Cs- materials. It has a smaller interchain distance, but also may have a different chain-chain orientation.

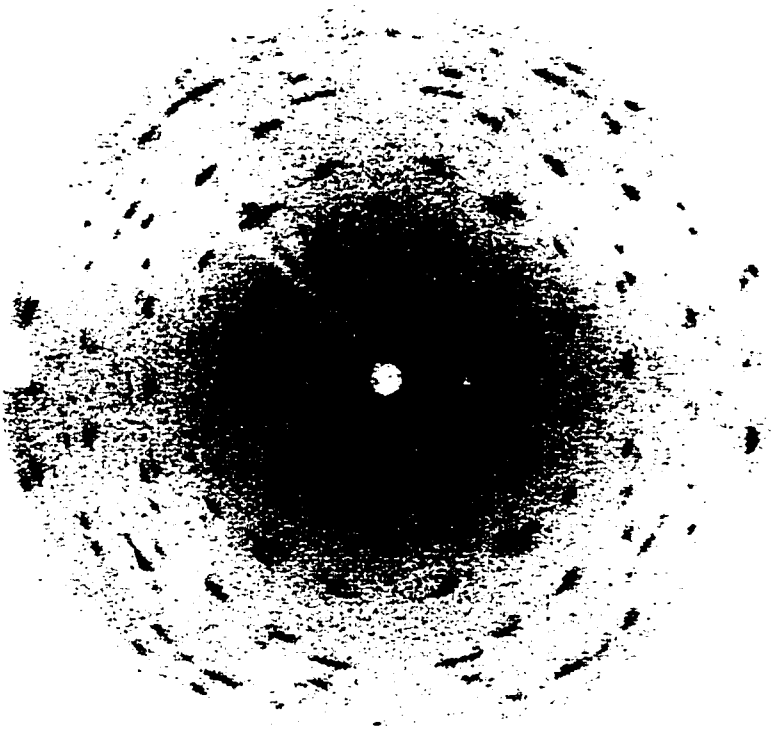

Figure 2.7 Single-Crystal X-Ray Diffraction Pattern of KC_{60}.(Courtesy P. Launois)

Chapter 2 References

1. S. Pekker, A. Janossy, L. Mihaly, *et al.*, Science **265**, 1077-8 (1994).

2. P. W. Stephens, G. Bortel, G. Faigel, *et al.*, Nature **370**, 636-9 (1994).

3. N. G. Chopra, J. Hone, and A. Zettl, Physical Review B (Condensed Matter) **53**, 8155-6 (1996).

4. S. Seraphin, D. Zhou, and J. Jiao, Journal of Materials Research **8**, 1895-1899 (1993).

5. V. Brouet, H. Alloul, A. Janossy, *et al.*, in *Molecular Nanostructures: Proceedings of the International Winterschool on Electronic Properties of Novel Materials*, edited by H. Kuzmany (World Scientific, River Edge, NJ, 1997), p. 328-332.

6. R. Moret, P. Launois, P. A. Persson, *et al.*, Europhysics Letters **40**, 55-60 (1997).

Chapter 3.

Transport Measurements of AC_{60}.

3.1 Techniques for Resistivity Measurements

Because the AC_{60} materials retain a crystalline form after the purification process, it is relatively straightforward to perform electrical transport measurements on these materials. The temperature-dependent resistivity of AC_{60} samples was measured using a standard four-probe technique; currents of between 10 μA and 1 mA were supplied with a HP Data Acquisition / Control unit (DAC), and voltages were measured using Keithley nanovoltmeters. The instruments were controlled and data stored by the Zettl group 'R vs. T' LabView program. The dc resistance of the sample is measured in both the forward and reverse direction, and the results then averaged, in order to remove any effects from thermal or radiative EMF's. Samples were cooled on probes in helium dewars, and the temperature measured with a variety of sensors, including diodes and resistive sensors.

The only difficulty involved in performing transport measurements on these materials proved to be making good electrical contacts. For KC_{60}, wires (.0005" annealed gold) could be attached using conductive silver paint (Dupont conductor composition 4929N). However, this method did not work well for RbC_{60}--apparently RbC_{60} forms a thin oxide layer (either due to reaction with air or the solvents in the silver paint). This oxide layer is thin enough that contacts made with silver paint conduct reasonably well at room temperature, exhibiting a resistance of a few kΩ typically, but always go bad (often

showing dramatic nonlinear behavior) at low temperatures. Other conducting adhesives, including silver epoxies, and gold, platinum, and carbon paint, were tried, without success. One solution was to evaporate metal pads onto the surface of the crystals. A variety of methods were used to mask portions of the crystals; the easiest proved to be to place the crystals over a copper grid (or combination of crossed grids) to produce a striped (checked) pattern of pads. The best contacts were obtained by evaporating approximately 100 Å of chromium, followed by 1000 Å of gold; chromium aids in the adhesion of gold to many surfaces, including oxides. A few samples with good contacts (in the range of tens of ohms) were obtained in this manner; however, even this method proved to be unreliable.

3.2 R(T) of KC_{60} at ambient pressure

Figure 3.1 shows the temperature-dependent resistivity of a representative sample of KC_{60} from 350 K to 4.2 K; all samples measured showed identical behavior above 80 K, and qualitatively similar behavior below that temperature. The resistivity has been normalized to its room-temperature value. Measurement of the exact resistivity of the samples is difficult due to their irregular geometry; our best estimate was 10-20 mΩ-cm. The sample shows positive $d\rho/dT$ above 50 K, indicating metallic behavior. In fact, the temperature-dependence of the resistivity can be fit to an empirical function of the form

$$\rho(T) \approx a + bT + cT^2, \tag{3.1}$$

as indicated by the solid line in fig. 3.1.

Figure 3.2 shows the $\rho(T)$ behavior of Rb_3C_{60} for comparison (K_3C_{60} displays

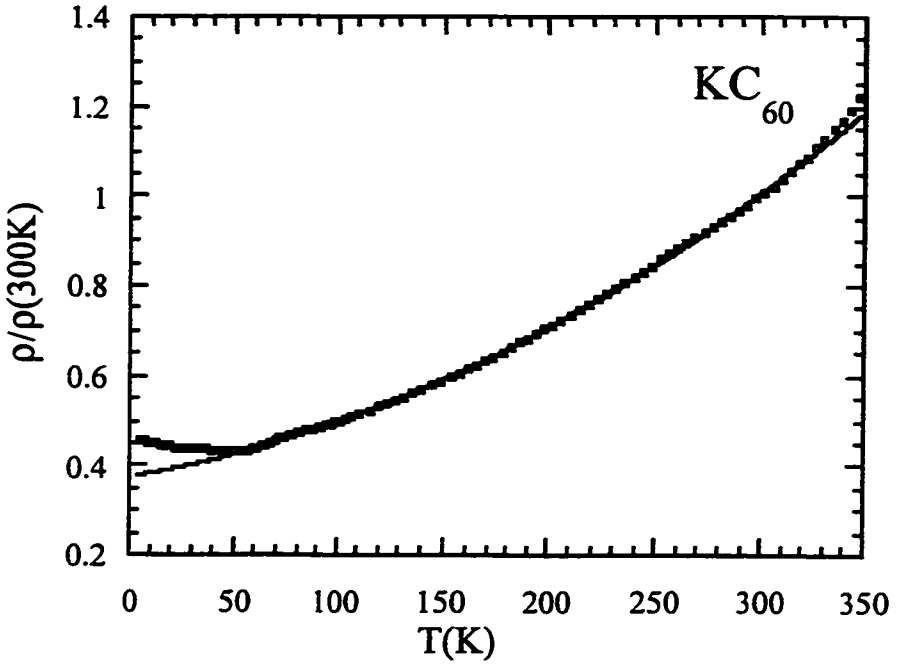

Figure 3.1 ρ(T) of KC_{60} from 350 K to 4.2 K The solid line represents an empirical fit (Eq. 3.1) to the data above 80 K.

identical transport behavior, except that its T_c is lower); from 30 K to 250 K, the resistivity follows the functional form[1]

$$\rho(T) \approx a + bT^2 \quad . \tag{3.2}$$

Thus the resistivity behavior of KC_{60} is quite similar to that of K_3C_{60} in the normal state, except that the behavior of KC_{60} is closer to linear than that of K_3C_{60}. The quadratic behavior of ρ(T) in K_3C_{60} has been explained as an artifact of the high thermal expansion of the material and its strongly volume-dependent resistivity[2]. When the resistivity is corrected for thermal expansion, it is linear, as is expected for a normal metal. We speculated

that this thermal expansion accounts for the nonlinear temperature dependence in the ρ(T) of KC_{60} as well, and that the weaker curvature was the result of a smaller thermal expansion coefficient due to the polymerization. We will examine this hypothesis in section 3.8.

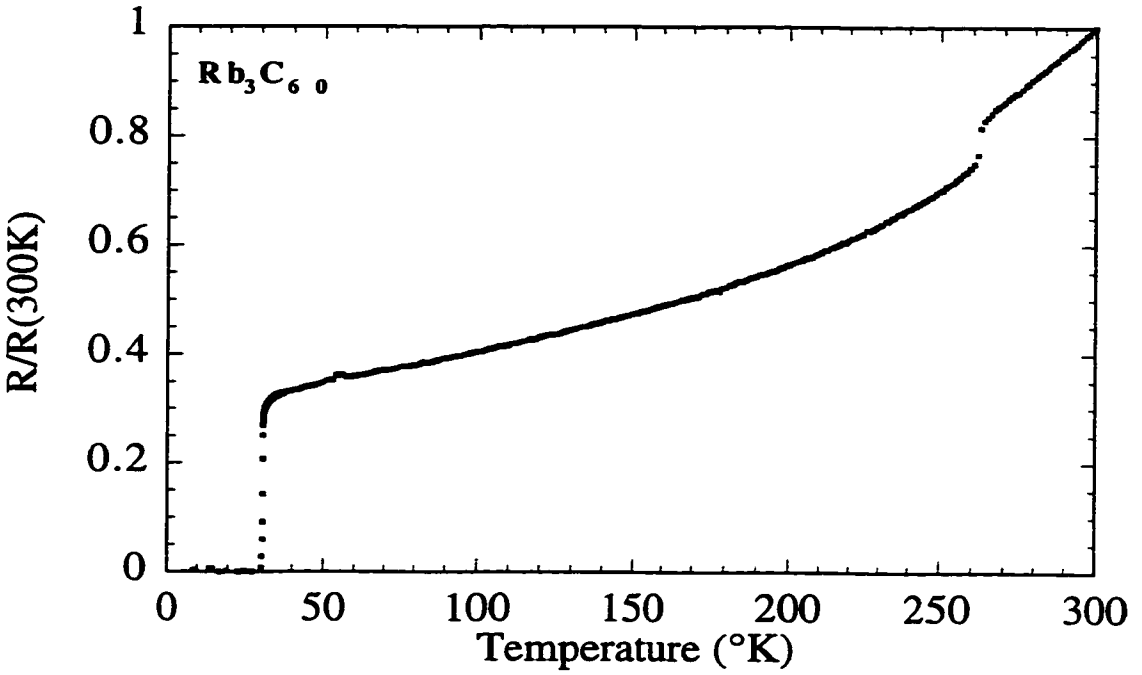

Figure 3.2 ρ(T) of Rb_3C_{60} from 350 K to 4.2 K (From M.S. Fuhrer)

A_3C_{60} crystals often display an increase in ρ upon warming above 260 K, as can be seen in Fig. 3.2. This is the signature of the orientational ordering transition which takes place at this temperature in pristine C_{60}. Doped crystals often contain a minority phase of undoped material; the expansion of the C_{60} lattice above 260 K in the undoped

phase causes the entire doped crystal to expand, resulting in an increase in resistivity. This transition is not seen in the ρ(T) behavior of the purified KC_{60} material, further confirming the phase-purity of the samples.

Figure 3.3 highlights the low-temperature behavior of the resistivity of KC_{60}. It displays nonmetallic temperature dependence below 50 K. Although it has been speculated that all of the AC_{60} materials might be susceptible to formation of an insulating ground state such as a charge- or spin- density wave[3], a transition to one of these states should produce a gapped Fermi surface and result in an activated ρ(T) below the transition. We do not observe activated behavior, but instead only a weakly nonmetallic behavior. This could possibly be due to an incomplete gapping of the Fermi surface, but given that other measurements do not see any evidence of a low-temperature phase in this material, we believe it to be unlikely.

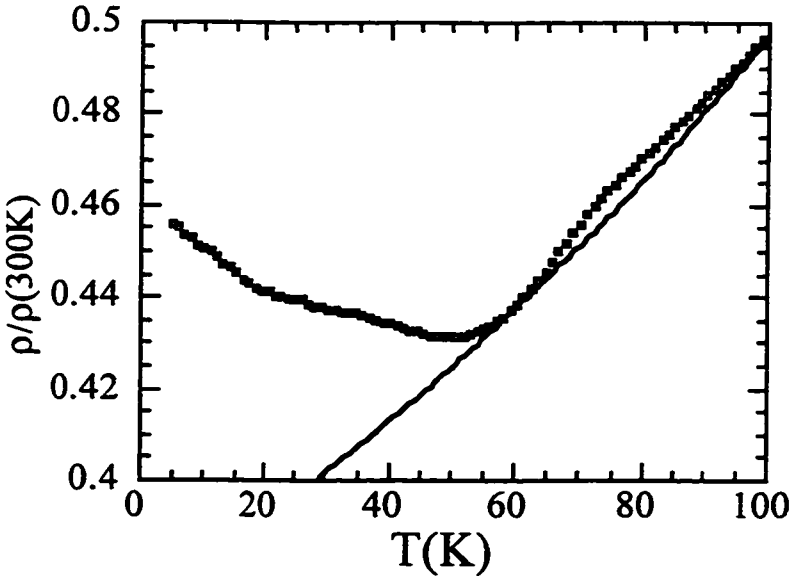

Figure 3.3 Low-temperature ρ(T) of KC_{60}.

Figure 3.4 shows the resistivity of KC_{60} over an extended temperature range. These data were taken on warming; just above 400 K, the resistivity of the sample increases dramatically, and the sample becomes insulating. This increase is the result of passing through the depolymerization transition; it is unclear whether the resistivity increase is due to intrinsically insulating behavior in the rocksalt phase, or whether the expansion of the lattice during depolymerization causes cracks to form in the sample. Because the crystal did not return to its conducting state upon cooling, we guess that the latter explanation is true.

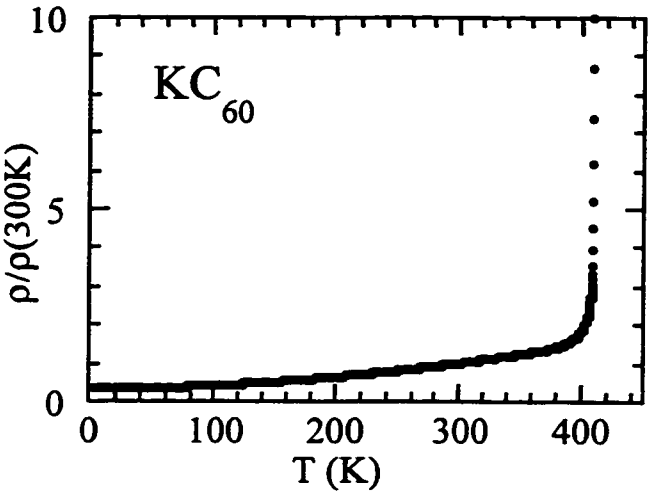

Figure 3.4 Depolymerization in KC_{60} above 400 K

3.3 R(T) of RbC_{60} and CsC_{60} at Ambient Pressure

A number of studies[4-7] have demonstrated that RbC_{60} and CsC_{60} are electronically different from KC_{60}, in spite of their structural similarity. Figure 3.5 shows the ρ(T) behavior of RbC_{60} and CsC_{60} at ambient pressure, from 300 K to 4.2 K. Both of these

materials display nonmetallic resistivity behavior at all temperatures, in contrast to the metallic behavior observed in KC_{60}. However, as was discussed above, many of these studies have also found evidence for a metal-insulator transition in RbC_{60} and CsC_{60} near 50 K. The dc resistivity we observe does not show any change in behavior at low temperature.

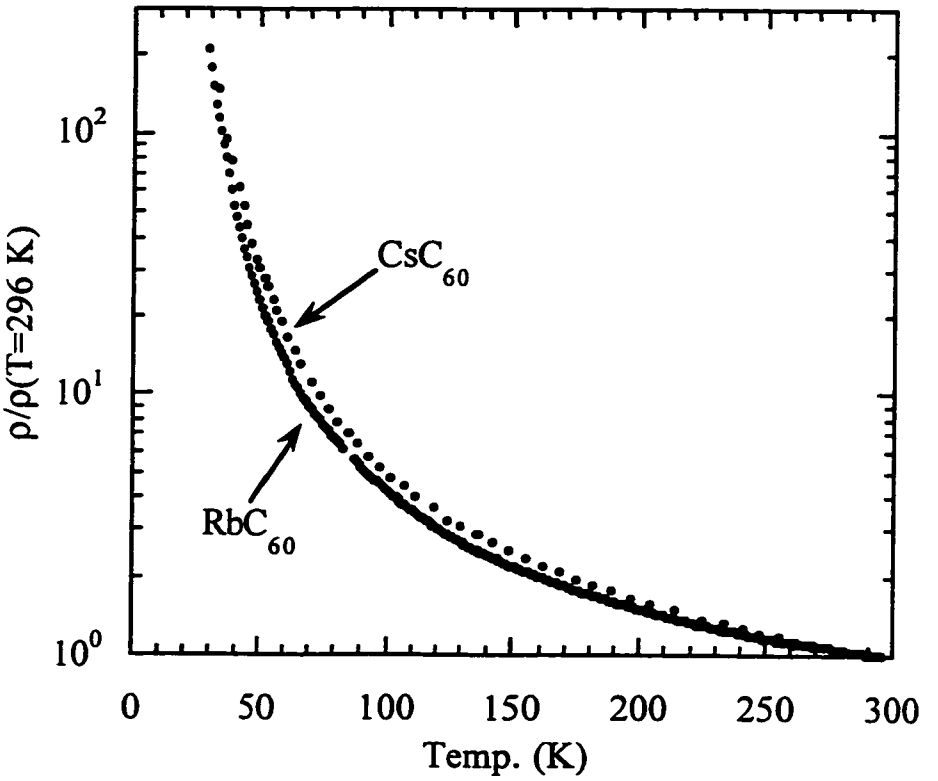

Figure 3.5 Ambient-pressure resistivity of RbC_{60} and CsC_{60}.

In an attempt to further understand the conduction mechanism in RbC_{60} and CsC_{60}, we have attempted to fit the data using a number of functional forms, including those which describe activated behavior and variable-range hopping (VRH) conduction in

1,2, and 3 dimensions. The best fit is obtained with a flucutation-assisted tunneling model[8], which is described by the functional form

$$\rho(T) = \rho_0 \exp\left(\frac{T_1}{T + T_0}\right). \tag{3.3}$$

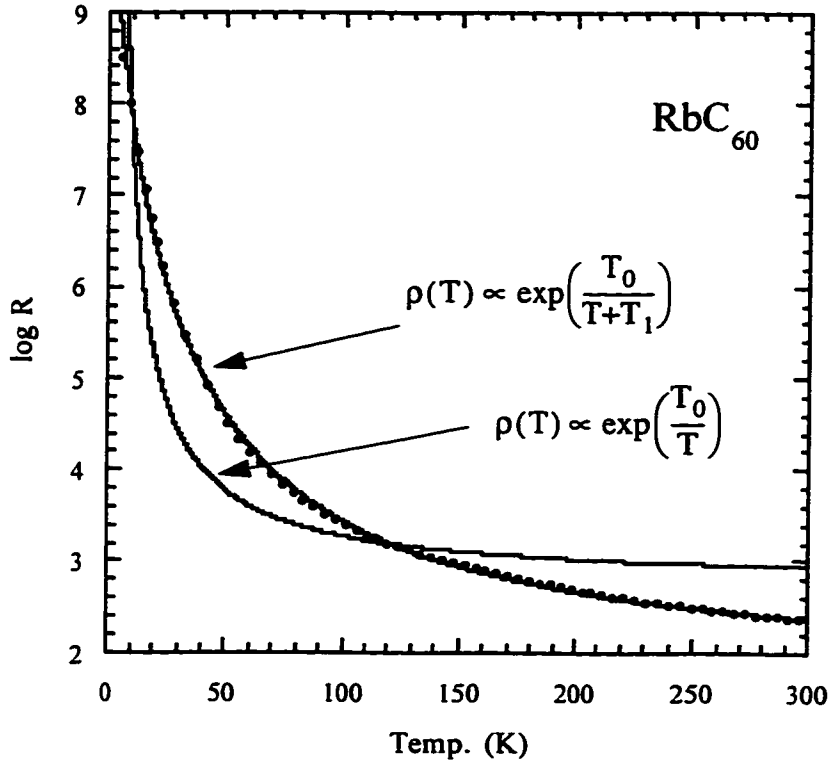

Figure 3.6 Functional fits to the $\rho(T)$ behavior of RbC_{60}.

Figure 3.6 shows a fit to the $\rho(T)$ behavior of RbC_{60} using eq. 3.1, with fitting parameters $T_1 = 95$ K, and $T_0 = 25$ K. In addition, a demonstrably worse fit, obtained using an acti-

vated form for the temperature dependence, is also shown for comparison; the standard expressions for VRH also do not fit as well as equation 3.3. We expect that thermal expansion will also play a large role in the transport behavior of this material, so that quantitative analysis of the functional form of $\rho(T)$ should require a constant-volume correction. However, the effects of thermal expansion should be less at the lowest temperatures, where the thermal expansion coefficient is small. At these temperatures, we clearly do not observe activated behavior, and thus believe that the transport at low temperatures is dominated by a tunneling-type mechanism rather than activation of carriers across a gap in the Fermi surface.

3.4 Magnetoresistance in AC_{60}.

Because of the observed antiferromagnetic ordering transition in RbC_{60} and CsC_{60}, we have searched carefully for any sign of magnetoresistance in all three AC_{60} materials. Our early efforts did yield a negative magnetoresistance for RbC_{60} at low temperature. This measurement proved to be spurious, however: the carbon glass resistors we were using for temperature control exhibit a small magnetoresistance, which causes the temperature controller to change the true temperature of the probe when the magnetic field is applied. Therefore, we switched to cernox resistors, which have a significantly smaller magnetoresistance. Figure 3.7 shows a typical plot of measured resistance vs. magnetic field for RbC_{60}, at 20 K, with the temperature measured with a cernox resistor. At this temperature, RbC_{60} shows no measurable magnetoresistance up to the maximum of 8 T. In fact, at no temperature is measurable magnetoresistance observed in any of the

AC_{60} materials. The lack of any magnetoresistance demonstrates that any low-temperature magnetic ordering which does occur in these materials does not couple appreciably into their dc transport behavior.

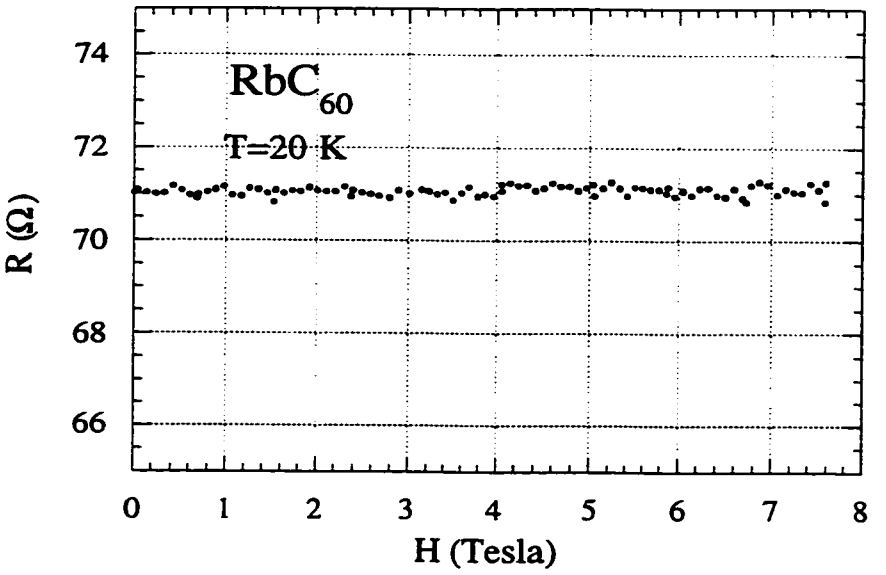

Figure 3.7 Resistance vs. magnetic field of RbC_{60} at 20 K

3.5 Resistivity Behavior of Mixed-Intercalant Species: $Rb_{1-x}K_xC_{60}$.

Because of the widely differing dc resistivity behavior of KC_{60} and RbC_{60}, we attempted to interpolate between the two by synthesizing a series of crystals with mixed intercalants, designated by $Rb_{1-x}K_xC_{60}$. This was done by inserting two types of alkali metal into the doping vessel at the same time, and then preparing doped crystals as was described in chapter 3. Three batches were prepared: one with $x \approx 0.1$, one with $x \approx 0.5$, and one with $x \approx 0.9$. Because of the somewhat uncontrolled doping conditions, the exact value of x varied among crystals in a single batch, as well as in different locations on a sin-

gle crystal. Nevertheless, examining the transport behavior of a series of these crystals is informative.

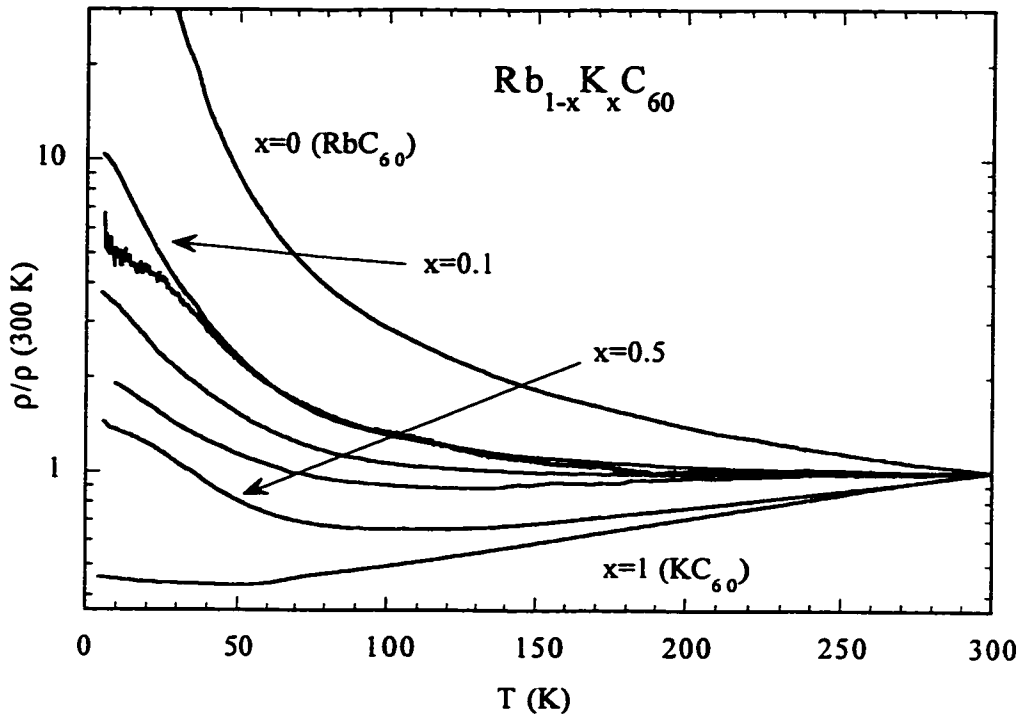

Figure 3.8 Resistivity of mixed-intercalant $Rb_{1-x}K_xC_{60}$.

Figure 3.8 shows the dc resistivity behavior of mixed-intercalant $Rb_{1-x}K_xC_{60}$ crystals, measured as a function of temperature from 300 K to 4.2 K. The resistivity of each sample is normalized to its room-temperature value to highlight the temperature-dependence of the resistivity. Two of the samples were analyzed using X-ray photoemission spectroscopy (XPS). By measuring the spectrum of the x-rays emitted from a sample as it is bombarded with electrons in a scanning electron microscope, this technique can identify individual elements in the sample, and give their relative stoichiometries. The two sam-

ples measured showed some variation (± 0.1) in the measured value of x in different locations. Clearly, however, the transport behavior of these samples changes dramatically even at small x, with the 4.2 K resistivity of the sample with $x \approx 0.1$ two orders of magnitude smaller than that of the pure RbC_{60} sample. Also, we note that the resistivity behavior of the mixed-intercalant samples interpolates smoothly between the behavior of KC_{60} and that of RbC_{60}. Therefore, the same mechanism may be responsible for the nonmetallic behavior in both materials.

3.6 Resistivity of KC_{60} Under Applied Hydrostatic Pressure

We were motivated to undertake a study of the pressure- and temperature-dependent resistivity of the AC_{60} compounds for three reasons. First, we hoped that by correcting for thermal expansion effects, we would be able to calculate the constant-volume resistivity of the A3C60 materials, so that a quantitative analysis of their transport behavior could be made. Second, KC_{60} and the Rb- and Cs-doped materials show strikingly different electronic properties, a difference which at the time was seemingly related only to the slightly smaller interchain distance in KC60. Thus we guessed that compression of the lattice of RbC60 should cause it to behave like KC60. We hoped to examine the details of this change in behavior. Finally, we hoped to suppress the nonmetallic behavior in these materials in the hope that they might superconduct. The high-pressure measurements described in this section were performed primarily by Kasra Khazeni, and have been published elsewhere[9-11].

Resistivity measurements were performed using a self-clamping hydrostatic pres-

sure cell, using Fluorinert FC-75 as a pressure medium. This technique has been extensively described elsewhere[12]. The sample is pressurized at room temperature using a hydraulic press; when the pressure (monitored continuously using a pressure-sensitive manganin coil) reaches the desired value, the pressure is locked in and the cell is cooled. Because of the differing thermal contraction of the pressure cell and pressure medium, the pressure in the cell decreases with decreasing temperature.

Figure 3.9 shows the resistivity vs. temperature of KC_{60} for a number of different applied room-temperature pressures. The measured resistivity is normalized to its room-temperature, zero-pressure value. The pressures at room temperature and 4.2 K are noted on each curve. The resistivity is highly pressure-dependent, decreasing by a factor of three at room temperature with application of 16 kbar. Furthermore, the nonmetallic behavior at low temperature is suppressed: the upturn in resistivity occurs at lower temperatures with increasing pressure, and is finally disappears completely between 3 and 5 kbar. In order to search for superconducting behavior in a completely metallic sample, we have cooled a sample pressurized to a 4. 2 pressure of $\approx$ 5 kbar to a temperature of 300 mK in a ^{3}He cryostat. Although the sample remained metallic, no superconductivity was observed.

3.7 R(P,T) of RbC_{60}.

Figure 3.10 shows the measured $\rho(P,T)$ behavior of RbC_{60}. This material is even more pressure-sensitive than KC_{60}, especially at the lowest temperatures, where application of only 0.5 kbar reduces the resistivity by four orders of magnitude. Also interesting

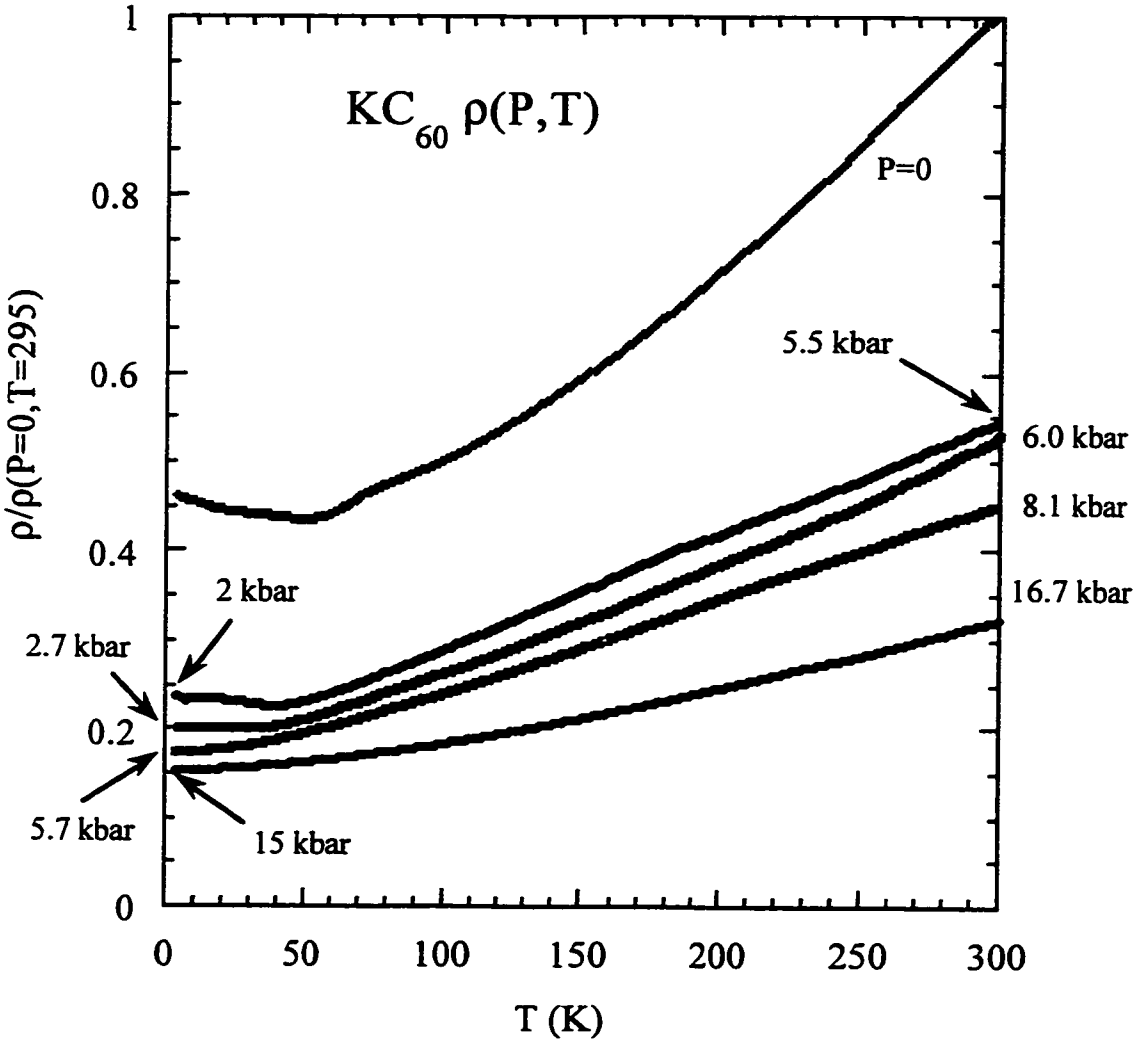

Figure 3.9 ρ(P,T) of KC_{60}. Due to thermal contraction, the applied hydrostatic pressure changes with temperature, and is monitored continuously with a calibrated manganin coil. The initial and final pressures are indicated on each curve.

is the change in the temperature dependence of the resistivity under applied pressure: RbC_{60} becomes metallic under moderate pressures. It is unclear whether this pressure is changing the electronic dimensionality and suppressing the low-temperature magnetic

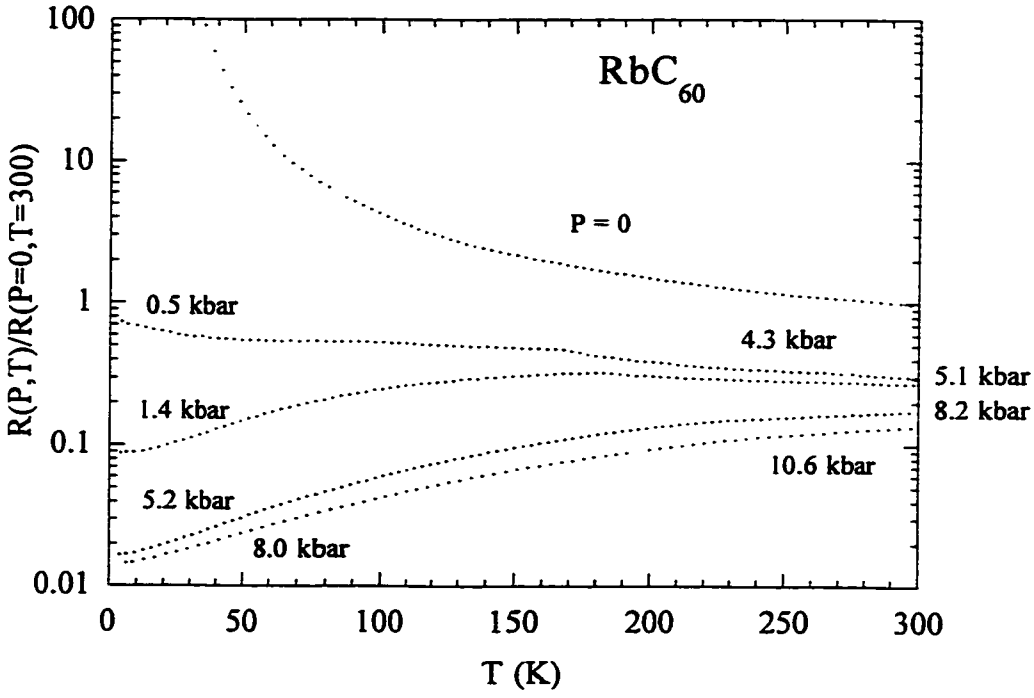

Figure 3.10 $\rho(P,T)$ of RbC_{60}.

transition in RbC_{60}; ESR measurements[5] have seen the persistence of the magnetic ground state up to pressures of 4 kbar, while we see substantial metallization of the sample at lower pressures.

Figure 3.11 highlights the nonmetallic-metallic transition in RbC_{60}. One would expect a gradual change in behavior from nonmetallic to metallic as the RbC_{60} lattice is compressed toward the KC_{60} structure. However, when the resistivity curves are examined closely, sharp changes in the resistivity behavior are observed. This transition is most prominent in the second curve from the top, which shows a sharp transition from nonmetallic to metallic behavior occurring at a pressure of 3.3 kbar and a temperature of 180 K.

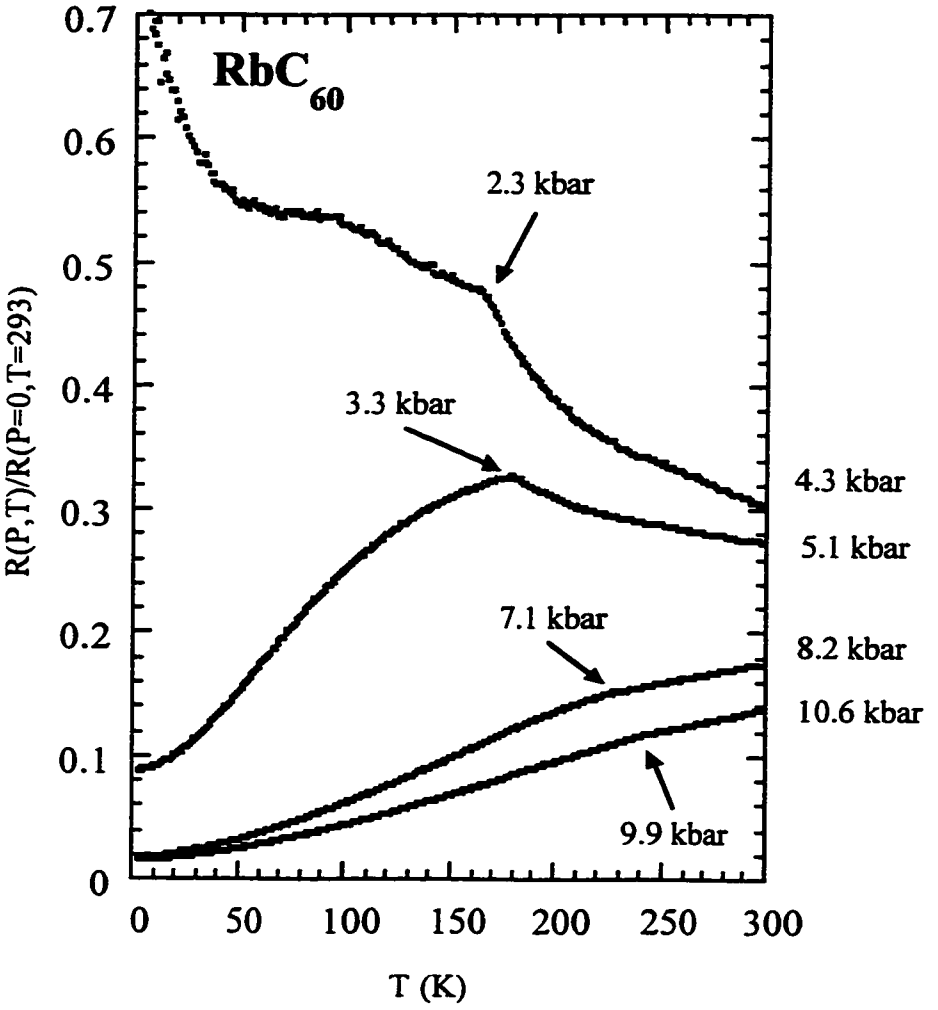

Figure 3.11 Sharp transition in the temperature dependence of ρ(T) of RbC_{60} under pressure. The labels mark the pressures at which the transition occurs.

In fact, however, the transition, seen as a discontinuity in the slope of the resistivity vs. temperature, occurs in all curves except the zero-pressure curve, and can separate regions of either metallic or nonmetallic behavior. However, the region below the transition is always more metallic than the region above the transition, in that there is an increase in dρ/dT upon cooling.

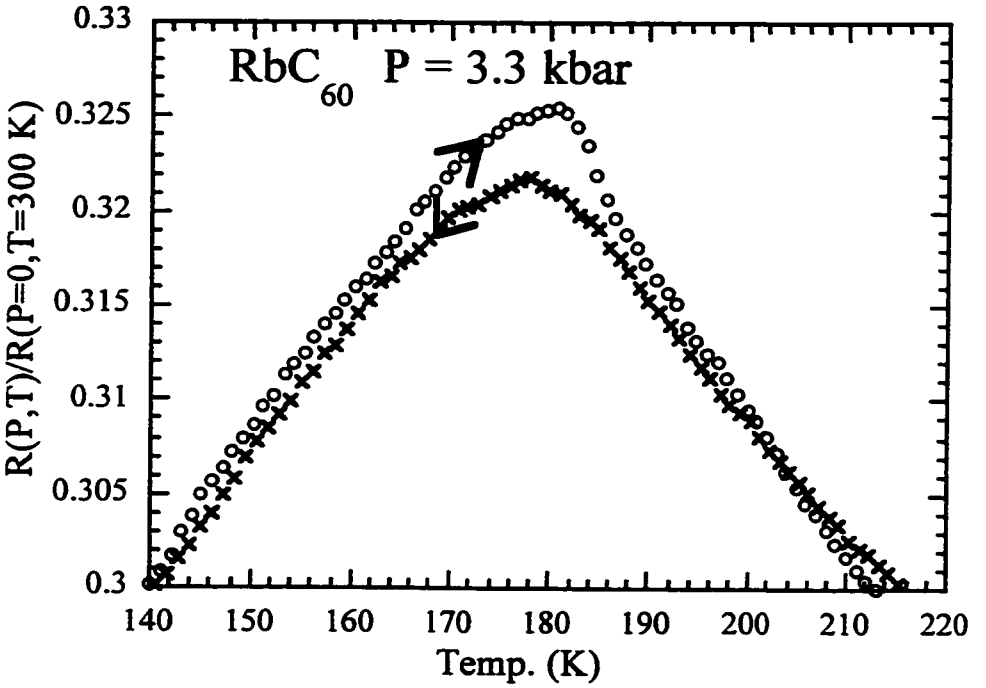

Figure 3.12 Hysteresis in RbC_{60} $\rho(P,T)$

Figure 3.12 shows the region around the 3.3 kbar, 180 K transition. The data taken on warming and cooling, as indicated by the arrows on the figure, diverge near the transition. This hysteresis, indicative of a first-order phase transition, is consistent with a structural phase transition. The sharp hysteretic transition indicates that there is a structural difference between KC_{60} and RbC_{60} aside from the differences in their lattice constants.

3.8 Constant-Volume Resistivity of KC_{60} and RbC_{60}.

There are two main motivations for correcting for thermal expansion effects to obtain the constant-volume resistivity of the AC_{60} materials. First, as was mentioned previously, theoretical predictions for transport behavior are done at constant volume, and therefore the experimental data must be corrected for thermal expansion before it is com-

pared to standard models. In addition, the transition observed in RbC_{60}, and the similarity of the transport behavior in KC_{60} and RbC_{60} in the pressure-induced metallic phase warrants careful examination of the constant-volume resistivity. The calculation of the constant-volume behavior was performed primarily by Vincent Crespi.

The constant-volume resistivity of KC_{60} and RbC_{60} was calculated using the measured $\rho(P,T)$ data, the previously-published thermal expansion coefficient (α) for KC_{60} (3.1×10^{-5} $kbar^{-1}$, assumed to be equal for RbC_{60}), and the measured bulk modulus (B) for both materials (chapter 4). The thermal expansion coefficient was assumed to be constant to 30 K and have a T^3 temperature dependence below that temperature; the bulk moduli were assumed to be constant in temperature and pressure. At a number of temperatures, curves of resistivity vs. pressure were constructed from the measured data and fitted to a smoothly-varying function to allow for interpolation between the measured data points.

As a sample warms from a temperature T to $T+\Delta T$, thermal expansion causes it to expand by a volume $\Delta \ln V = 3\alpha\Delta T$. To correct for this expansion, a pressure $P = B\ln V = 3\alpha B\Delta T$ must be applied. The corresponding constant-volume resistivity can then be calculated using

$$\rho(T+\Delta T)|_V = \rho(T+\Delta T)|_P \times \frac{\rho(P+3\alpha B\Delta T)}{\rho(P)}, \tag{3.4}$$

where the last term is calculated from the resistivity vs. pressure plots.

Figure 3.13 shows the constant-volume resistivity of KC_{60}, with the zero-pressure data superposed for comparison. The labels represent multiples of the zero-pressure vol-

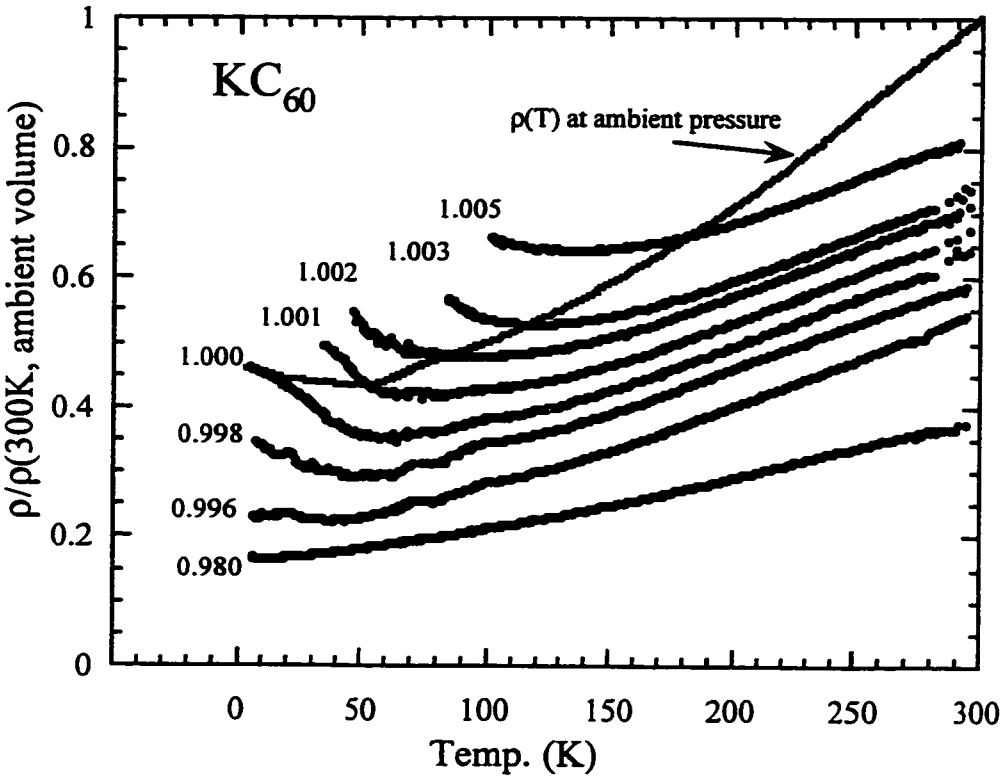

Figure 3.13 Constant-volume resistivity of KC_{60}.

ume at 4.2 K; thus the curve labeled 0.998 represents the resistivity of a sample which has been compressed by 0.2% at 4.2 K, and then held at that volume as it is warmed. Two features are evident here. First, the nonmetallic transition moves upward in temperature as the volume is increased. Second, the constant-volume resistivity above the nonmetallic region is substantially closer to linear in temperature than is the zero-pressure resistivity. This supports the earlier hypothesis that the curvature was due to thermal expansion; above the nonmetallic region, KC_{60} seems to be a normal metal with a linear temperature-dependent resistivity.

Figure 3.14 shows the constant-volume resistivity of RbC_{60}, shown as a series of curves at multiples of the zero-pressure, 4.2 K volume, as in the previous plot. The cor-

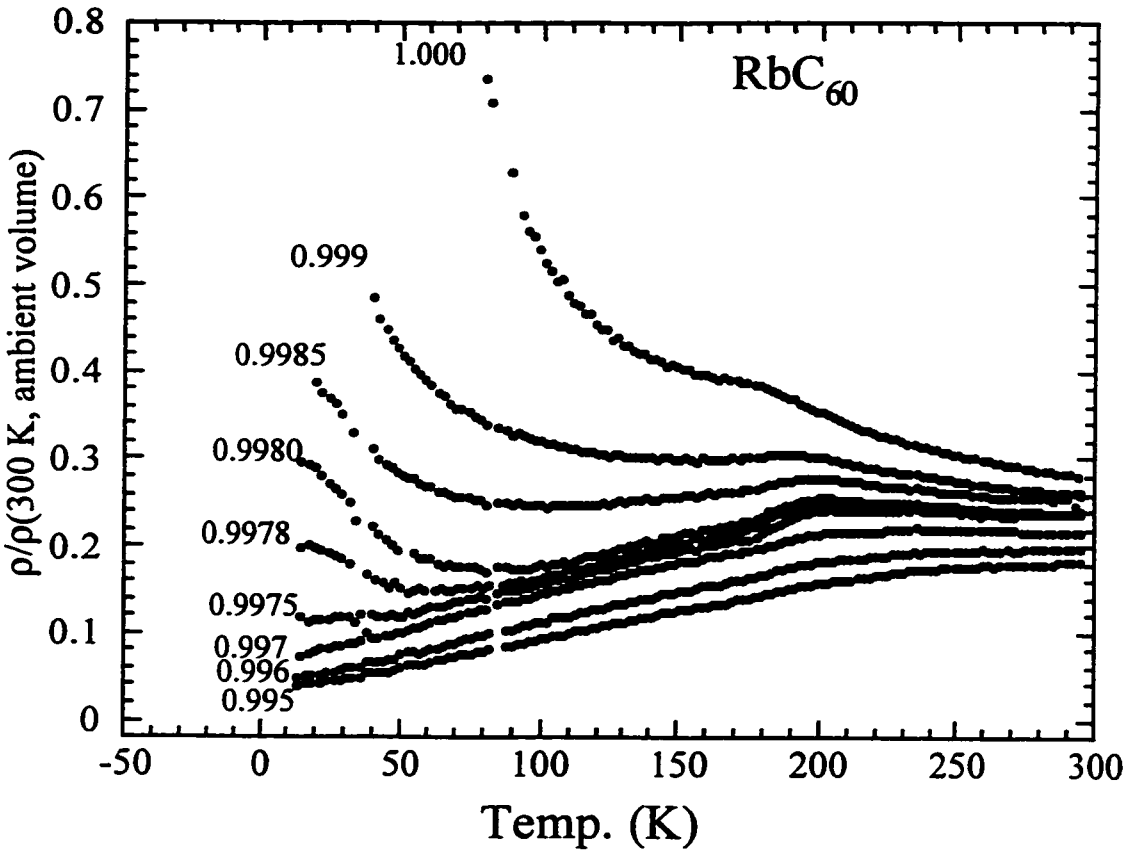

Figure 3.14 Constant-Volume Resistivity of RbC_{60}.

rection to constant volume clarifies the character of the resistive transition seen in figure 3.11, as well as the character of the phases above and below the transition. At low volume, below the transition, RbC_{60} is metallic with a nonmetallic low-temperature behavior. The onset of nonmetallic behavior moves upward in temperature with increasing volume. Above the transition, RbC_{60} is metallic at low volumes and nonmetallic at higher volumes. In all cases, the transition marks a change toward less metallic behavior upon warming.

Although quantitative comparisons between the curves are difficult because of

experimental uncertainties, it is clear that there is a great similarity between the behavior of KC_{60} and that of RbC_{60} below the resistive transition. If the resistive transition reflects a structural phase transition, then the structure of RbC_{60} below the transition should be similar to that of KC_{60}, while the structure above the transition would then be different. The strongest candidate for this structural difference seems to be a difference in chain orientation; the final results from the single-crystal XRD study (section 3.6) should help illuminate this issue.

3.9 Thermopower of KC_{60} and RbC_{60}.

The thermopower (TEP) of a material is defined as

$$S = \frac{E}{\nabla T}. \tag{3.5}$$

In a normal metal, calculation of the TEP using Boltzmann transport theory leads to the Mott formula[13]:

$$S = -\frac{k_B^2 T}{|e|}\frac{d}{d\varepsilon}(\ln\sigma). \tag{3.6}$$

For electron-like conduction, the conductivity σ increases with an increase in the Fermi level, so that the thermopower is negative, while for a hole-like system the conductivity decreases and the thermopower is positive; in both cases, the thermopower is linear in temperature. The Mott expression can be further simplified by using a free-electron (parabolic band) model to:

$$S = -\frac{\pi^2 k_B^2}{6|e|}\frac{T}{\varepsilon_F} \tag{3.7}$$

Thus the slope of the linear S vs. T can, in a free-electron model, give the Fermi level if the variation in the scattering time is negligible. For a semiconductor, a simple model using Boltzmann theory leads to the following form:

$$S_{semi}(T) = \frac{k_B}{e}\left(\frac{\varsigma}{T} + \frac{\partial \ln \tau}{\partial \ln \varepsilon} + \frac{5}{2}\right), \tag{3.8}$$

where ζ represents the energy distance between the conduction band and the Fermi level, expressed in units of temperature. In contrast to the linear temperature dependence observed in metals, a semiconductor should have a thermopower which is inversely temperature dependent. Thus we can learn a number of things by measuring the thermopower of the AC_{60} compounds. In the metallic state, we can hope to measure the sign of the carriers and possibly information about the location of the Fermi level. If the system undergoes a true transition to a true semiconducting state, the thermopower should then display a (1/T) dependence. On the other hand, other mechanisms which cause nonmetallic resistivity behavior, such as localization, do not necessarily result in a nonmetallic thermopower.

Thermopower was measured in a two-probe fashion using the apparatus and software described in appendix A. Crystals of KC_{60} and RbC_{60} were connected to the stages of the thermopower probe using multiple 1/2-mil gold wires to provide a good thermal contact to the stages. The wires were attached to the samples using silver paint, and were bent for stress relief.

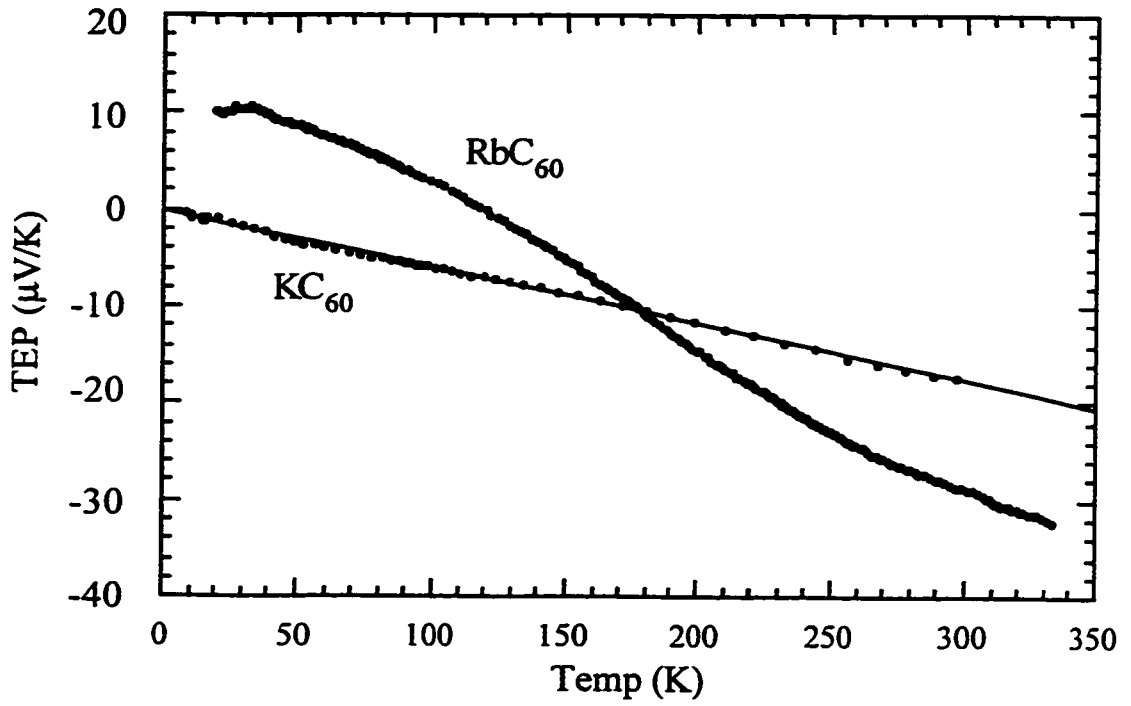

Figure 3.15 Thermopower of KC_{60} and RbC_{60}.

Figure 3.15 shows the thermopower of KC_{60} and RbC_{60} as a function of temperature. The thermopower of KC_{60} is linear in temperature, as can be seen from the straight-line fit through the data points. The linear thermopower indicates that KC_{60} has a metallic density of states at the Fermi level at all temperatures. Thus we see no sign in the TEP of the nonmetallic behavior seen in the resistivity at low temperature. The TEP of KC_{60} is negative, indicating electron-like conduction. If we use Eq. 3.7, we obtain a value of 0.22 eV for the Fermi level for this material.

RbC_{60}, on the other hand, displays a distinctly different thermopower. It is negative at room temperature, but then actually crosses zero and becomes negative below $T \approx 120$ K. The low-temperature behavior of RbC_{60} does not show any sign of semiconduct-

ing behavior. The results so far are inconclusive, however: all of the samples measured have had contacts which go bad below ≈ 40 K, exactly the temperature below which we are looking for evidence of an insulating ground state. The zero-crossing in the TEP leads us to speculate that RbC_{60} is quite near to the boundary between electron-like and hole-like conduction, and that the thermal contraction of the sample upon cooling causes it to traverse that boundary. In a tight-binding model, the boundary between electron-like and hole-like conduction is at half filling. Recent theoretical work[14] has examined the possibility of an insulating ground state in the AC_{60} materials as being the result of half-filled bands rather than a quasi-one-dimensional electronic structure. These results lend support to that model, in that RbC_{60} seems to be near half filling while KC_{60} does not.

Chapter 3 References

1. X. D. Xiang, J. G. Hou, G. Briceno, *et al.*, Science **256**, 1190-1 (1992).

2. W. A. Vareka and A. Zettl, Physical Review Letters **72**, 4121-4 (1994).

3. O. Chauvet, G. Oszlanyi, L. Forro, *et al.*, Physical Review Letters **72**, 2721-4 (1994).

4. F. Bommeli, L. Degiorgi, P. Wachter, *et al.*, Physical Review B (Condensed Matter) **51**, 14794-7 (1995).

5. L. Forro, G. Baumgartner, A. Sienkiewicz, *et al.*, in *Fullerenes and Fullerene Nanostructures: Proceedings of the International Winterschool on Electronic Properties of Novel Materials*, edited by H. Kuzmany, J. Fink, M. Mehring and S. Roth, (World Scientific, River Edge, NJ, 1996), p. 102-9.

6. H. Alloul, V. Brouet, E. Lafontaine, *et al.*, Physical Review Letters **76**, 2922-5 (1996).

7. V. Brouet, H. Alloul, A. Janossy, *et al.*, in *Molecular Nanostructures: Proceedings of the International Winterschool on Electronic Properties of Novel Materials*, edited by H. Kuzmany (World Scientific, River Edge, NJ, 1997), p. 328-332.

8. S. Roth, *One-dimensional metals : physics and materials science* (Vch, New York, 1995).

9. J. Hone, K. Khazeni, and A. Zettl,in *Fullerenes and Fullerene Nanostructures: Proceedings of the International Winterschool on Electronic Properties of Novel Materials*, edited by H. Kuzmany, J. Fink, M. Mehring and S. Roth, (World Scientific, River Edge, NJ, 1996), p. 115-18.

10. K. Khazeni, J. Hone, N. G. Chopra, *et al.*, Applied Physics A (Materials Science Processing) **64**, 263-9 (1997)

11. K. Khazeni, V. H. Crespi, J. Hone, *et al.*, Physical Review B (Condensed Matter) **56**, 6627-30 (1997).

12. K. Khazeni, PhD thesis(University of California, Berkeley, 1997).

13. F. J. Blatt, *Thermoelectric power of metals* (Plenum Press, New York, 1976).

14. M. Fally and H. Kuzmany, Physical Review B (Condensed Matter) **56**, 13861-4 (1997).

Chapter 4.

High-pressure Structural Study of AC_{60}.

4.1 Motivation

We were motivated to undertake a high-pressure structural study of the AC_{60} materials for a number of reasons. First, a determination of the bulk modulus of these materials was required in order to perform the constant-volume correction described in section 3.8. Second, the bulk modulus was expected to be highly anisotropic due to the polymerization in these materials. Third, by extrapolating the Tc vs. P behavior of the pressure-induced transition in RbC_{60}, we predicted a room-temperature phase transition near 15 kbar (1.5 GPa); we hoped to see evidence of a structural phase transition at this point. Finally, pristine C_{60} can polymerize in a variety of ways under pressure[1]; we wanted to examine whether this would occur in a doped system. This high-pressure structural study was undertaken in collaboration with Jeffrey Nguyen and Raymond Jeanloz.

4.2 Experimental Technique

The structure of the AC_{60} materials under pressure was determined by x-ray diffraction (XRD) in a diamond anvil cell (DAC). The cell used was a Merrill-Bassett type, as diagrammed in figure 4.1. The two diamonds are glued to circular backing plates; the top plate has a small hole to permit the incoming x-ray beam to enter the cell, while the

bottom plate is slotted at an angle to allow the scattered radiation to escape. The backing plates are held by triangular steel plates. The sample (in this case, AC_{60} crystals were ground into powder) is placed in a hole in an indented spring-steel gasket, in a pressure medium of 4:1 methanol-ethanol, and compressed between the two diamonds. Small ruby chips are included for pressure measurement, and a small flake of gold is attached to the back of the bottom diamond to calibrate the distance from the diamond cell to the image plate. Pressure is applied by tightening three screws at the corners of the cell.

After loading the samples into the DAC, we attempted to apply small amounts of pressure initially and then take spectra in increments while increasing pressure; however, it proved difficult to seal the pressure medium between the diamonds at low pressure, and most of the data were taken by applying high pressure initially and measuring upon decreasing pressure.

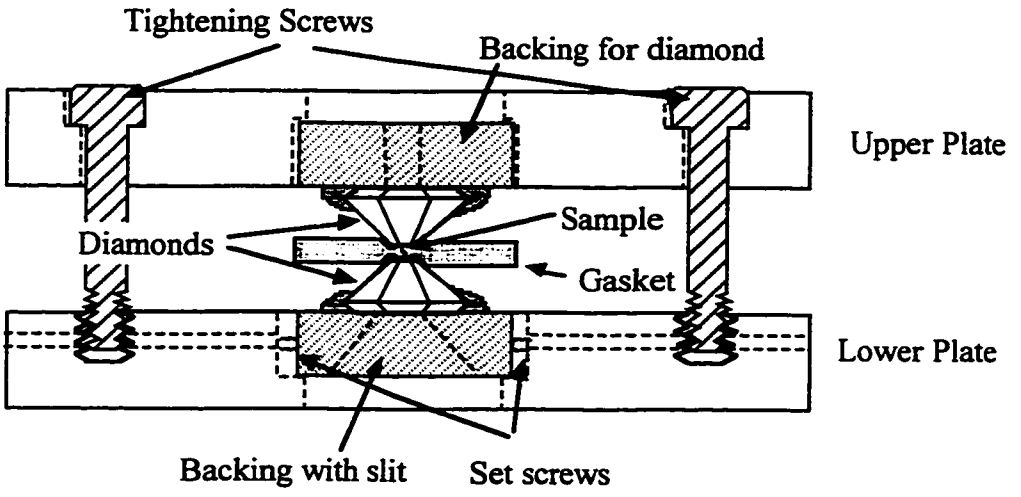

Figure 4.1 Merill-Bassett Diamond Anvil Pressure Cell

Because of the small size of the samples used in a DAC, it can take as much as a

month to obtain a single diffraction spectrum using a tabletop x-ray source. Therefore, it is necessary to use a high-flux synchrotron source in order to obtain spectra in a reasonable amount of time. This study was done at beamline 10-2 at the Stanford Synchotron Radiation Laboratory; each spectrum required only 30 minutes of exposure. Diffraction patterns were collected using an image plate is mounted on a holder aproximately 20 cm away from the center of the DAC, which is centered on a collimated beamline; the distance to the image plate is calibrated at the beginning of the run using diffraction from a gold standard. We also found it necessary to make sure that the image plate holder was exactly perpendicular to the beam; this was accomplished by adjusting the angle of the image plates using micrometers until a circular diffraction pattern was obtained.

The diffraction pattern of the sample was taken for 30 minutes at each pressure; before taking the spectrum, the pressure in the DAC was measured using ruby fluorescence.

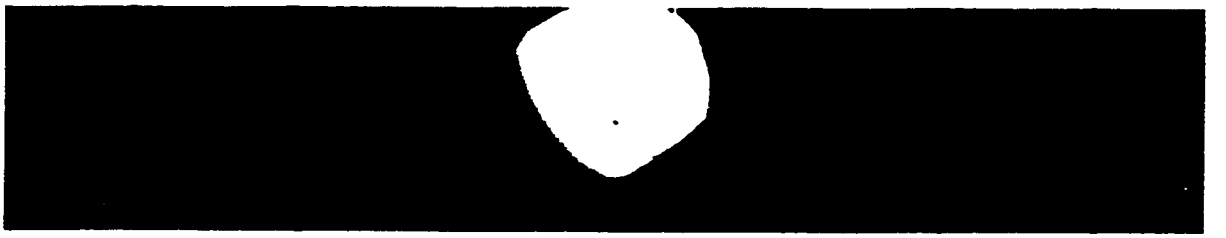

Figure 4.2 Powder x-ray diffraction pattern of RbC_{60} in the DAC

Figure 4.2 shows a sample diffraction pattern of RbC_{60}. In this image, dark corresponds to a high intensity of x-rays: the diffraction peaks appear as pairs of arcs on the left and right side, and the white area in the center is from a lead shield used to block the unscattered beam. After exposure, the image plate is scanned and the above digital image

recorded.

Figure 4.3 shows the next two steps in the analysis of the diffraction pattern. To convert a pattern into one-dimensional powder diffraction spectrum, its intensity is integrated over all angles using a custom-written computer program, producing a 1-D spectrum like the one labelled 'raw spectrum' in the figure. Diffuse scattering leads to a large smooth background in this spectrum; the background is subtracted by running the data through a high-pass filter, producing the spectrum labelled 'filtered spectrum'. In this spectrum, the peaks at low distance correspond to RbC_{60}, while the large peak at $\approx$ 8.5 cm is from the gold calibrant. The location of this peak is used to calibrate the distance (y) from the diamonds to the image plate

The angle by which the x-rays are scattered can be determined from the sample-film distance (y) and the and the location (x) of an individual peak:

$$\phi = \operatorname{atan}\frac{x}{y}. \tag{4.1}$$

This angle is related to the angle of incidence of the incoming beam to a given Bragg plane by

$$\sin\phi = \sin(2\theta), \tag{4.2}$$

so that the spacing between Bragg planes in the sample (the 'd-spacing') is given by (using the Bragg criterion)[2]

$$d = \frac{\lambda}{2\sin\left(\frac{1}{2}\operatorname{atan}\frac{x}{y}\right)}. \tag{4.3}$$

Alternately, d-spacing can be converted to distance by inverting equation 4.3.

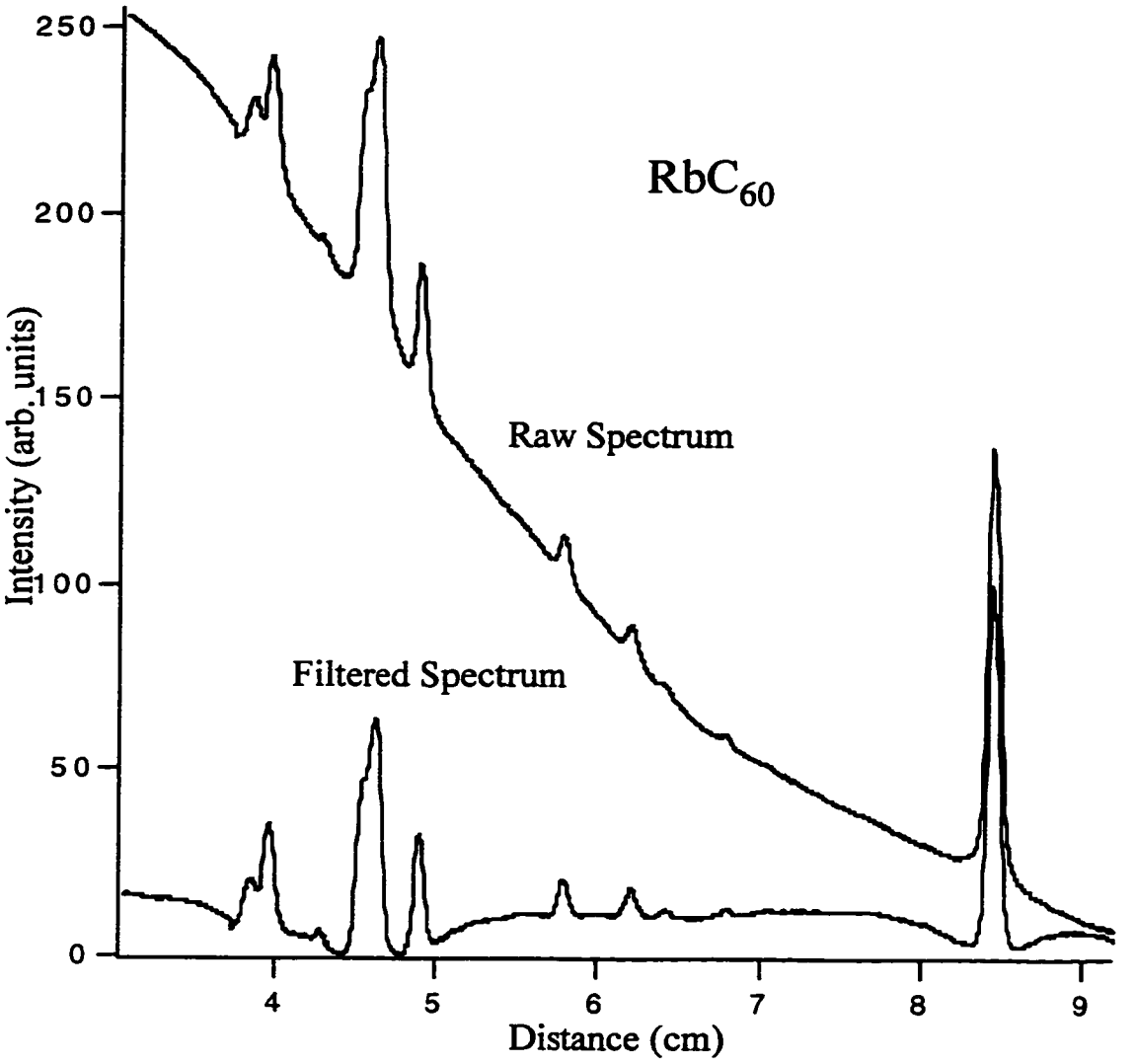

Figure 4.3 Raw and filtered diffraction spectra of RbC_{60}.

To measure the lattice constants of the samples from the diffraction patterns, it was first necessary to index the observed peaks. This was done by performing forward-scattering calculations using the published structures of KC_{60} and RbC_{60}. Figure 4.4 shows a section of the diffraction pattern obtained for RbC_{60} at zero pressure and at 1.5 and 3.2 GPa, superposed with the peaks obtained from the forward scattering. To a large extent, the observed zero-pressure peaks match the predicted peaks; small discrepancies can be

due to impurity phases or the intrinsic uncertainty of the forward-scattering procedure. As the sample shrinks under pressure, the peaks shift to a smaller d-spacing, and the peaks move outward on the image plate. In addition, the peaks broaden and weaken, due to a non-hydrostatic pressure distribution in the sample space. At each pressure, the location of the indexed peaks was measured by fitting the peaks to a Gaussian form; some of the peaks are superposed and require a multiple Gaussian fit. Finally, the orthorhombic lattice vectors were determined by a least-squares fit to the locations of the indexed peaks.

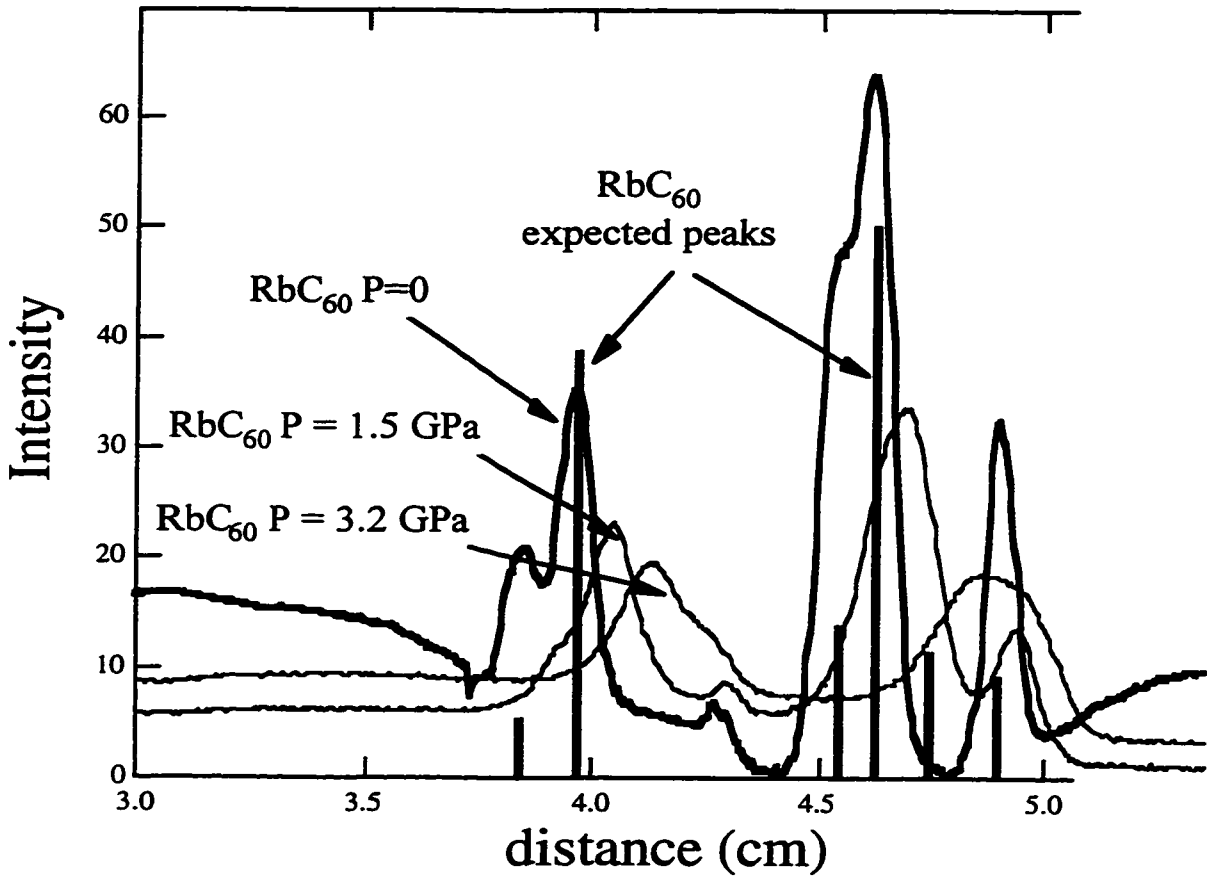

Figure 4.4 RbC_{60} spectra at zero and high pressure

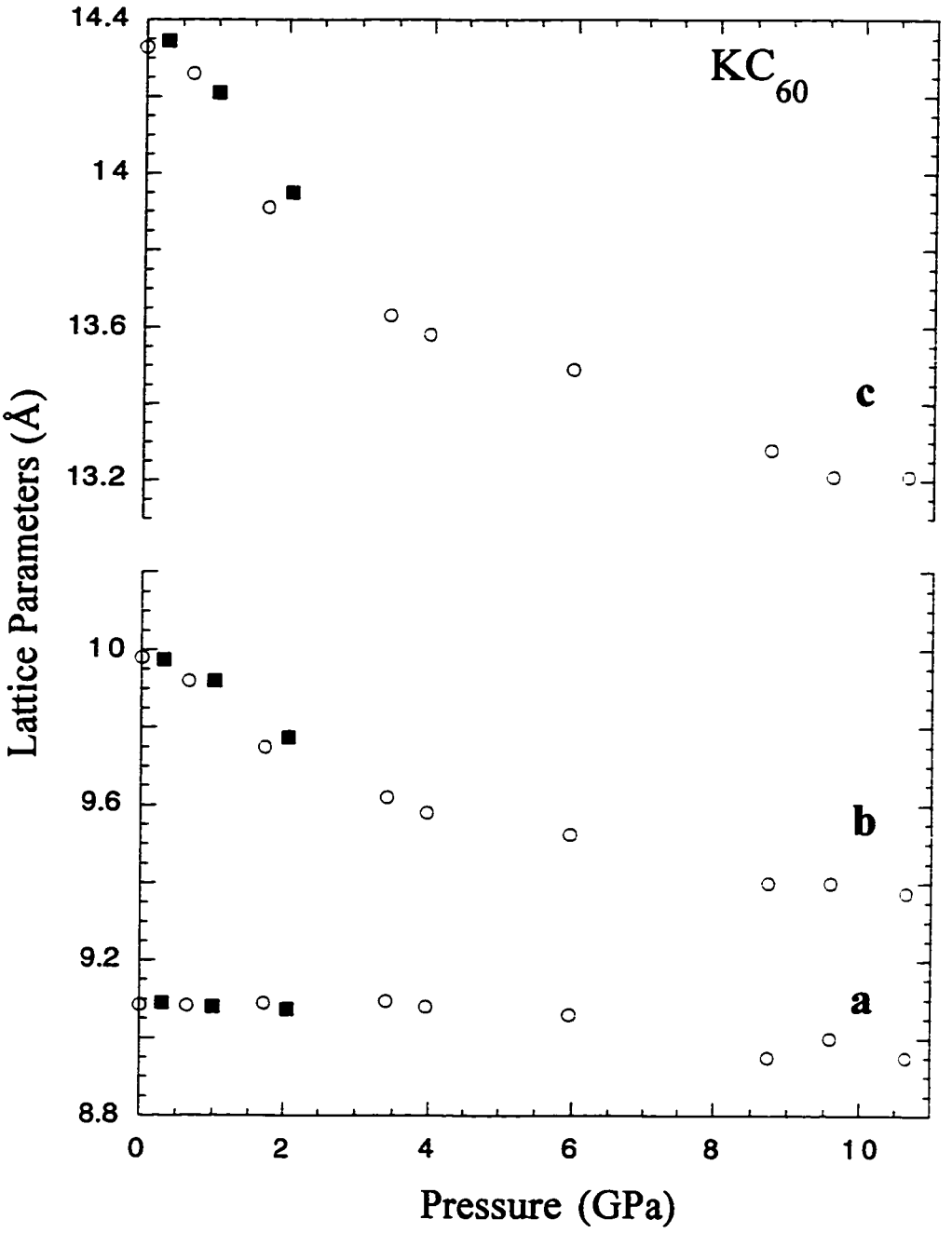

Figure 4.5 Lattice parameters of KC_{60} under applied pressure. The different symbols refer to different samples. Solid symbols represent data taken upon compression; open symbols represent data taken upon decompression

Figure 4.5 shows the pressure-dependence of the lattice parameters of KC_{60}. Two data sets are represented: the solid squares are taken from one sample upon compression, while the open circles are derived from a second sample, measured on decompression. Due to the difficulty in extracting three independent lattice parameters from the data, there is considerable scatter in the data points; nevertheless, the broad features of the behavior of KC_{60} under pressure are clear. KC_{60} has a highly anisotropic compressibility: it is soft in the **c** and **b** directions and quite rigid in the **a** direction, reflecting the polymerized nature of the material. No sudden change in the lattice constants, which might reflect a structural phase transition, is apparent; however, such a change in lattice constant could easily be smaller than the resolution of the experiment.

Figure 4.6 represents the behavior of RbC_{60} under applied pressure. The data in this case are from three different samples, represented by circles, squares, and triangles. As in the previous plot, solid symbols represent data taken on compression, while open symbols represent data taken on decompression. On compression, RbC_{60} behaves in a manner similar to KC_{60}: it compresses significantly in the **b** and **c** directions, is stiff in the **a** direction, and does not show any abrupt changes in lattice constant with pressure. A saturation seems to occur at 8 GPa; above that pressure, RbC_{60} shows significantly reduced compressibility. In striking contrast to KC_{60}, RbC_{60} shows significantly different behavior on compression and decompression. In the sample measured to the highest pressures (represented in figure 4.5 by the circles), the **c** lattice parameter remains almost constant upon decompression until pressures below 1 GPa. At low pressure, the sample slowly (on the order of one hour) relaxes and moves toward its zero-pressure structure. This behavior also seen in a second sample (represented by triangles), which was compressed only to 5

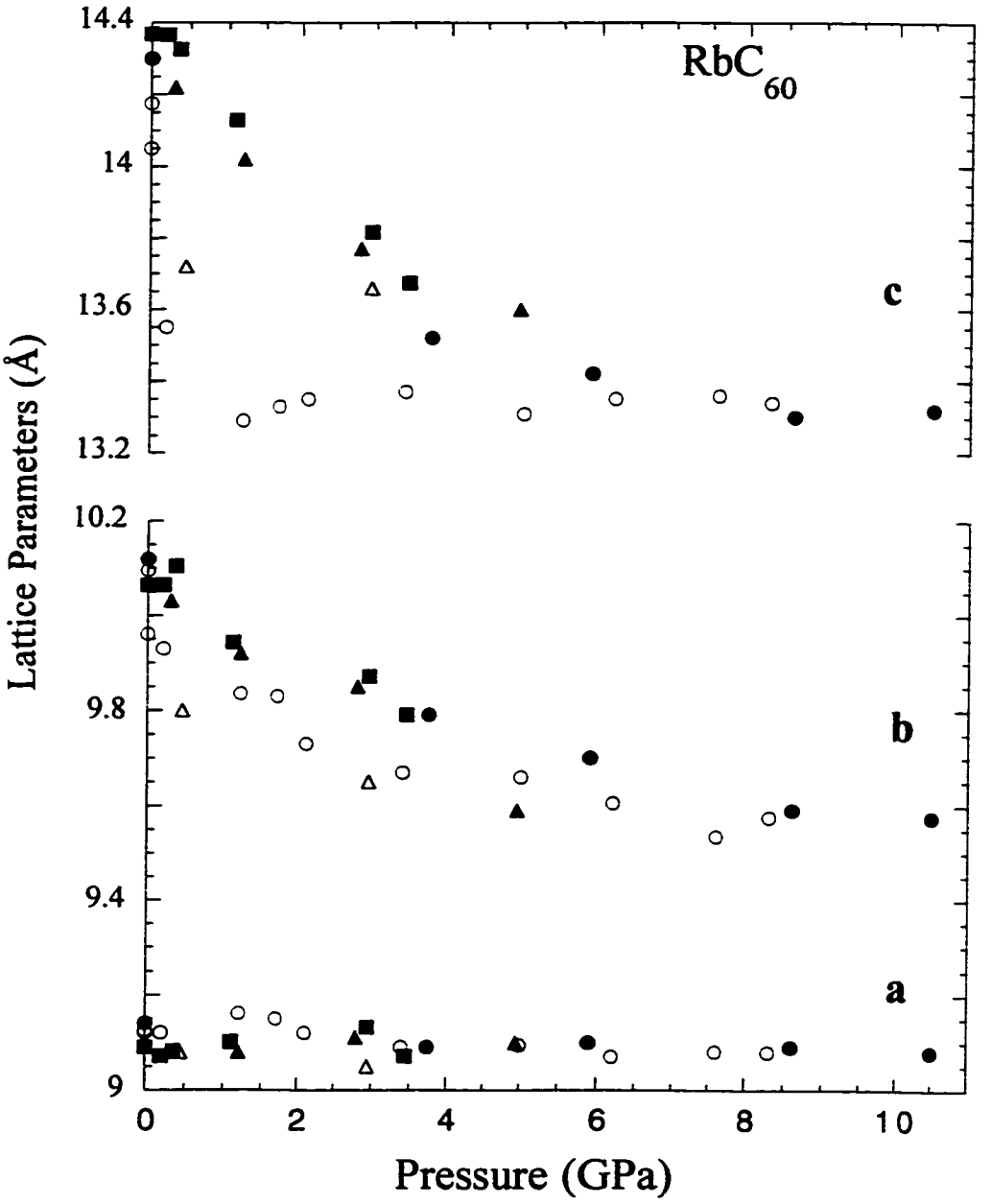

Figure 4.6 Lattice parameters of RbC_{60} under applied pressure. The different symbols refer to different samples. Solid symbols represent data taken upon compression; open symbols represent data taken upon decompression

GPa. Hysteretic behavior is also seen in the **b** parameter: the data taken on decompression are consistently below the data taken on compression. However, because the hyster-

esis is significantly stronger in the c direction, is not likely to be an experimental artifact. We are still in the process of attempting to understand this behavior, but it is consistent with the formation of a metastable phase with some type of covalent bonding between chains.

4.4 Bulk Moduli of KC_{60} and RbC_{60}.

As was mentioned above, a significant motivation for this experiment was to determine the bulk moduli of KC_{60} and RbC_{60}, in order to perform the constant-volume correction to the measured resistivity. The bulk modulus of a material is given by:

$$B = -V\left(\frac{\partial P}{\partial V}\right). \tag{4.4}$$

A material will generally become stiffer as it is compressed, and thus the bulk modulus is in general a function of pressure (or volume). To obtain a bulk modulus as a function of pressure, one generally fits the V vs. P data to a model equation of state. A simple semiempirical form is the Murnaghan equation[3]:

$$P = \frac{B_0}{B'}\left[\left(\frac{V}{V_0}\right)^{-B'} - 1\right], \tag{4.5}$$

Where B_0 is the zero-pressure bulk modulus, and B' is the derivative of B_0 with respect to pressure.

Figure 4.7 represents the normalized unit cell volume of KC_{60} and RbC_{60} as a function of pressure. Both materials show similar behavior, with the volume decreasing rapidly with pressure at low pressure, and then levelling off at high pressure, although

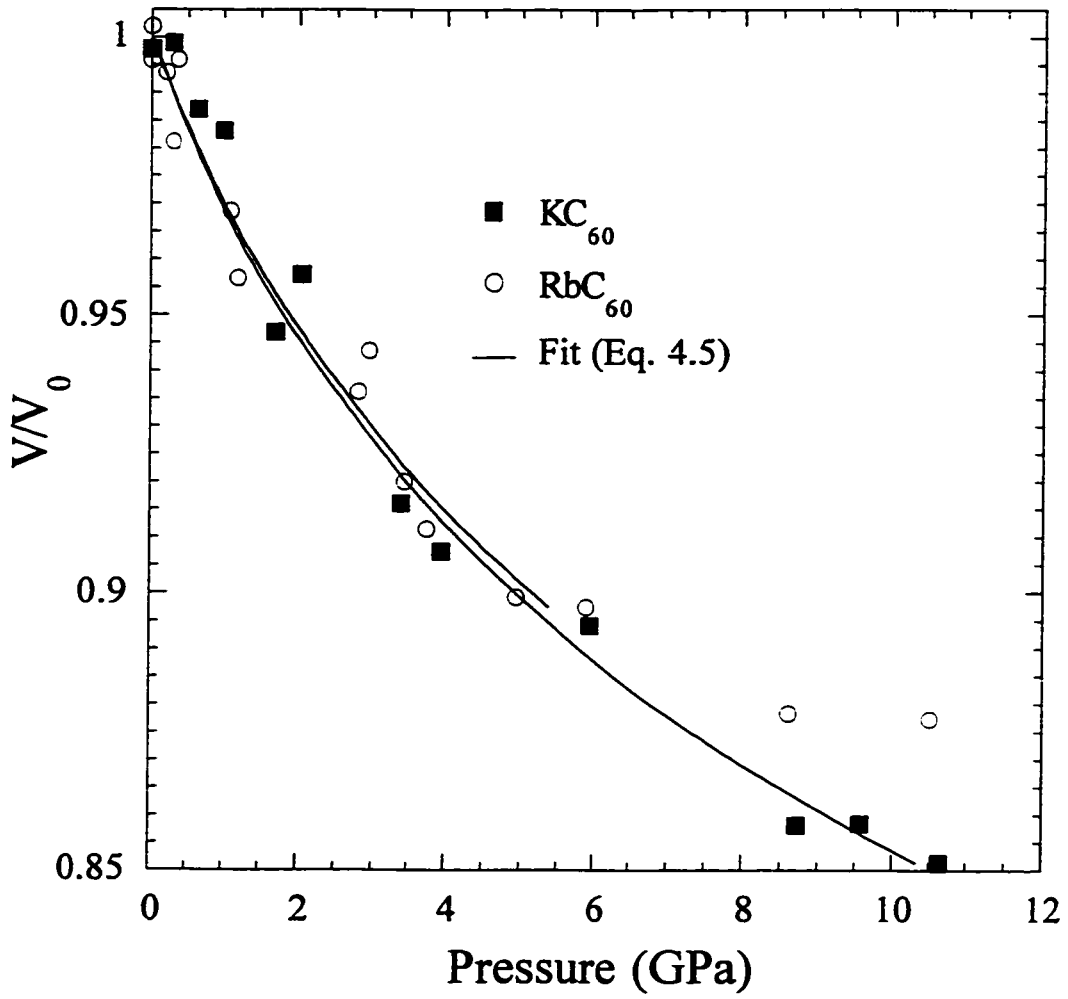

Figure 4.7 Normalized unit-cell volumes of KC_{60} and RbC_{60}, with fits to a simple equation of state (eq. 4.5).

RbC_{60} shows a more prominent plateau above 8 GPa. The solid lines in the plot represent fits of the data to equation 4.5; the upper fit, for RbC_{60}, is only performed using the data below 8 GPa to eliminate any effects from the high-pressure saturation. From the fits, we can extract zero-pressure bulk moduli of 28.7 GPa (287 kbar) for RbC_{60} and 27.4 GPa for KC_{60}. These values are greater than the reported bulk moduli of pristine C_{60} (13.4 GPa)[4]

and Rb_3C_{60} (20.5 GPa)[5].

Chapter 4 References

1. M. Nunez-Regueiro, L. Marques, J.-L. Hodeau, *et al.*, Physical Review Letters **74**, 278-281 (1995).

2. C. Kittel, *Introduction to solid state physics* (Wiley, New York, 1996).

3. F.D. Murnaghan, Proc. Natl. Acad. Sci. USA **30**, 244 (1944).

4. H.A. Ludwig, W.H. Fietz, F. W. Hornung, *et al.*, Zeitschrift fur Physik B **96**, 179 (1994).

5. H.A. Ludwig, W.H. Fietz, F. W. Hornung, *et al.*, Physica C **234**, 45 (1994).

Chapter 5.

Introduction to Carbon Nanotubes

5.1 Synthesis of Nanotubes

In 1991, Iijima and coworkers[1], using high-resolution transmission electron microscopy (TEM) made the first observation of carbon nanotubes, tubular structures with diameters on the order of nanometers and lengths which can exeed a micron, in the soot from a carbon arc. Since that discovery, a number of methods have been used to produce nanotubes. The most common method is still the arc vaporization method, as was described in section 1.1 for the synthesis of C_{60} and other fullerenes. In the arc, nanotubes form a dense deposit (called the 'boule') on the cathode. In general, the nanotubes in the boule have of a number of individual concentric layers, and are thus termed multiwalled tubes (MWNT's). It was later discovered that the addition of metal catalysts[2] (such as Fe, Co, Ni, Ga, and Y) to the anode results in the formation of single-walled tubes (SWNT's), which are primarily found not in the boule but in a spongy material outside it. As their name indicates, these materials consist of single tubes, with diameters typically 0.7-1.6 nm. Nanotubes can also be made by laser ablation of a graphite target[3], chemical vapor deposition[4], and a number of other methods. In particular, the Smalley group at Rice has used a double-laser ablation technique[3] and Fe/Co catalysts to produce samples of highly pure (70-90%) single-walled nanotubes which form crystalline bundles, or 'ropes,' of tubes; the bundles form tangled 'mats.' It was later discovered[5] that it is possible to syn-

thesize samples of this type in the carbon arc, using a mixture of Y and Ni as catalysts. The SWNT samples used in the studies described below were synthesized in our lab by Uday Varadarajan using the arc method, and were also obtained from the Smalley group, who used the laser ablation method. MWNT samples were synthesized in our lab using the arc method.

5.2 Morphology of Nanotubes[6]

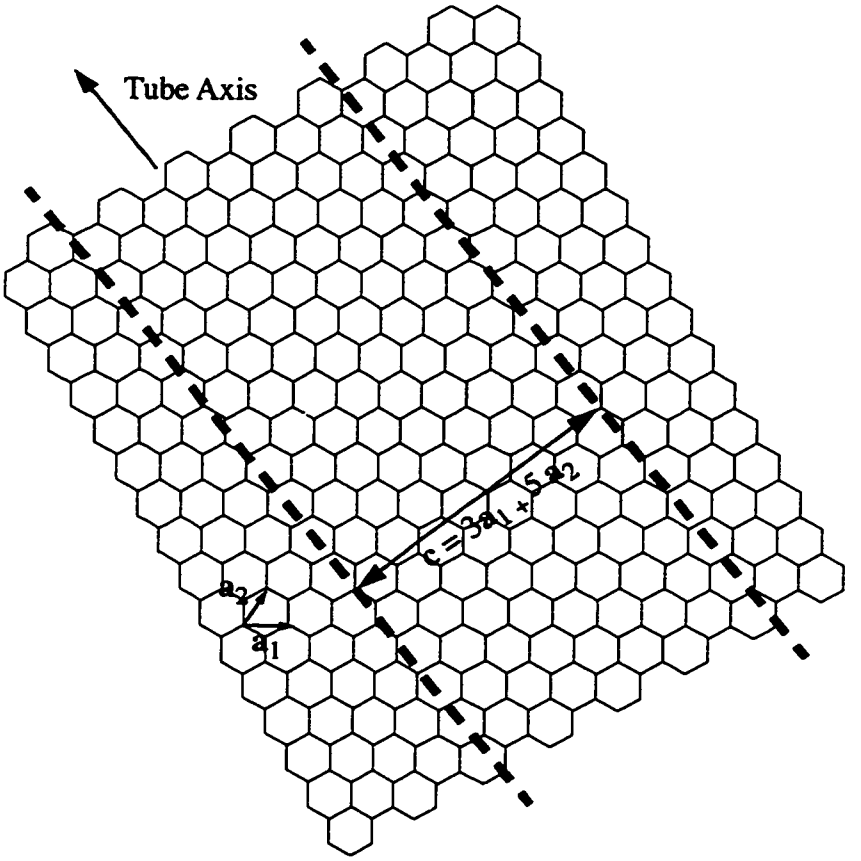

Figure 5.1 Wrapping a Graphene Sheet to Make a Nanotube

A single-walled carbon nanotube consists of a single sheet of graphite (graphene), wrapped into a cylinder. Figure 5.1 depicts the scheme used to describe the geometry of a

nanotube using the wrapping vector. A graphene sheet has two basis vectors ($\mathbf{a}_1$ and $\mathbf{a}_2$), with lengths of 2.4 Å. A tubular geometry can be formed by mapping all points separated by a vector $\mathbf{c} = n\mathbf{a}_1 + m\mathbf{a}_2$ (where n and m are integers) onto each other; the vector c forms the circumference of the tube. Therefore, a single pair of integers (n,m) is sufficient to completely describe the geometry of a nanotube. Alternately, we can say that the geometry of the tube consists of its radius and the chirality with which the sheet is wrapped; the radius is given by

$$R_{tube} = \frac{a}{2\pi}\sqrt{(n^2 + m^2 + nm)}. \qquad (5.1)$$

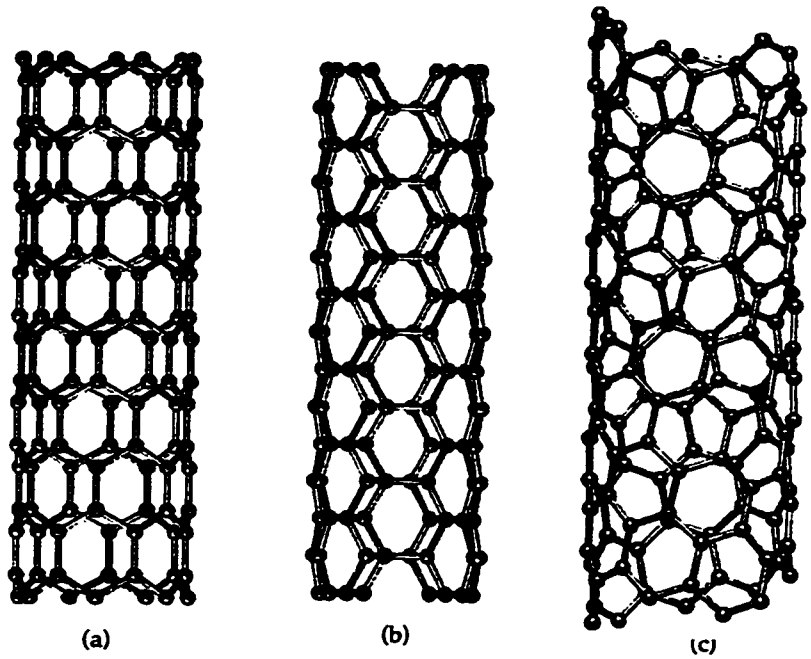

Figure 5.2 Three representative nanotubes. (a) is a 'zigzag' (8,0) tube, (b) is an 'armchair' (4,4) tube, and (c) is a (7,2) tube, of intermediate chirality (Courtesy L. Benedict)

Two geometries are of particularly high symmetry, in that they are achiral: those

described by translation vectors (n,0) and (n,n). The first case results in a tube with a 'zig-zag' chain of carbons along the circumference, while in the second case the chain of atoms in the circumference has an 'armchair' shape. Figure 5.2 depicts a 'zigzag' tube, an 'arm-chair' tube and a tube with arbitrary chirality. We will return to issues of the symmetry in nanotubes below, in the discussion of their electronic structure.

Figure 5.3 Multiwalled Nanotube (Courtesy N. Chopra)

Figure 5.3 is a high-resolution TEM image of a multi-walled nanotube (MWNT). It consists of multiple concentric single-walled tubes, as depicted in the line drawing, which are separated by an inter-layer distance of 3.4 Å, similar to the inter-layer spacing in graphite. Because the strongest scattering occurs when the carbon planes are parallel to the electron beam, the tube appears as two sets of parallel lines, separated by an empty space. Although only a short section of the tube is depicted here, these tubes can be microns in length.

Figure 5.4 shows a high-resolution TEM image of a single-walled nanotube, produced by the graphite arc technique with Ni/Y catalysts. Individual tubes produced by

Figure 5.4 Single-Walled Nanotube (courtesy of N. Chopra)

this method and the laser-vaporization method have been shown to have a diameter distribution sharply peaked near 1.4 nm[3, 7], consistent with the diameter seen in the image.

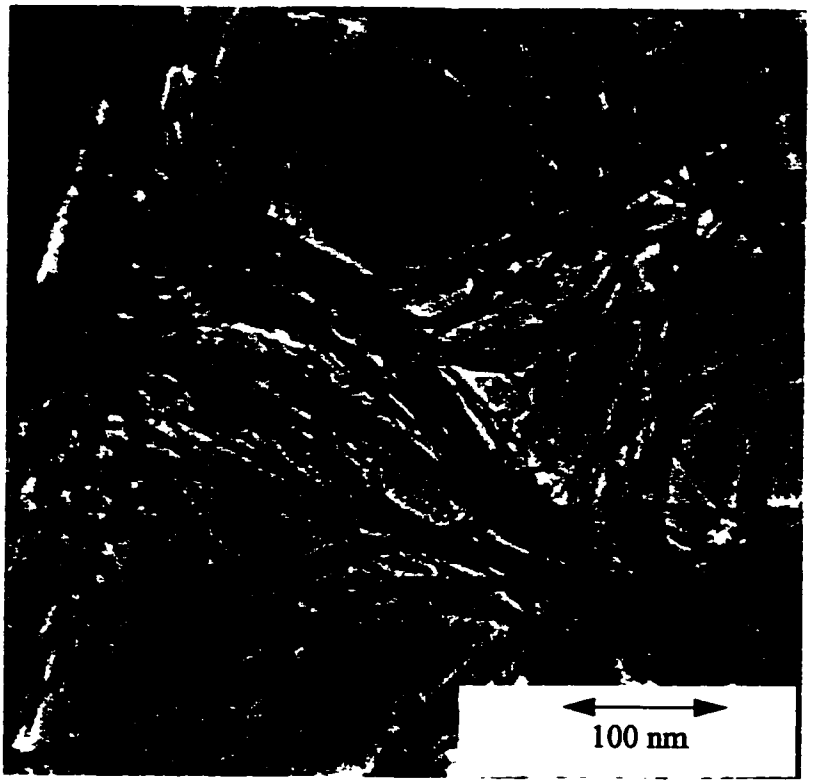

Figure 5.5 SWNT bundles (courtesy of R.E. Smalley)

Figure 5.5 is a TEM image of a sample consisting primarily of bundles of

Figure 5.6 A crystalline bundle of SWNT's, seen in cross-section in the TEM. (Courtesy of R.E. Smalley)

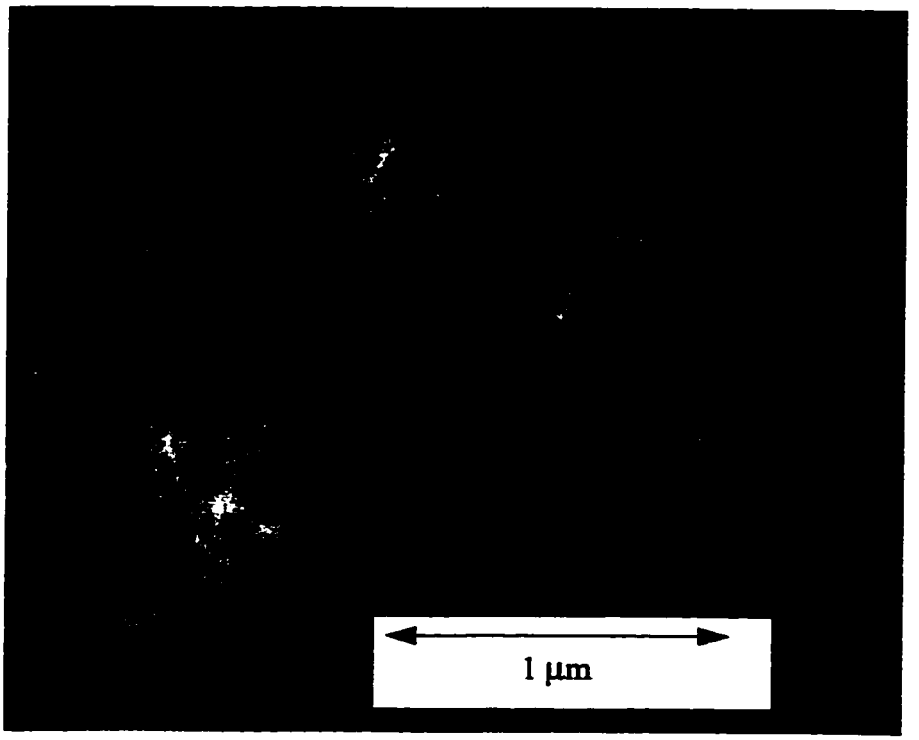

Figure 5.7 SEM image of SWNT ropes (Courtesy of R.E. Smalley)

SWNT's. The tubes in each bundle are arranged in parallel, in a triangular lattice with a nearest-neighbor distance of 1.7 nm. It was originally thought that these bundles contained a majority of the (10,10) variety of tubes[3]; recent studies[8], however, suggest that the chirality distribution is relatively random. Figure 5.6 is a TEM image of the cross-section of a single bundle, showing the triangular lattice. Figure 5.7 shows a scanning electron microscope (SEM) image of an as-grown 'mat' of SWNT ropes: the ropes are microns in length and highly tangled, with the distance between tubes on the order of 100 nm.

5.3 Electronic Structure of Nanotubes

A single graphene sheet has a two-dimensional Brillouin zone with a hexagonal shape. The conduction and valence bands are formed by the π and π^* atomic orbitals, and touch at the corners of the Brillouin Zone. Thus the Fermi surface consists of six points[6]. The rolling up of a graphene sheet into a small-diameter tube greatly affects the dimensionality of its electron (and phonon) structure. Although the shape of the Brillouin Zone of a nanotube is the same as that of the graphene sheet, the rolling-up enforces periodic boundary conditions on reciprocal-space vectors[9]. This has the effect of quantizing the momentum in the direction perpendicular to the tube axis. Thus the allowed wavevectors in reciprocal space are confined to lines slicing the hexagonal Brillouin zone of the graphene sheet. The spacing between these subbands is given by

$$\Delta k_{\perp} = \frac{1}{R_{tube}}. \tag{5.2}$$

Figure 5.8 shows the lines of allowed momentum for three representative nano-

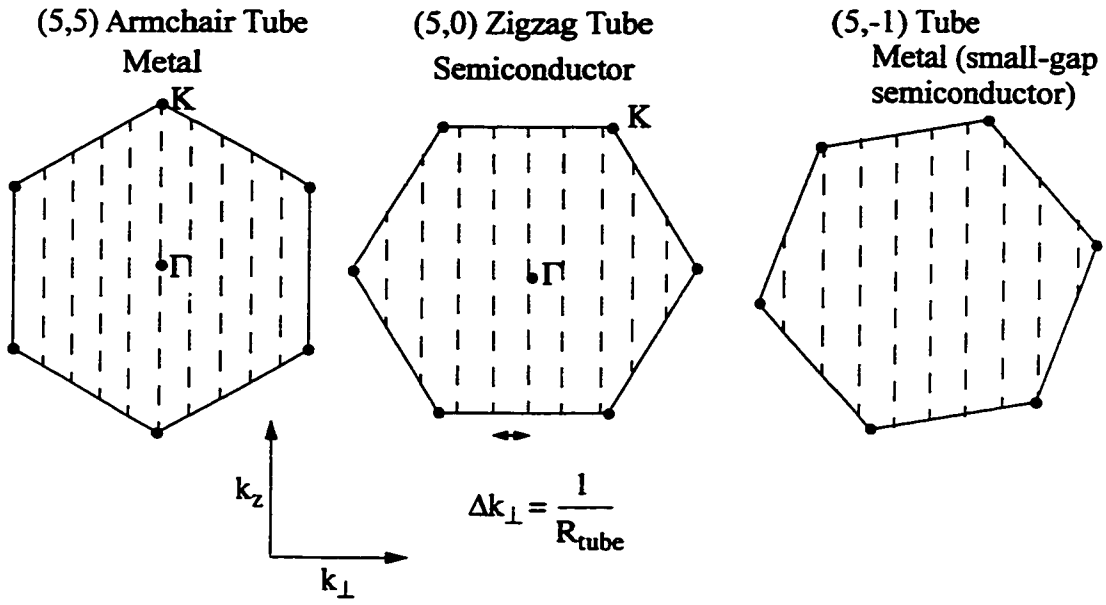

Figure 5.8 Brillouin Zone of Nanotubes of Varying Chirality

tubes. As can be seen from the diagrams, the chirality of a tube influences its electronic structure by determining whether the lines of allowed **k** pass through one of the graphene sheet Fermi points. An (n,n) armchair tube, for instance, is always metallic, because a subband always passes through the center of the Brillouin zone, from the Γ point to the K point. Other tubes, on the other hand, can be metallic or semiconducting depending on whether one of the K points. It can be shown[9] that a chiral tube will be a semiconductor if

$$n - m \neq 3k, \tag{5.3}$$

where k is an integer. A naive approach produces the conclusion that all other tubes (those with n-m = 3k) will be metals, but this is only rigorously true for (n,n) tubes; in the others, band mixing will cause the lines of allowed k to move away from the K points, resulting in a small-gap tube. Thus theory predicts three different classes of tube: metals (with n =

m), small-gap ($\Delta \approx 0.1\,eV$) semiconductors (with n-m=3k), and moderate-gap ($\Delta \approx 1\,eV$) semiconductors ($n - m \neq 3k$). Thus nanotubes represent an all-carbon material with an electronic structure which can be altered by small changes in geometry. Particularly interesting is the possibility of electronic devices created by joining tubes of different chirality at a single defect site[10].

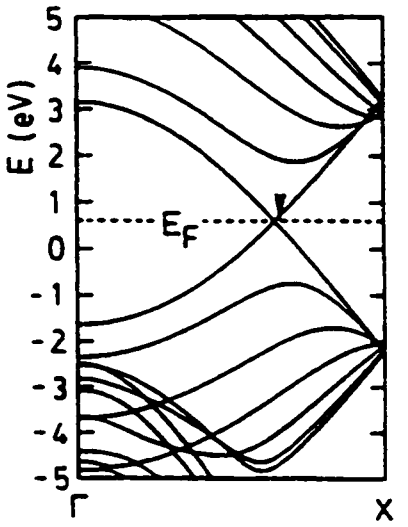

Figure 5.9 Bandstrudture of a metallic (5,5) tube [9]

Figure 5.9 shows the predicted bandstructure of a metallic (5,5) nanotube[9], taken from the Γ point to the K point, along the axis of the tube. At the Fermi level, two bands cross in a nearly linear fashion, with a Fermi velocity of 8×10^7 cm/s. Other bands enter 1.6 eV above and below the Fermi level: these are the first-order circumferential subbands. Since 1.6 eV corresponds to a temperature of ≈ 20,000 K, at ordinary temperatures electrons are confined to a single momentum subband, and the nanotube acts as a one-dimensional electronic system. Because the subband spacing varies as 1/R, a (10,10) tube

will have subbands which enter 0.8 eV above the Fermi level, corresponding to 10,000 K, still well above any reasonable measurement temperatures.

5.4 Transport in Single-Walled Nanotubes

The availability of high-quality samples of SWNT bundles has sparked a great number of experimental studies of this material. Studies of the transport properties of SWNT's fall into two categories: those examining bulk material and those examining single tubes or bundles.

Bulk ('mat') samples display weakly metallic (positive $d\rho/dT$) behavior at room temperature, with a broad transition to nonmetallic (negative $d\rho/dT$) behavior at lower temperatures[11]. The metallic-nonmetallic crossover temperature is typically 150-200 K, although there is a great deal of variation in this behavior: the resistivity is dependent on such factors as mechanical handling of the sample and the applied electric field. At low temperatures (below 5 K), the resistivity of SWNT mat samples seems to exhibit temperature dependence characteristic of variable-range hopping[12]. The conductivity of SWNT mats has been observed to increase upon intercalation with a number of materials, including the alkali metals K, Rb, and Cs, and the halogens Br and I[13]. The intercalants occupy interstitial sites between tubes in SWNT bundles.

It is possible to make electrical contact to single tubes and SWNT bundles using a number of techniques; the simplest is to randomly distribute SWNT's onto a substrate which has been patterned with submicron-scale leads. Devices made in this way have exhibited a broad variety of interesting physics, such as coulomb blockade, resonant tunneling through extended discrete energy levels, and enhancement of the conductivity of

semiconducting SWNT's by application of an external electric field[14, 15].

Chapter 5 References

1. S. Iijima and T. Ichihashi, Nature **363**, 603-15 (1993).

2. D. S. Bethune, C. H. Kiang, M. S. deVries, *et al.*, Nature **363**, 605-7 (1993).

3. A. Thess, R. Lee, P. Nikolaev, *et al.*, Science **273**, 483-7 (1996).

4. M. Terrones, N. Grobert, J. Olivares, *et al.*, Nature **388**, 52-5 (1997).

5. C. Journet, W. K. Maser, P. Bernier, *et al.*, Nature **388**, 756-758 (1997).

6. M. S. Dresselhaus, G. Dresselhaus, and R. Saito, Carbon **33**, 883-91 (1995).

7. A. M. Rao, E. Richter, S. Bandow, *et al.*, Science **275**, 187-91 (1997).

8. T. W. Odom, H. Jin-Lin, P. Kim, *et al.*, Nature **391**, 62-4 (1998).

9. Noriaki Hamada, Shin-ichi Sawada, and Atsushi Oshiyama, Physical Review Letters **68** (1992) 1579-1581

10. L. Chico, V. H. Crespi, L. X. Benedict, *et al.*, Physical Review Letters **76**, 971-4 (1996).

11. J. E. Fischer, H. Dai, A. Thess, *et al.*, Physical Review B (Condensed Matter) **55**, R4921-4 (1997).

12. M. S. Fuhrer, personal communication.

13. R. S. Lee, H. J. Kim, J. E. Fischer, *et al.*, Nature **388**, 255-7 (1997).

14. M. Bockrath, D. H. Cobden, P. L. McEuen, *et al.*, Science **275**, 1922-5 (1997).

15. S. J. Tans, M. H. Devoret, H. Dai, *et al.*, Nature **386**, 474-7 (1997).

Chapter 6.

Thermopower of Single-Walled Carbon Nanotubes

6.1 Introduction to Thermopower

The thermoelectric power (TEP) of a material is defined by the relation

$$E = S\nabla T \tag{6.1}$$

Where E is the electric field and S is the thermoelectric power. Using Boltzmann transport theory, the following expression for the electronic (drift) thermopower can be derived[1]:

$$S(T) = -\frac{1}{eT}\frac{\int \tau_k \mathbf{v}_k \mathbf{v}_k (\varepsilon - \mu)\frac{\partial f_0}{\partial \varepsilon} d^3k}{\int \tau_k \mathbf{v}_k \mathbf{v}_k \frac{\partial f_0}{\partial \varepsilon} d^3k}, \tag{6.2}$$

where τ is the relaxation time, $\mathbf{v}$ is the band velocity, $(\varepsilon-\mu)$ is the energy relative to the chemical potential, and f_0 is the equilibrium electron distribution function; the integral is taken over all momentum states $\mathbf{k}$. Because metals and semiconductors have very different distribution functions, equation 6.2 leads to significantly different expressions for the two cases. In a metal, the derivative of the distribution function is sharply peaked at the Fermi level, and the thermopower becomes:

$$S_{metal}(T) = -\frac{\pi^2}{3}\frac{k_B}{e}k_B T\left.\frac{\partial \ln\sigma}{\partial\varepsilon}\right|_{\varepsilon_F}, \tag{6.3}$$

where the conductivity σ is

$$\sigma = \frac{e^2}{4\pi^3\hbar}\int\frac{\tau_k v_k v_k}{|v_k|}dS \tag{6.4}$$

with the integral taken over the Fermi surface. In the case of semiconductors, the low electron density leads to a slowly-varying distribution function, and therefore the following expression for the thermopower (in 3-d)[2]:

$$S_{semi}(T) = \frac{k_B}{e}\left(\frac{\varsigma}{T} + \frac{\partial \ln\tau}{\partial \ln\varepsilon} + \frac{5}{2}\right), \tag{6.5}$$

where ζ represents the energy distance between the carrier band and the Fermi level, expressed in units of temperature.

In this simple model, the sign of the thermopower is the same the sign of the charge carriers: in a metal, $\frac{\partial}{\partial\varepsilon}\ln\sigma$ is positive for an electron-like band and negative for a hole-like band; in a semiconductor, ζ is positive for holes and negative for electrons. In addition, the temperature dependence of the thermopower can differentiate between a semiconductor and a metal: a semiconductor displays a (1/T)-dependent thermopower, while the thermopower of a simple metal is linear in T. In addition, the thermopower of a semiconductor is usually large at room temperature: $\zeta >> 300$ K for most semiconductors, and so, with k_B/e having a value of 86 μV/K, the thermopower of most semiconductors is in the mV/K range. Metals, on the other hand, usually display a small thermopower (on

the order of a few μV/K), because the factor $\frac{\partial}{\partial\varepsilon}\ln\sigma$ is small. The magnitude and sign of the TEP can, in both cases, be used to test models for the bandstructure of the material.

There are other effects beyond these simple models which complicate the thermopower behavior of real-world materials. Chief among these effects is phonon drag. This occurs because phonons, moving from the hot side to the cold side of the sample, collide with mobile charge carriers (electrons or holes) and cause them to accumulate at the cold end of the sample; this produces a voltage, hence a thermopower. A simple model[3] of this effect assumes that the phonons exert a 'radiation pressure' equal to

$$P_x = \frac{-1}{3}C\frac{dT}{dx}, \tag{6.6}$$

where C is the phonon specific heat; in a steady state, this pressure is then balanced by the a pressure $P = -neE_x$ from the electrons, resulting in a phonon-drag thermopower:

$$S_{e-p} = \frac{C_{phonons}}{3ne}, \tag{6.7}$$

which is again negative for electrons and positive for holes. The phonon drag contribution to the thermopower of most materials leads to a T^3-dependent contribution at low temperature, reflecting the behavior of the phonon specific heat. A slightly more rigorous model takes into account phonon-phonon Umklapp scattering, which also serves to keep the phonon system in equilibrium. In this model, the phonon-drag thermopower is given by

$$S_{e-p} = \frac{C}{3ne}\frac{\tau_{e-p}}{\tau}\ , \tag{6.8}$$

where $1/\tau_{e-p}$ is the electron-phonon scattering rate, and $1/\tau$ is the phonon scattering rate for all processes. This added factor causes the phonon drag thermopower to decrease rapidly (usually like 1/T) in most materials above some fraction (0.1-0.5) of the Debye temperature, as phonon-phonon Umklapp scattering becomes the dominant phonon scattering process. However, as will be discussed in the next chapter, this scattering may be suppressed in SWNT's due to their low dimensionality.

Finally, we note that non-crystalline materials can display a thermopower which is different from that of metals or semiconductors. In systems with variable-range hopping behavior, the thermopower is given by[4]

$$S_h = \frac{k_B^2}{2e}\sqrt{T_0 T}\left[\frac{d\ln N(E)}{dE}\right]\Bigg|_{E = E_F}, \tag{6.9}$$

where N(E) is the density of states at the Fermi level. At high temperatures[5], when the hopping distance is independent of temperature, the thermopower is constant, on the order of

$$S \approx \frac{k_B}{e}\ln\left\{\frac{c}{(1-c)}\right\}, \tag{6.10}$$

where c/(1-c) is the ratio of electrons to holes, and k_B/e has the value 86 μV/K. We note that equation 6.9 gives zero for a system with a constant density of states near the Fermi level, and that equation 6.10 gives zero for systems with electron-hole symmetry.

6.2 Motivation and Experimental Details

We were motivated to study the thermopower of SWNT's for a number of reasons. Previous measurements[6] of the temperature-dependent dc and ac electrical conductivity of macroscopic mats of SWNT's and single SWNT ropes had left open a number of interesting questions. Specifically, what is the nature of the low-temperature upturn in the resistivity of these materials? Is it due to localization, the opening of a gap, or some other mechanism? And is the transport behavior of bulk samples dominated by inter-rope contacts or on-rope or on-tube effects? What is the role in transport of semiconducting vs. metallic tubes? A measurement of the temperature-dependent thermopower of SWNT's could shed light on all of the above questions. In addition, studying the thermopower of samples mechanically treated in different ways allows for the study of the role of inter-tube effects.

Two different types of SWNT samples were used for this study[7]. The first was 'pristine' SWNT mats, prepared by Andrew Rinzler in the Smalley group at Rice University. They were baked out in vacuum at 1000 °C in our laboratory, in order to remove impurities. A second type of sample was made by 'sintering' the SWNT mat samples, in the hope that heating under pressure would improve the contacts between nanotube bundles and render the samples metallic. This was done by pressing the SWNT mat samples between two electrodes under vacuum, and then applying a large current to heat the material. The outcome was a dense material which could be cut into the desired shape. Figure 6.1 shows the resistivity, normalized at room temperature, of both samples. It is difficult to compare the absolute resistivities of the samples, but rough measurements suggest that the resistivity of the sintered sample is actually larger than that of the pristine sample by a

factor of about 10. In addition, we can see that the sintered sample displays nonmetallic resistivity over the entire temperature range, while the pristine sample is metallic from 300 K to 180 K.

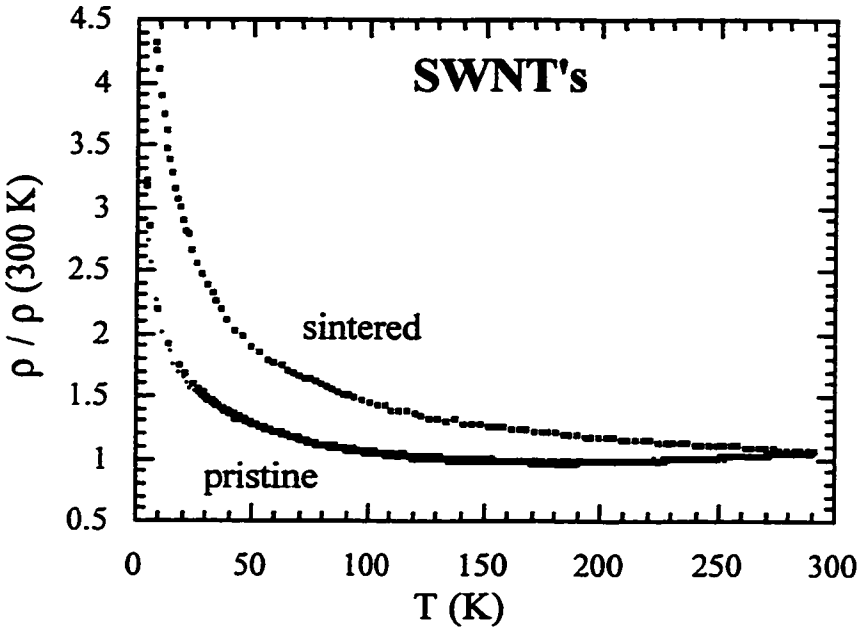

Figure 6.1 Temperature-Dependent Resistivity of SWNT Samples

Thermopower was measured using the methods outlined in Appendix A, except that most of the measurements were taken at a number of fixed target temperatures, rather than on temperature sweeps. 'Mat' samples were obtained by pulling small pieces (approx. 5mm X 0.5 mm X 0.5 mm) out of a larger SWNT mat, while the 'sintered' samples were obtained by slicing off small pieces from the sintered sample. Because the samples were mechanically robust, they could be mounted directly onto the thermopower stage with silver paint.

Figure 6.2 shows the thermopower of three samples, two pristine and one sintered, as a function of temperature from 300 K to 4.2 K. All samples show similar behavior; at

high temperatures the TEP is positive and of moderate magnitude (of order 50 μV/K), while at low temperatures the TEP is linear in temperature and approaches zero as T→0. There is a notable change in the temperature dependence of the TEP near 100 K. Because the magnitude and functional form of the TEP is insensitive to sample preparation (i.e. sintering), the measured TEP, unlike the measured resistivity, is likely to reflect the intrinsic properties of the nanotube bundles.

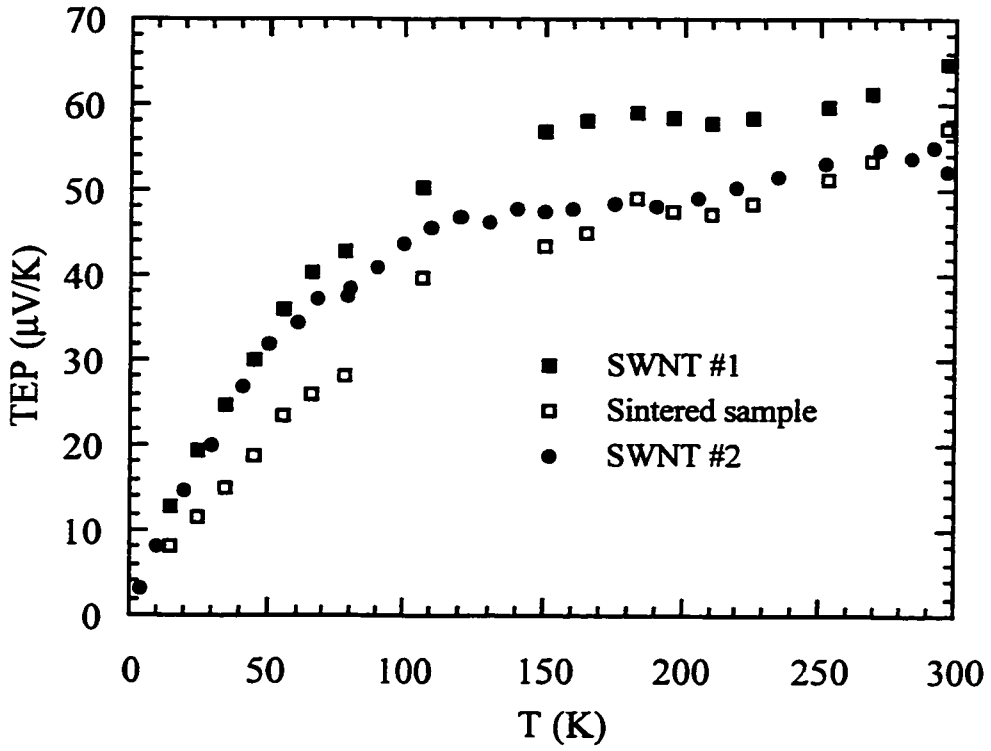

Figure 6.2 Measured thermopower of SWNT's[7]

As was noted above, the TEP of a material can be used to elucidate its electronic structure. A simple interpretation of the rather large (for a metallic system) positive high-temperature TEP indicates hole-like carriers. This result is surprising in that metallic

tubes (such as (10,10) tubes) are predicted to have electron-hole symmetry and thus a TEP close to zero. It is also noteworthy that the magnitude of the measured TEP is considerably larger than that of graphite, simple metals, or MWNT's. The vanishing of the TEP at low temperatures argues against the opening of a semiconducting gap at the Fermi level, which might be invoked to account for the observed increase in electrical resistivity at low temperature. The temperature dependence of the TEP is also unusual: it does not correspond to that of a simple metal or semiconductor, nor does it display a power-law dependence as might be expected for hopping-type conductivity (equation 6.9), although this behavior might only manifest itself at low temperatures (below 4 K).

6.3 Expected Thermopower of a (10,10) Tube

We expect the transport in SWNT bundles to be dominated by metallic tubes; we take the (10,10) tube as a representative of the metallic tubes in the sample. Therefore, we first compare the measured TEP to that of an individual metallic (10,10) tube. As was discussed above, two pairs of one-dimensional bands cross at the Fermi level of a metallic tube, forming a conduction band and a valence band, with a Fermi surface consisting of two points. The bands are highly linear near the Fermi level, and thus display electron-hole symmetry.

To calculate the expected thermopower of a (10,10) tube, we first examine the Mott expression (equation 6.3) for the thermopower of a metal. In 1-D, the conductivity (equation 6.4) is given by:

$$\sigma_{1D} = \frac{2e^2}{h}\sum v\tau, \tag{6.11}$$

where the sum is over all states at the Fermi points. Equation 6.3 therefore reduces to:

$$S_{1-D} = -\frac{\pi^2 k_B^2 T}{3e}\left\{\frac{v'}{v} + \frac{\tau'}{\tau}\right\}, \tag{6.12}$$

where their derivatives are with respect to energy, and the expression is evaluated at the Fermi points. The first term in the brackets is strictly zero for linear bands. Due to the near-linear bandstructure and high band velocity ($v_F = 8 \times 10^7$cm/s) of metallic tubes near the Fermi level, we estimate an upper limit of 0.5 μV/K for the room-temperature contribution from the first term in equation 6.12. The energy-dependent relaxation time, τ(E), should be determined at moderate temperatures by electron-phonon scattering. Assuming that phonon energies can be neglected, Fermi's Golden Rule gives

$$\frac{1}{\tau_{e-p}} = \frac{2\pi}{\hbar}\left|V(E)\right|^2 N(E), \tag{6.13}$$

where V(E) is an electron-phonon scattering matrix element and N(E) is the electron density of states. In 1-D, with linear bands, N(E) is constant. V(E) should vary slowly near the Fermi level, and thus τ(E) will be nearly constant over this energy range as well, yielding a negligible contribution from the second term in equation 6.12. Hence, the total drift contribution to the TEP of individual (10,10) tubes is insufficient to account for the observed TEP.

We now address the issue of phonon-drag thermopower. Offhand, we do not expect phonon drag effects to be appreciable at high temperatures. In graphite, for

instance, the maximum phonon drag contribution to the TEP occurs at 15 K[8]. In addition, the electron-hole symmetry of SWNT's should produce a phonon-drag thermopower which is identically zero. If the number of electrons and holes is equal (as it should be for linear bands), then the contribution from equation 6.8 for each carrier type should be equal in magnitude, and the total phonon-drag TEP should be zero. A more rigorous expression for the phonon-drag thermopower is[1]

$$S_{e-p} = \frac{e}{\Omega \sigma k_B T^2} \sum_q \sum_{k,k'} \Gamma_{k'k} (v\tau - v'\tau') v_{ph}(\mathbf{q}) \hbar \omega_q \tau_{p-p}(\mathbf{q}) \quad , \tag{6.14}$$

Where $\Gamma_{k'k}$ is the rate of electron-phonon scattering from an electron state k to a state k', and the sum is over all phonon wavevectors q, where $k' - k = q$. The linearity of the bands near the Fermi level ensures that all of the terms $(v\tau - v'\tau')$ will either be identically zero (for scattering on the same band) or cancel with a matching term (for scattering between bands). Therefore phonon drag is unable to account for the thermopower of a metallic nanotube with linear bands.

Finally, we examine the expressions for disordered conductors (equations 6.9 and 6.10). A (10,10) tube will have a constant density of states at the Fermi level, and thus should have a zero thermopower according to equation 6.9. Likewise, the electron-hole symmetry should produce a zero value from equation 6.10.

Having considered both the electronic (drift) and electron-phonon (phonon drag) contributions, as well as expressions describing disordered systems, we conclude that a single metallic nanotube with electron-hole symmetry should have an identically zero thermopower. While the small deviations from linearity in the bandstructure of a nano-

tube might result in finite contributions from any of these mechanisms, it is unlikely that these can account for the relatively large magnitude of the observed TEP.

There are a number of processes by which the electron-hole symmetry of metallic nanotubes could be broken, thereby yielding substantial TEP contributions. One possibility is that the assembly of individual (10,10) tubes into a rope is sufficient to break the single-tube electron-hole symmetry. Recent theoretical work[9] has predicted that tube-tube interaction in a rope of (10,10) tubes causes the opening of a 'pseudo-gap' in the density of states of the rope at the Fermi level and shifts the Fermi level downward. In addition, assembling 1-D tubes into 3-D ropes might break the electron-hole symmetry by causing an energy-dependence of the density of states and the area of the Fermi surface. Symmetry-breaking by either interaction mechanism could cause a contribution to the thermopower from both drift and phonon-drag effects, although the magnitude of the effect has not been calculated.

6.4 Thermopower of Metallic and Semiconducting Tubes in Parallel

Because the SWNT bundles likely comprise both semiconducting and metallic tubes, we now consider that semiconducting tubes, acting in parallel with metallic tubes, could account for the observed TEP. To explore this possibility, we model SWNT ropes as comprising semiconducting and metallic tubes in parallel. In a simple two-band model, the total TEP is given by[3]

$$S_{total} = \frac{G_{metal} S_{metal}}{G_{total}} + \frac{G_{semi} S_{semi}}{G_{semi}} \tag{6.15}$$

where G is the electrical conductance of each channel. To develop a functional form for the total TEP, we first insert generic forms for the metallic and semiconducting TEP and conductivity. A simple metal will have a linear TEP, while a semiconductor will have a constant term and a term proportional to λ / T, where λ is the gap temperature. We assume an activated form for the semiconducting conductance, $G_{semi} \propto \frac{-\lambda}{T}$, and that the total conductance is dominated by the metallic channel. The conductivity of an ideal metallic nanotube is difficult to model in a compact way. A (1/T) dependence is probably best near room temperature, but fails to take into account the low-temperature residual resistivity. Likewise, a temperature-independent conductivity is probably better at low temperature and less accurate at high temperature. We consider both extreme cases below. If a (1/T) dependence for the metallic conductivity is assumed, we obtain

$$S_{tot} = AT + (B\lambda + CT)\exp\left(\frac{-\lambda}{T}\right), \tag{6.16}$$

while a constant metallic conductivity yields

$$S_{tot} = AT + \left(\frac{B\lambda}{T} + C\right)\exp\left(\frac{-\lambda}{T}\right) \tag{6.17}$$

In both cases the first term in the sum is the thermopower of the metallic channel and the second is the conductance-weighted thermopower of the semiconducting channel.

In attempting to fit the observed TEP using the above model, we will first use the

predicted (near-zero) TEP of an isolated (10,10) tube (equation 6.12) to provide the A parameter, and then attempt to fit the data by adjusting the values of B, C, and λ. Next, we will consider the TEP of a broken-symmetry metallic tube in parallel with a semiconducting tube by allowing the A parameter to vary.

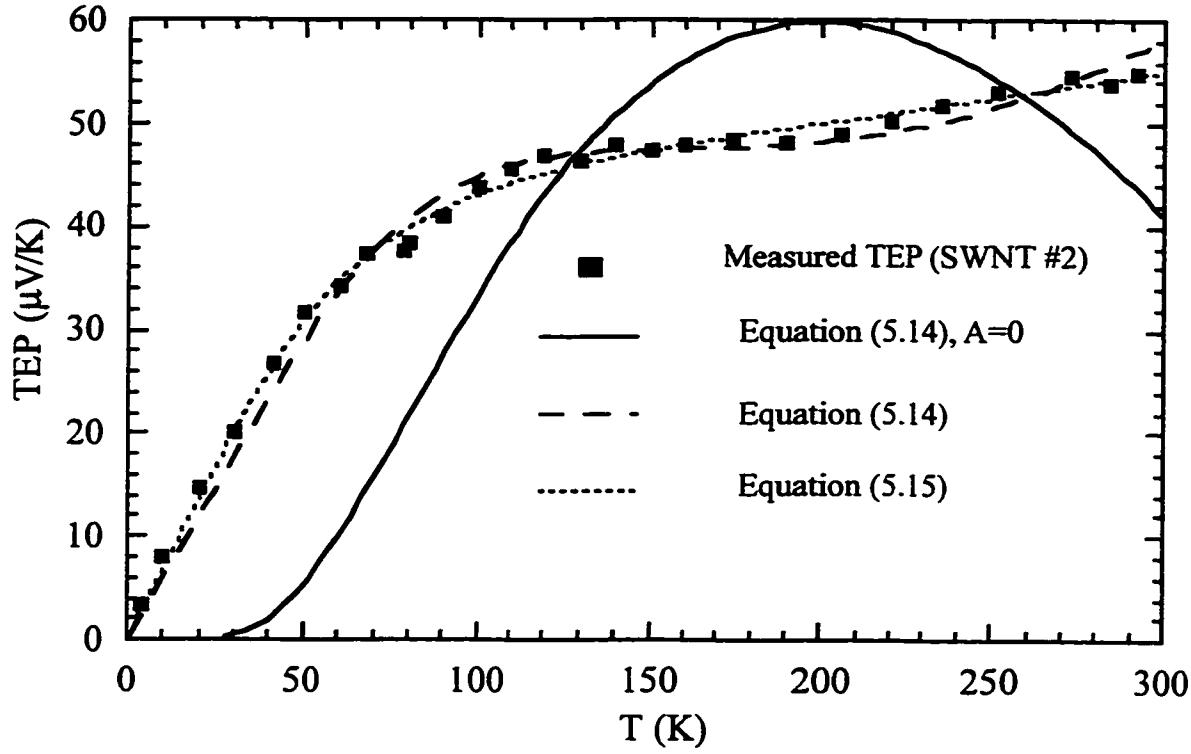

Figure 6.3 Fits to the measured TEP using a two-band model to simulate semiconducting and metallic tubes in parallel. The solid curve represents a fit to the data using equation 6.16, with A=0 to represent the TEP of an isolated metallic nanotube. The two dashed lines represent fits to the data using equation 6.16 and equation 6.17; in these cases, A is allowed to vary in order to simulate a metallic nanotube with broken electron-hole symmetry. The fitting parameters extracted from the fit to equation 6.16 are $A = 0.7\mu V/K^2$; $B = -0.46\mu V/K^2$; $C = -0.65\mu V/K^2$; and $\lambda = 179K$. The fitting parameters extracted to the fit to Eq. (6.17) are $A = 0.59\mu V/K^2$; $B = -0.1\mu V/K$; $C = -343\mu V/K$; and $\lambda = 302$ K.

The lines in figure 6.3 represent fits of Eqs. (6.16) and (6.17) to one of the data sets

(SWNT #2) shown in Fig. 6.2. The solid line represents the first attempt to fit the data, using the TEP of an isolated metallic tube in parallel with a semiconducting tube with a gap temperature of 200 K. This model fails to fit the data for any reasonable choice of λ. This failure can be understood by examining equation 6.15. The low-temperature thermopower of a metal and a semiconductor in parallel will always be dominated by the metal, because the conductance of the semiconductor decreases exponentially, overwhelming its increasing thermopower. Therefore we conclude that the introduction of semiconducting tubes into a rope, without any interaction between tubes to break the symmetry of the metallic tubes, cannot explain the measured thermopower. This leads us to expand the model to consider a metallic tube with broken electron-hole symmetry in parallel with a semiconducting tube.

The dashed lines in fig. 6.3 represent fits of eqs. (6.16) and (6.17) to the same data set, where now the metallic thermopower and the gap temperature are left as fitting parameters. Both forms fit the measured data quite well; the exact form of the metallic conductivity is not critically important, and in both cases the total conductivity is dominated by that of the metallic tube, in agreement with the observed metallic conductivity in this system. The fitting parameters obtained in both cases are given in the caption to figure 6.3. The temperature coefficient of the metallic thermopower is given by the A parameter; its value implies a positive TEP, with a room-temperature magnitude near 200 μV/K in both cases. λ is of order 200-300 K, indicating that small-gap semiconductors are necessary to produce the observed TEP. Significantly, the B and C parameters are negative in both cases, indicating that the semiconducting contribution is electron-like. The success of this model in fitting the measured data suggests a physical mechanism for symmetry-breaking

in nanotube ropes, in which a transfer of electrons from metallic to semiconducting tubes, results in hole-like metallic tubes and electron-like semiconducting tubes. The contributions from both species acting in parallel could reproduce the measured thermopower.

To summarize, we are able to draw a number of definite conclusions from the magnitude and sign of the measured thermopower and the theoretical analysis. First, the observed thermopower cannot be derived from the bandstructure of an individual metallic (n,n) tube. Second, the addition of semiconducting tubes in parallel with zero-thermopower metallic tubes is still insufficient to account for the low-temperature behavior of the thermopower--there must be at least some metallic tubes which have broken electron-hole symmetry and thus a nonzero thermopower. These tubes could be either (10,10) tubes with symmetry broken by tube-tube interactions, 'small-gap' semiconducting tubes which are metallic (either through some sort of doping process or due to intrinsic effects) or by another mechanism entirely.

6.5 Thermopower of SWNT's at High Temperature

In an effort to extend the range of the TEP measurements taken previously, and in preparation for vapor-transport doping of nanotube mats, we studied the thermopower of SWNT' s at high temperature. This was done by building a small TEP stage inside of a 'doping vessel' (similar to that described in chapter 8) which could be sealed with a VCR-type fitting and operated under dynamic vacuum or sealed under vacuum for measurement at low temperatures. The system could be heated with heater tape or cooled in to 4.2 K in a liquid-helium cryostat. Data were taken using the automated system described in appendix A.

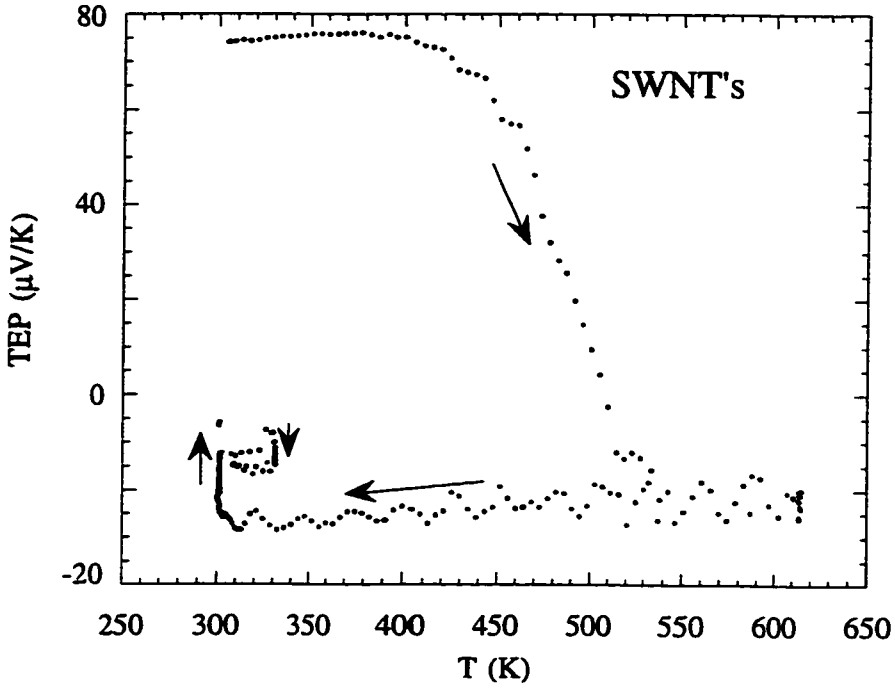

Figure 6.4 High-temperature behavior of the thermopower of SWNT's.

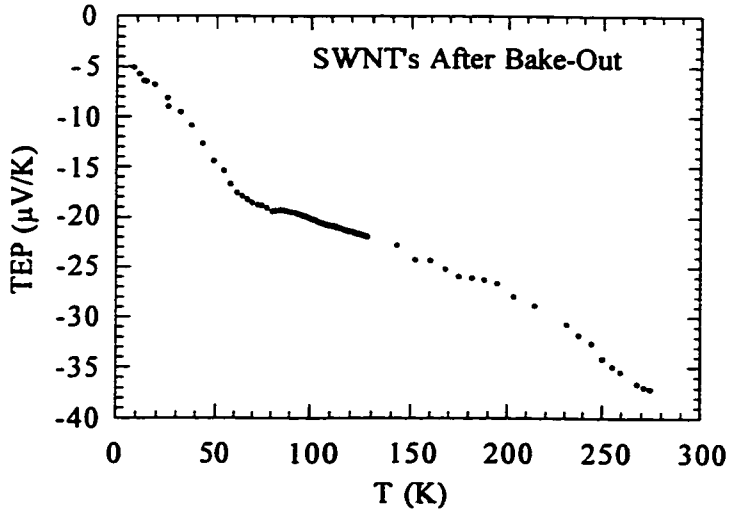

Figure 6.5 Thermopower of SWNT's after high-temperature treatment

Figure 6.4 shows the results obtained upon heating a SWNT sample from 300 K to 620 K, and then cooling to room temperature. The room-temperature thermopower is consistent with previous measurements, and is roughly constant to about 400 K. Above this temperature, the thermopower rapidly decreases, crosses zero, and reaches a value of $\approx$ -15 μV/K. This change in sign of the TEP is a kinetic process: the TEP changes with time at constant temperature, and changes faster at higher temperatures. Furthermore, it is not easily reversible. If the sample is cooled relatively quickly, the TEP remains negative to 4.2 K, as is shown in figure 6.5 (the data in this plot were obtained using a different sample, which displayed a different thermopower after high-temperature treatment). However, when the sample is allowed to sit at room temperature, the thermopower begins to increase and eventually turns positive over a period of days. This process appears to be reversible: when the sample is heated to even a few degrees above room temperature, the thermopower begins to slowly decrease, forming the hysteresis loop shown in figure 6.4. The change in the sign of the TEP at high temperature has been observed in a number of samples, both under dynamic vacuum and sealed in vacuum.

Because of the long timescale involved in the hysteresis in the TEP, we have not yet performed a complete study of this phenomenon. Nevertheless, it is possible to speculate on some mechanisms which could account for the observed behavior. First, there could be some type of external dopant, such as oxygen, in the nanotube ropes. This dopant could change the thermopower of the nanotubes in the sample (particularly the small-gap semiconductors, whose TEP should be highly sensitive to the thermopower). Heating under vacuum could drive off the dopant and change the TEP. The return of the TEP to its original positive behavior when left at room temperature could be due to a small

leak of the dopant back into the system. However, it seems unlikely that this type of mechanism could account for the hysteresis loop obtained by heating the sample only a few degrees above room temperature.

An alternate explanation for the hysteretic behavior of the thermopower is that the SWNT ropes undergo some type of structural phase transition which affects their electronic structure. For instance, if there is any type of orientational ordering of the tubes with respect to each other, this orientational ordering could change with heating; because of the length of the tubes, relaxation to the low-temperature state could take considerable time.

6.6 Thermopower of Br-Intercalated and Acid-Treated SWNT's

Because the conductivity of SWNT's changes drastically upon doping with both electron donors and acceptors, it is interesting to examine the effects of doping upon the thermopower of these materials. However, because alkali-metal doping requires high temperatures (with the associated strange behavior of the TEP), we decided to concentrate on SWNT's doped with bromine. Bromine intercalation occurs at room temperature, and Br-doped tubes are air-stable. Therefore, we synthesized samples by enclosing a SWNT mat in a beaker with a few drops of bromine liquid, which quickly vaporized and intercalated the tubes. Small strands of the doped SWNT's were then mounted on the TEP stage and measured in the same manner as the pristine materials.

Figure 6.6 shows the resistance of a Br-intercalated SWNT sample as a function of temperature (the feature near 80 K is due to a change in the cooling rate); it displays the same behavior as as-grown SWNT's, with metallic behavior at high temperature and a

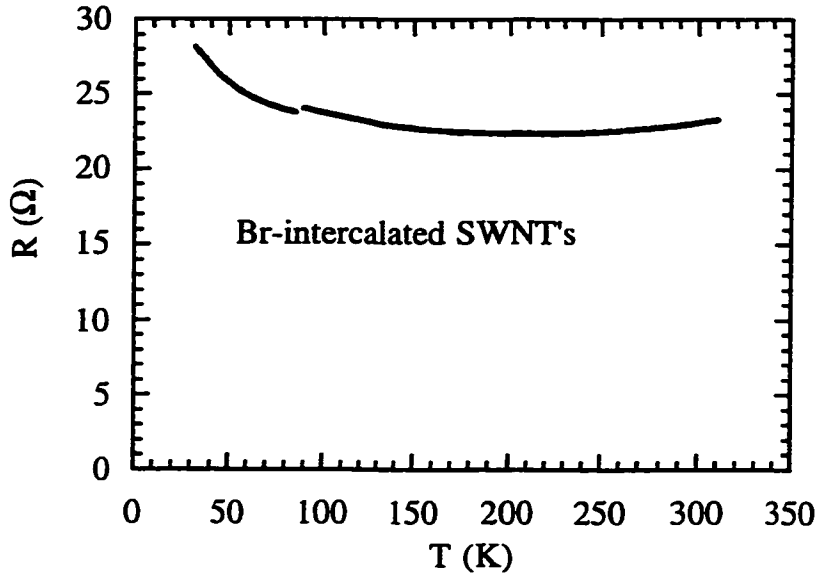

Figure 6.6 Resistance vs. temperature of a Br-intercalated SWNT sample

crossover to nonmetallic behavior near 200 K. Although the magnitude of the resistivity decreases with intercalation, the temperature-dependence of the resistivity does not seem to. Figure 6.7 shows the TEP of Br-doped tubes as a function of temperature from 300 K to 4.2 K. The thermopower of the doped tubes is positive, as would be expected for a hole-doped system, and smaller in magnitude than the TEP of pristine tubes. If the large positive TEP of the pristine tubes is due to tubes which are already doped to near a hole band edge, then it is possible that Br-doping could be moving the Fermi level further down, to a region of the band with smaller curvature, resulting in a lower TEP. At low temperature, the TEP shows a 'bump' which may be due to phonon drag. It is interesting to examine the temperature dependence of the TEP of the Br-doped SWNT's. It displays neither a linear nor a power-law temperature dependence (although above 150 K it varies roughly as $T^{1/2}$). It seems to be logarithmic in T above 40 K, as can be seen in figure 6.8;

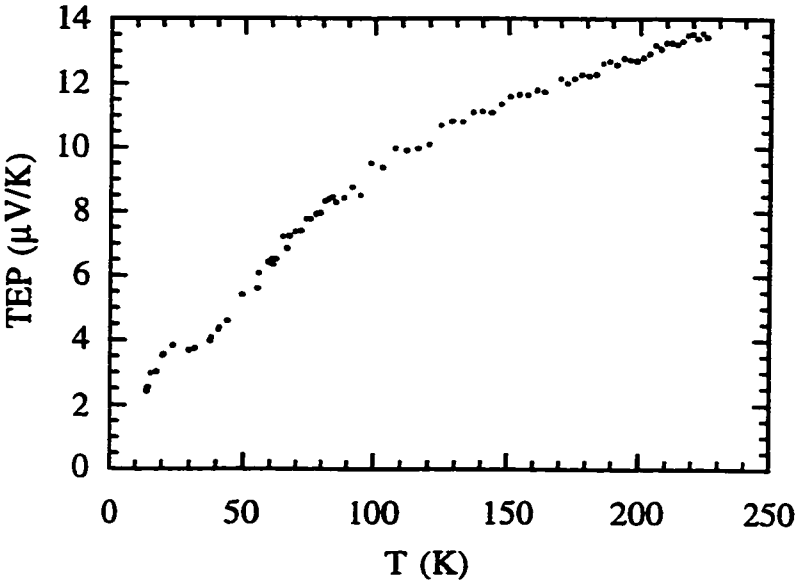

Figure 6.7 Thermopower of Br-intercalated SWNT's

the feature at lower temperatures may be due to phonon drag.

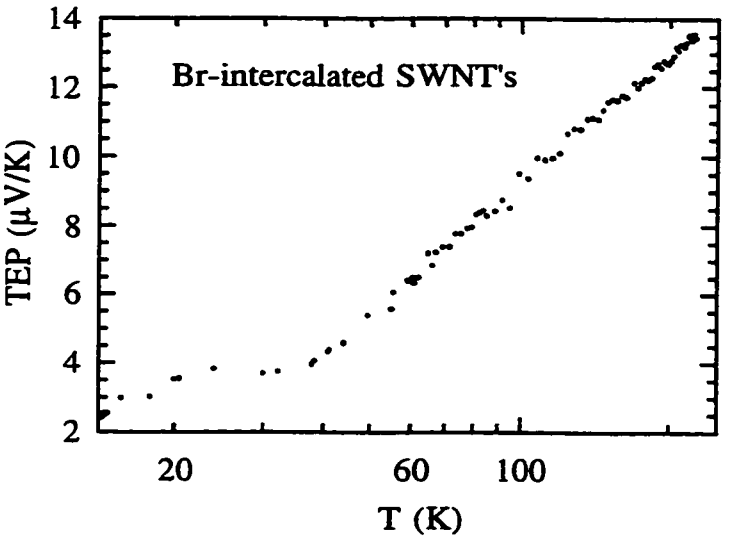

Figure 6.8 Thermopower of Br-intercalated SWNT's vs. log T

One difficulty with SWNT's has been their purification: although highly pure

samples are possible, many samples are of lower purity. Thus considerable effort has been involved in attempting to remove the amorphous carbon, nanoparticles, and metal particles from the tube mats. Several schemes have been developed, including filtration and chromatographic separation. A particularly successful scheme involves treatment of the tubes in dilute nitric acid. The nitric acid preferentially attacks strained sites, such as pentagons, in graphitic lattices. Thus amorphous carbon and nanoparticles are quickly eaten away, while tubes are not; the tubes can then be separated from the other material by a filtration method which yields flat pieces of 'bucky-paper.' Even though the tubes are rinsed with distilled water numerous times after the treatment, it is still possible that nitric acid remains as an intercalant inside the tube lattice and affects the electronic structure; such a doping should show up in the thermopower. Figure 6.9 shows the thermopower of a piece of SWNT 'bucky-paper' made in our lab by Uday Varadarajan. The thermopower is closer to that of the Br-doped tubes than that of the pristine material, raising the possibility that left-over nitric acid is doping the SWNT's. The data can be fit well by the functional form

$$S(T) = AT^{0.72}, \tag{6.18}$$

as indicated by the solid line in the plot. The deviation from this form at low temperature may be due to a phonon drag effect.

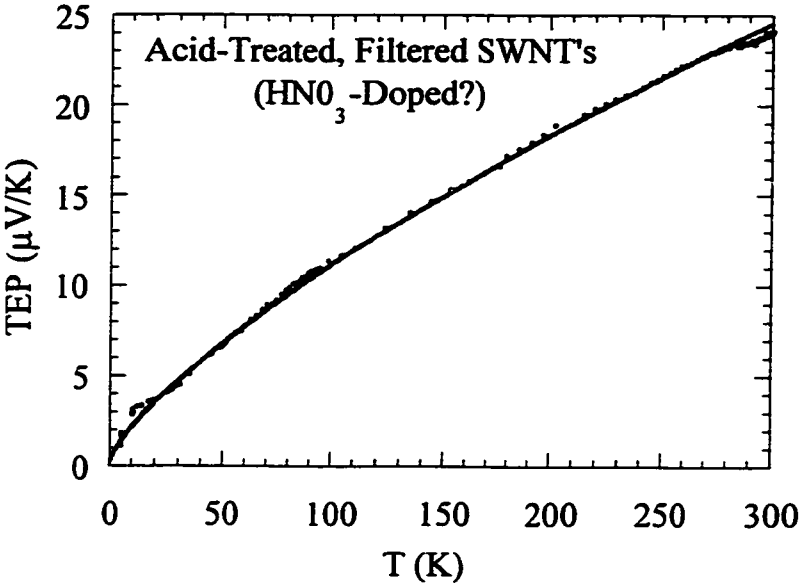

Figure 6.9 TEP of acid-treated and filtered tubes

Chapter 6 References

1. F. J. Blatt, *Thermoelectric power of metals* (Plenum Press, New York, 1976).

2. F. J. Blatt, *Physics of Electronic Conduction in Solids* (McGraw Hill, New York, 1968).

3. D. K. MacDonald, *Thermoelectricity, an Introduction to the Principles* (Wiley, New York, 1962).

4. I. P. Zvyagin, in *Hopping Transport in Solids*, edited by M. Pollak and B. Shklovskii (North-Holland, New York, 1991), Vol. 28.

5. N. F. Mott and E. A. Davis, *Electronic processes in non-crystalline materials* (Oxford University Press, Oxford, 1979).

6. J. E. Fischer, H. Dai, A. Thess, *et al.*, Physical Review B (Condensed Matter) **55**, R4921-4 (1997).

7. J. Hone, I. Ellwood, M. Muno, *et al.*, Physical Review Letters **80**, 1042-5 (1998).

8. B. T. Kelly, *Physics of graphite* (Applied Science, London; Englewood, N.J., 1981).

9. P. Delaney, C. Hyoung Joon, Jisoon Ihm, *et al.*, Nature **391**, 466-8 (1998).

Chapter 7.

Thermal Conductivity of Carbon Nanotubes

7.1 Motivation and Experimental Procedure

Carbon-based materials (diamond and graphite) display the highest thermal conductivity (κ) of any known substance at moderate temperatures[1], due primarily to the high velocity of acoustic phonons in these materials. Carbon nanotubes have also been predicted[2] to have a high thermal conductivity, but until this study that speculation had not been confirmed. In addition, it was unknown whether electrons or phonons provided the mechanism for thermal transport in nanotubes. Finally, the low-temperature phonon thermal conductivity of a material is sensitive to the dimensionality of the material. Thus a study of the thermal conductivity of nanotubes could ideally measure the magnitude of their thermal conductivity, determine the predominant mechanism for thermal conduction, and probe issues of dimensionality in these materials.

A number of different carbon nanotube samples were studied. Single-walled carbon nanotubes (SWNT's), synthesized in the Zettl lab by Uday Varadarajan using the graphite arc technique and at Rice University using the laser ablation technique, were studied in their as-grown configuration, as tangled 'mats' of SWNT bundles. In addition, the 'sintered' SWNT material, as described in the previous chapter, was studied in order to assess the role of changing contacts and mechanical damage on the sample. Finally, a multiwalled nanotube (MWNT) sample, consisting of a section of a 'boule' grown in the

graphite arc, was studied. Thermal conductivity was measured using the comparative method, as described in Appendix A. We will first discuss the thermal conductivity of SWNT's and then discuss MWNT's.

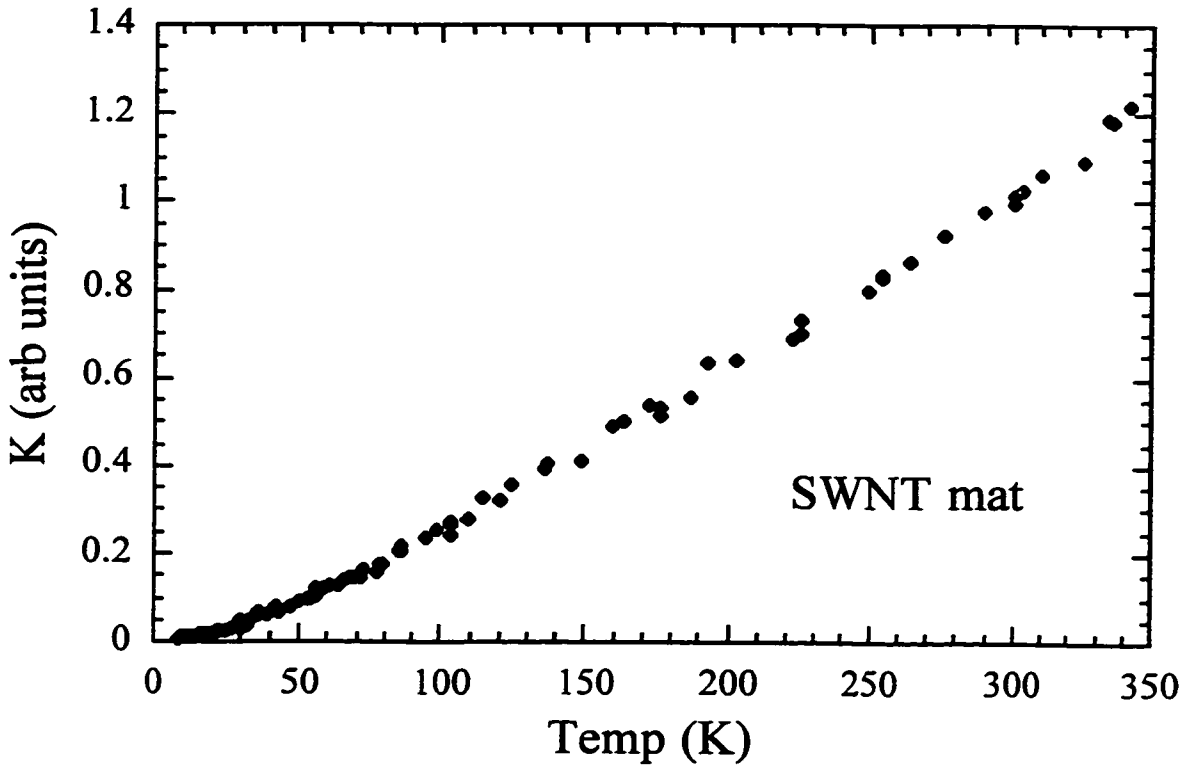

Figure 7.1 Thermal conductivity of a SWNT mat sample

7.2 Measured Thermal Conductivity of SWNT's

Figure 7.1 shows the measured thermal conductivity of a SWNT mat sample as a function of temperature. The data have been normalized to their room-temperature value; we will address the issue of the magnitude of the measured thermal conductivity in section 7.3 below. This behavior was duplicated in a number of mat samples, as well as in the sintered sample. Because the behavior is independent of geometry and mechanical treatment

of the sample, we believe that it reflects the intrinsic behavior of the SWNT's in the sample rather than extrinsic effects such as the connections between ropes or geometry of the sample. $\kappa(T)$ decreases from 350 K to 8 K with very little curvature, in contrast to the behavior of diamond and graphite, which show T^3-like and T^2-like power law dependence below 150 K[1].

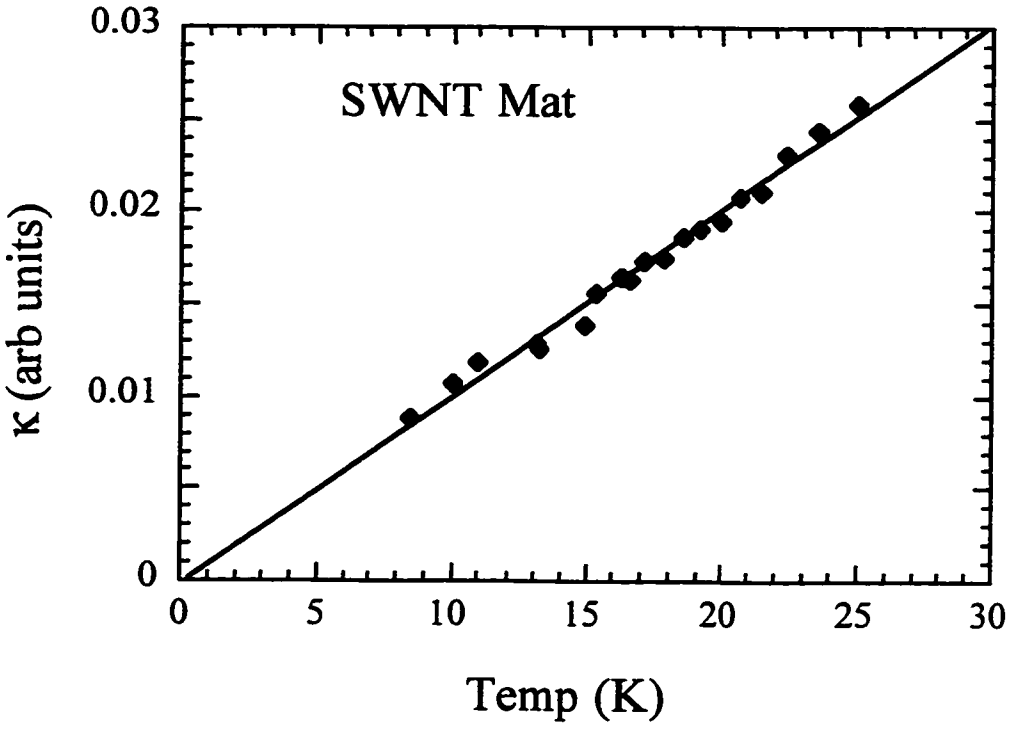

Figure 7.2 Low-temperature thermal conductivity of SWNT's

Figure 7.2 highlights the low-temperature thermal conductivity of SWNT's, with the solid line representing a linear fit to the measured data. Below 30 K, κ displays a strictly linear temperature dependence, and extrapolates to zero as $T \rightarrow 0$. A linear temperature dependence at low temperature is usually attributed to electrons; we will examine

this issue below.

7.3 Magnitude of κ(T) of SWNT's

We first attempt to determine the magnitude of the thermal conductivity of SWNT's from the measured data. As a first step, we obtain the bulk thermal conductivity of the mat sample from the measured thermal conductance and the measured dimensions of the sample. Doing this, we find that a typical sample has a thermal conductivity of ≈ 0.7 W/m-K at room temperature. However, a typical mat sample is mostly empty space; we must correct this value for the filling fraction of a mat, which we measured to be about 2% by finding the ratio of the mat's density to the expected density of a close-packed rope of tubes with a 1.4-nm diameter. Thus we determine the true value of the room-temperature bulk thermal conductivity of nanotubes in a mat, κ_{mat}, to be 36 W/m-K.

The bulk thermal conductivity of tubes in a mat does not take into account the tangled nature of tubes in a mat; the longitudinal thermal conductivity κ_{rope} is likely larger than κ_{mat}. The exact determination of the ratio between these two quantities has not been determined experimentally nor addressed theoretically. Therefore we look to previous electrical transport experiments for inspiration. The longitudinal electrical conductivity of a single rope has been measured[3] to be 50-150 times that of a bulk mat sample. If we assume that the same holds true for thermal conductivity, i.e. that

$$\frac{\kappa_{rope}}{\kappa_{mat}} \approx \frac{\sigma_{rope}}{\sigma_{mat}}, \tag{7.1}$$

then we arrive at a value of 1800-6000 W/m-K for the room-temperature longitudinal

thermal conductivity of a rope of nanotubes. This value is comparable to that of diamond or graphite at similar temperatures. Finally, we note that the sintered sample has a thermal conductivity which is less than one tenth that of the mat sample.

7.4 Electrons or Phonons?

We now address the question of whether the observed thermal conductivity is due to electrons or phonons. The low-temperature linear behavior points toward an electronic mechanism; yet the thermal conductivity of similar materials (diamond, graphite, and carbon fibers) is phonon-dominated. To conclusively resolve the separate electronic and lattice contributions to the thermal conductivity, we measure the Lorentz ratio $L = \frac{\kappa}{\sigma T}$ of the sample. We do this by measuring the thermal conductance and electrical conductance of a single sample in exactly the same geometry. In this way, the geometrical factors involved in the calculation of the thermal and electrical conductivities drop out, and we are left with a geometry-independent measure of the different contributions to the thermal conductivity. An electronic system with elastic scattering will display a Lorentz ratio[4] which is near to the theoretical value for electrons, $L_0=2.45 \times 10^{8}$ W-Ω/K^2. Thus a comparison of the measured Lorentz ratio to the expected value for electrons permits separation of the electronic and lattice contributions to the thermal conductivity, with any thermal conductivity in excess of the expected electronic contribution coming from phonons.

Figure 7.3 shows the measured Lorentz ratio of a typical SWNT sample from 300 K to 8 K. At all temperatures, this value is at least two orders of magnitude larger than the

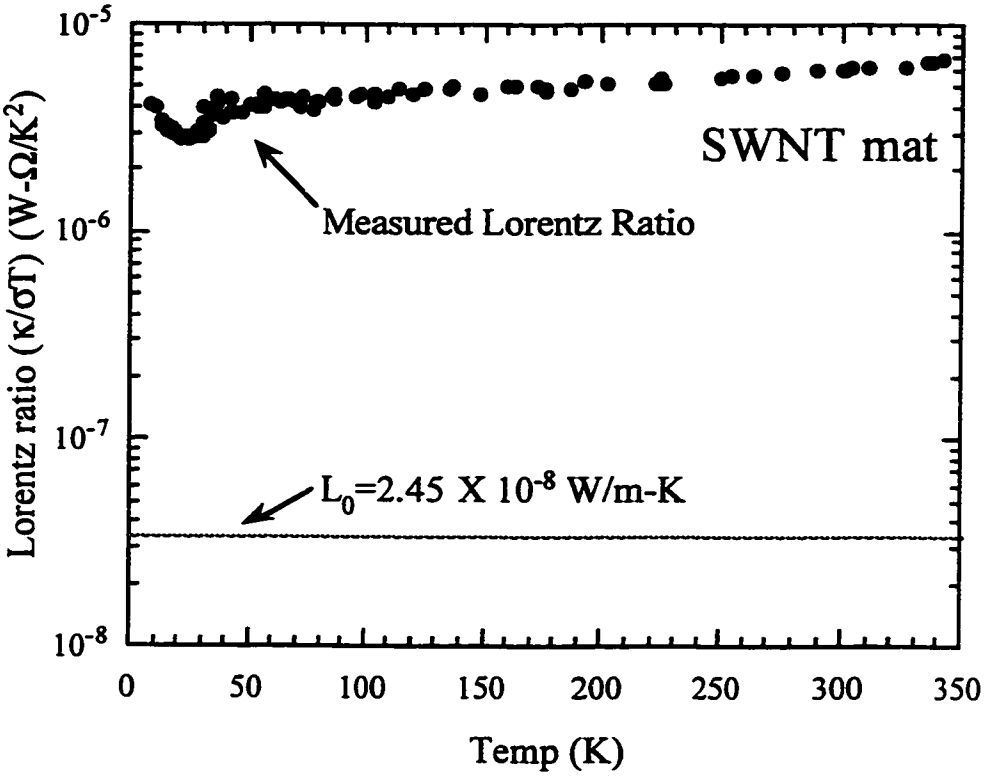

Figure 7.3 Lorentz Ratio of single-walled nanotubes

expected value for a purely electronic system. Thus we conclude that the thermal conductivity of single-walled nanotubes is dominated by phonons at all temperatures. We will attempt in the next sections to understand how the observed temperature-dependence, especially the linear low-temperature behavior, can be a result of phonon thermal conductivity in a nanoscale system. Finally, we note that the sintered SWNT sample displays the same Lorentz ratio as the mat samples; its electrical and thermal conductivities are reduced in equal proportions.

7.5 Thermal Conductivity of Graphite and Carbon Fibers

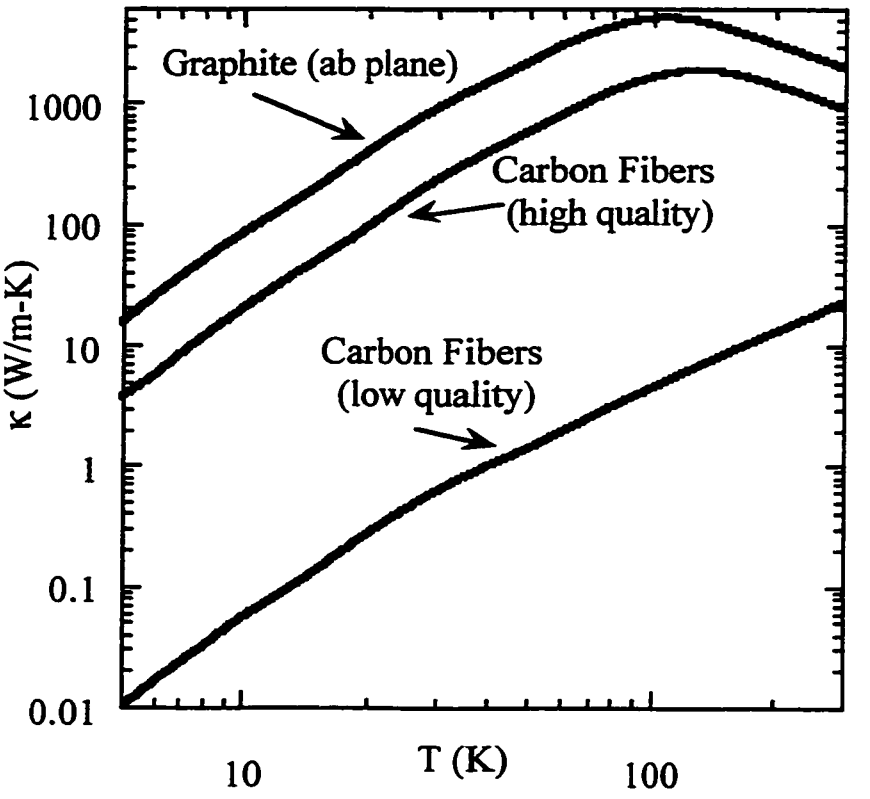

Figure 7.4 Thermal conductivity of graphite and carbon fibers

Figure 7.4 represents the published thermal conductivity of graphite[1] and two representative carbon fiber samples[5] as a function of temperature. In both of these materials, the thermal conductivity is dominated by phonons, and the behavior of the phonon thermal conductivity reveals the dimensionality of the phonon structure. Graphite, which is close to 2-d, shows a T^2-like temperature dependence, in contrast to 3D materials which show a T^3 temperature-dependent thermal conductivity. At higher temperatures, phonon-phonon Umklapp scattering causes the thermal conductivity to decrease with increasing temperature with a roughly 1/T dependence. The crossover temperature occurs when the

phonon-phonon scattering time is approximately equal to the defect scattering time. The high-quality carbon fibers are almost as crystalline as high-quality graphite, and therefore display a crossover temperature which is only slightly higher. Because low-quality carbon fibers are significantly less crystalline, their thermal conductivity is significantly lower and defect scattering dominates up to above room temperature.

7.6 Model for the Thermal Conductivity of SWNT's

We will attempt to understand the thermal conductivity of single-walled nanotubes by modeling the behavior of a single nanotube with a 1.4-nm diameter. We will use a tube of the (10,10) variety as a model, although the chirality should not be important.

The diagonal component of the thermal conductivity tensor of a phonon system in a simple model[6] is given by

$$\kappa_{zz} = \sum C v_z^2 \tau, \tag{7.2}$$

where C is the specific heat, v is the phonon group velocity, τ is the scattering time, and the sum is over all phonon states. As a first step, we will calculate the expected thermal conductivity of a (10,10) tube in a constant-scattering-time model; a constant-scattering-time approximation should be valid at low temperatures and close to valid at moderate temperatures, until phonon-phonon Umklapp scattering begins to be important. The calculation can be further simplified by considering only the acoustic phonon branches in the tubes; optical phonons will have a low group velocity, and will be thinly populated at low temperatures, so should not contribute appreciably to the thermal conductivity given by Eq. (7.2).

There are four acoustic phonon branches in a single-walled nanotube: one longitudinal (LA), two transverse (TA), and one 'twist' branch. These modes are diagrammed below in figure 7.5. The sound velocities of the LA and TA modes have been calculated by tight-binding methods[7], which yield $v_{LA} = 1.65 \times 10^6$ cm/s and $v_{TA} = 7.5 \times 10^5$ cm/s. In addition, neutron scattering measurements of graphite[8] yield $v_{LA}(\text{graphite}) = 2.8 \times 10^6$ cm/s and $v_{LA}(\text{graphite}) = 1.1 \times 10^6$ cm/s; these velocities should be similar to $v_{LA}(\text{tube})$ and $v_{twist}(\text{tube})$. Combining the two sets of data, we will use values of 2×10^6, 0.8×10^6, and 1×10^6 cm/s for the sound velocities of the longitudinal, transverse, and twist modes, respectively.

We now examine the phonon structure of nanotubes in more detail. In a simple picture, the phonon structure of a nanotube can be derived from that of a graphene sheet in the same way that the electronic structure is. The primary effect of turning a sheet into a tube is the quantization of the circumferential component of the phonon wavevector, which breaks the two-dimensional Brillouin Zone into linear 'subbands'[9, 10]. Figure 7.6 shows the subband structure of a (10,10) nanotube; the spacing in the circumferential direction is $\frac{1}{R_{tube}}$, so that a (10,10) tube will have one subband in the center and ten on each side.

The subband passing through the center of the B.Z. (the 'zeroth' subband) is unique in that it is the only subband which has $\omega \to 0$ as $k_z \to 0$: all other subbands have a finite minimum cutoff frequency. To determine the temperature scale corresponding to the subband separation, we assume that the acoustic phonons are isotropic and have a lin-

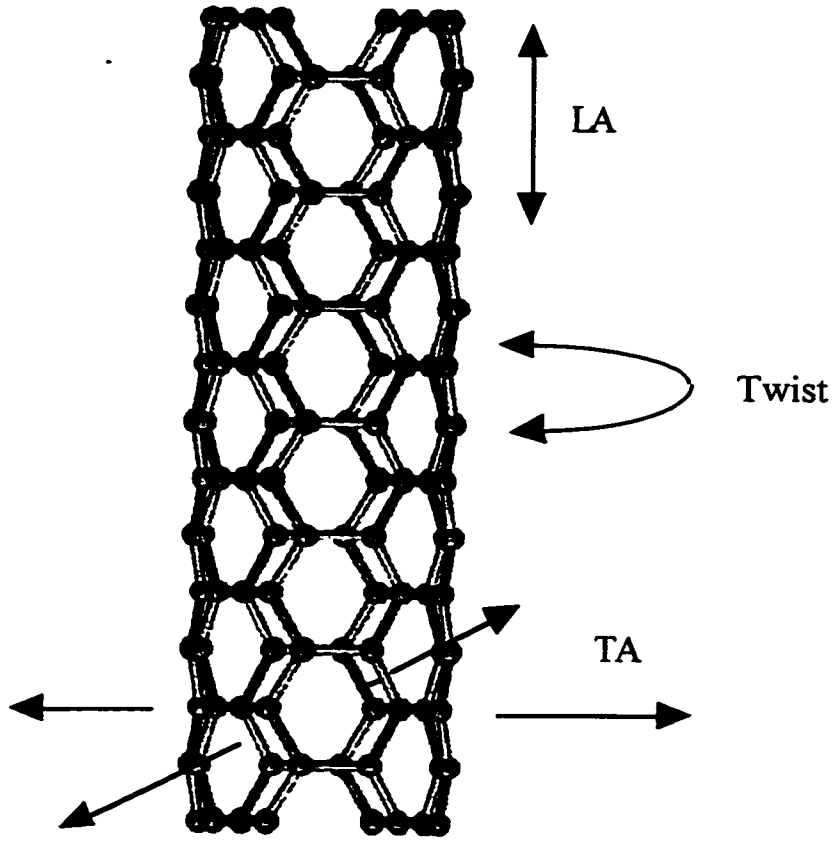

Figure 7.5 Acoustic phonon modes in a single-walled nanotube

ear dispersion relation, so that

$$\omega = v_s|k| . \tag{7.3}$$

Then the temperature which corresponding to the subband separation[11] is given by

$$T = \frac{\hbar v_s \Delta k}{k_B} = \frac{\hbar v_s}{k_B R} \tag{7.4}$$

Inserting the speed of sound for the acoustic phonon branches gives temperatures of 240 K, 95 K, and 120 K, for the longitudinal, transverse, and twist modes, respectively. These are on the same order of magnitude as the measurement temperatures, so we expect that

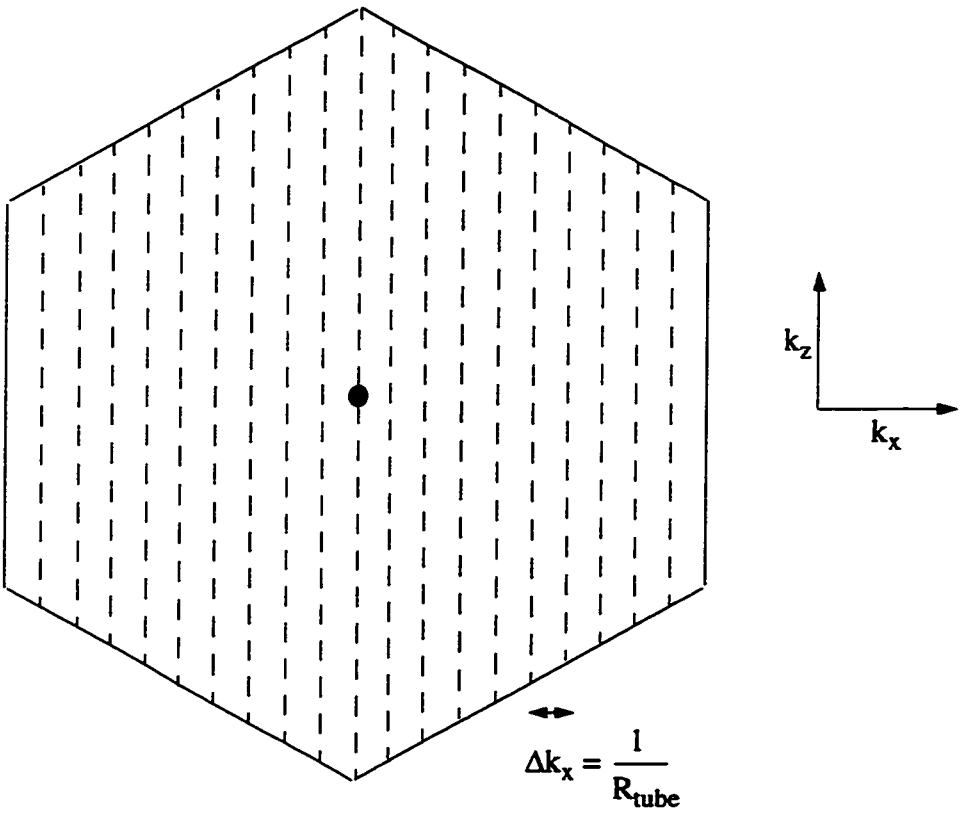

Figure 7.6 Subband structure of a (10,10) nanotube

this subband structure will in fact have a significant effect on the expected thermal conductivity.

Because of the quantization of the phonon structure, we will calculate the expected thermal conductivity of each subband separately using equation 7.2. To do this we first use the specific heat of a single phonon state[4],

$$C = \frac{\hbar^2 \omega^2 \tilde{n}(\tilde{n}+1)}{k_B T^2} \tag{7.5}$$

where $\tilde{n}$, the average number of phonons occupying the state, is given by

$$\bar{n} = \frac{1}{e^x - 1} \tag{7.6}$$

with $x = \frac{\hbar\omega}{k_B T}$. To convert the sum into an integral, a one-dimensional density of states

$$g(\omega) = \frac{1}{\pi v_s} \tag{7.7}$$

is sufficient for the 'zeroth' subband, which comprises only wavevectors along the z axis. Other subbands have a zero density of states up to a finite minimum cutoff frequency $\omega_{cutoff} = n\omega_0 = n\frac{v_s}{R_{tube}}$, and then a density of states described by

$$g_n(\omega) = \frac{1}{\pi v_s} \frac{\omega}{\sqrt{\omega^2 - n^2\omega_0^2}} \tag{7.8}$$

beyond the cutoff. Finally, we find the axial component of the group velocity:

$$v_z^2 = v^2 \frac{\omega^2 - n^2\omega_0^2}{\omega^2} \tag{7.9}$$

After equation 7.2 has been evaluated using an appropriate density of states, the resulting expression for the thermal conductivity of the n^{th} phonon subband is

$$\kappa_n = T\frac{2k_B^2 v\tau}{\pi\hbar} \int_{nx_0}^{(x_{max})_n} x\sqrt{x^2 - (nx_0)^2}\, \frac{e^x}{(e^x - 1)^2} dx \ , \tag{7.10}$$

where the limits of the integral represent the minimum cutoff for the subband and the zone edge, respectively.

Equation 7.10 can be evaluated numerically for a given temperature and phonon

branch. Figure 7.7 shows the results of that calculation, as a function of temperature, for all ten subbands of the twist mode. The 'zeroth' subband provides a linear $\kappa(T)$at low temperatures, because the integral in equation 7.8 is essentially constant. At higher temperatures, the finite maximum phonon temperature (1080 K for the twist mode) takes effect and the expression becomes sub-linear. Higher-order subbands, on the other hand, show markedly different low-temperature behavior due to their finite minimum frequencies. At low temperature, they are not populated and therefore do not contribute to the thermal conductivity. The first subband begins to contribute near 30 K, just the point at which the measured thermal conductivity departs from linearity; higher subbands begin to contribute at even higher temperatures. Thus a nanotube should display a thermal conductivity which is due to a single one-dimensional phonon subband at low temperatures. Finally, we note that the contribution from the zeroth subband is smaller than that of the higher subbands; this is because there are two identical subbands for all higher subbands, but only one for the zeroth subband.

Figure 7.8 shows the expected thermal conductivity of TA, LA, and twist phonon branches, calculated using equation 7.10, and assuming a constant scattering time. All three show qualitatively similar behavior: linear temperature dependence at low T, then an increase in slope around 30 K. At higher temperatures, the three branches show different curvature: the LA mode, with the highest sound velocity, has the highest Debye temperature, and therefore displays upward curvature to higher temperatures than the TA and twist modes.

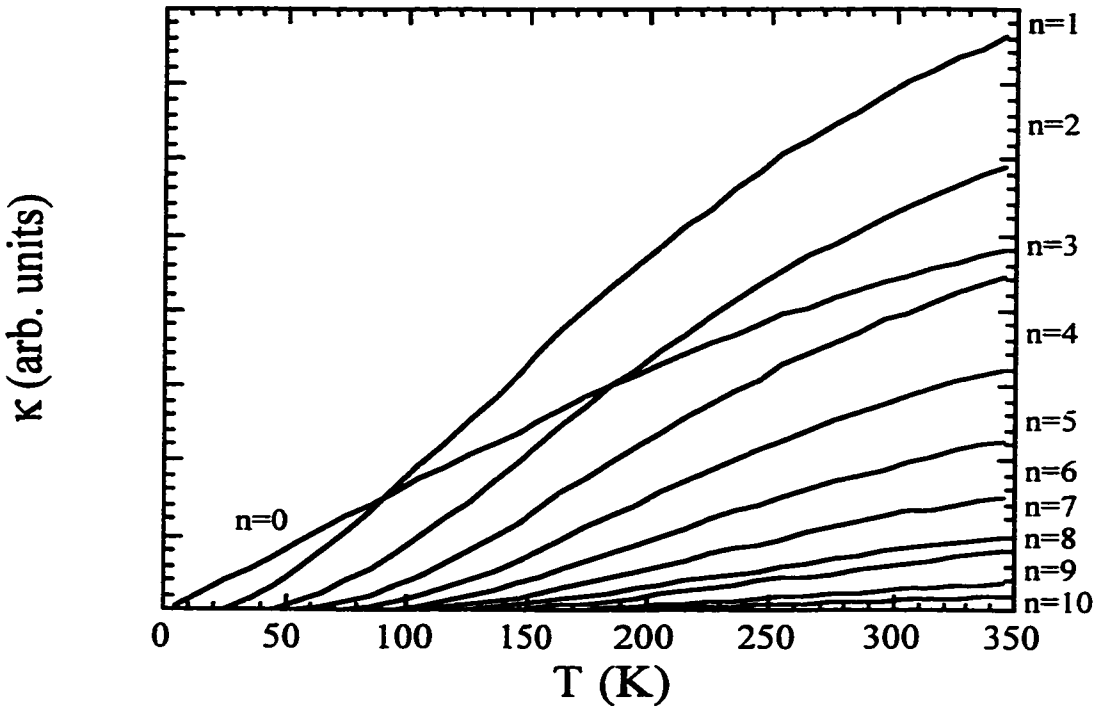

Figure 7.7 Thermal conductivity of 'twist' mode subbands

7.7 Comparison of Model and Experiment

The total expected thermal conductivity derived from the constant-scattering-time model can be obtained by summing the contributions, as shown in figure 7.8, from all four acoustic phonon branches (LA, twist, and 2 X TA). The result is a model for the thermal conductivity of a 1.4-nm - diameter nanotube which has only one free parameter, the constant scattering time τ. At high temperature, τ will decrease due to electron-phonon and phonon-phonon scattering, while at low temperatures it should be constant. Therefore we choose the value of τ by fitting the model to the low-temperature data. Figure 7.9 depicts the low-temperature data and model, where the model has been scaled to match the linear portion of the data below 25 K. The model shows identical linear behavior below that

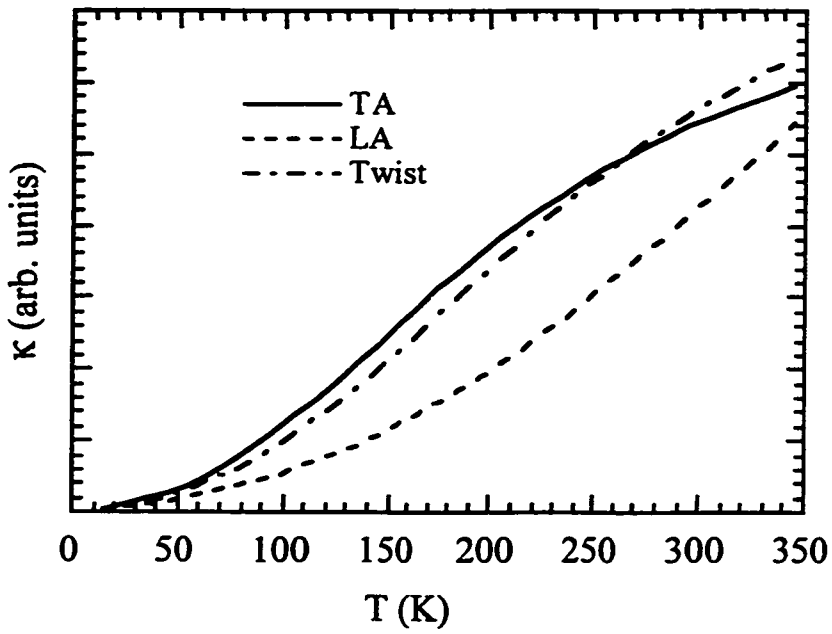

Figure 7.8 κ(T) of the TA, LA, and twist acoustic phonon branches

temperature, and a departure from linearity above, although it does not duplicate the sharpness of the change in slope in the measured data. Nevertheless, the close agreement between the linear-nonlinear crossover temperatures is strong confirmation that the one-dimensional phonon thermal conductivity of the model is the correct explanation for the observed low-temperature linear κ(T).

Figure 7.10 shows the prediction of the model and the measured data over the entire measured temperature range. The scaling is the same as is used in figure 7.9. The model, when scaled to match the low-temperature data, overestimates the high-temperature thermal conductivity. This is to be expected: the scattering time should decrease with increasing temperature. Nonetheless, the model and experiment agree to within 30%. Both show qualitatively the same features: strictly linear low-temperature behavior, a departure from linearity in the range 25-30 K, and behavior above that temperature which

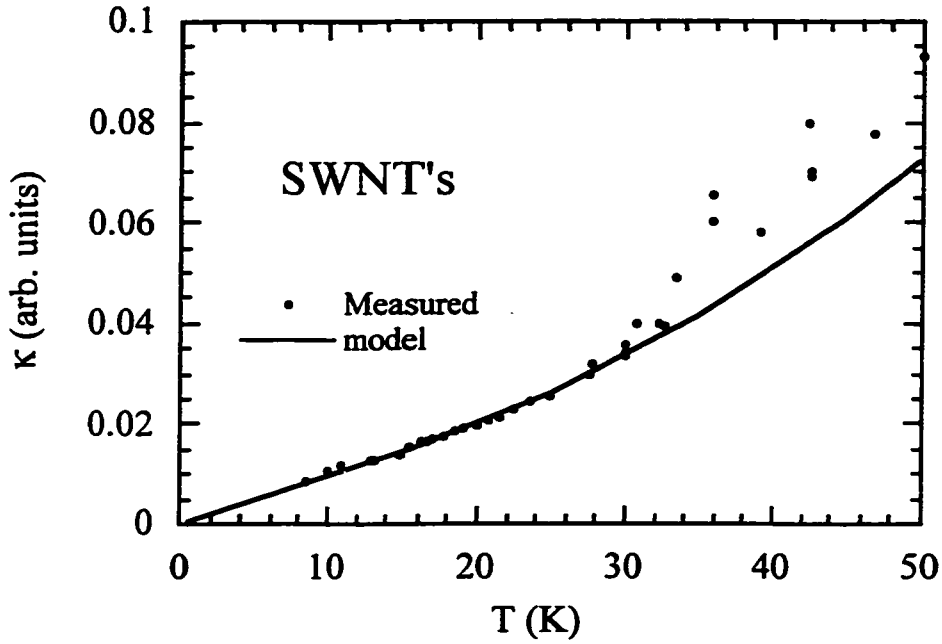

Figure 7.9 Low-temperature scaling of model and measured data

is close to linear.

A comparison of the model and data for the linear low-temperature region allows us to extract a value for the scattering time τ. At low temperatures, the value of the integral in equation 7.10 is $\frac{\pi^2}{3}$, so that the expected thermal conductivity is given by

$$\kappa(T < 25K) = T\frac{4\pi k_B v\tau}{3\hbar} \tag{7.11}$$

Equation 7.11 gives a 1-D thermal conductivity, with units W-m/K. To convert it to a 3-D thermal conductivity, we divide by the cross-sectional area (1.7 nm^2) per tube in a rope of tubes. We can then compare the measured thermal conductivity to equation 7.11. A value of 2000 W/m-K for the room-temperature thermal conductivity of a rope gives a scattering

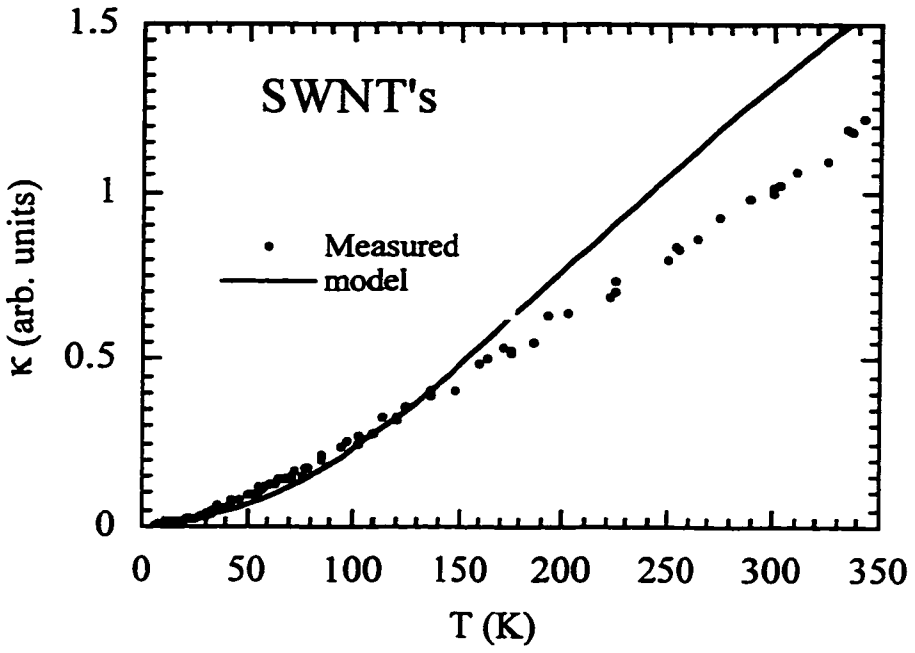

Figure 7.10 Comparison of model and data over entire temperature range

time of 10^{-11} s. Inserting a phonon sound velocity of 10^6 cm/s, this scattering time translates to a scattering length of 100 nm. This is considerably less than the length of a single tube. It is, however, on the same order as the distance between inter-rope contacts in SWNT mat samples. This suggests a possible mechanism for phonon scattering: phonons might scatter at a rope-rope contact because of the effectively higher mass of the rope at the contact point. This mechanism would also imply that the contacts between ropes are mechanically strong. Finally, it would offer an explanation for the reduced thermal conductivity of the sintered tubes: a higher density of rope-rope junctions leads to a shorter scattering length.

Finally, we examine the high-temperature behavior of the $\kappa(T)$ of SWNT's. It does not exhibit the decrease at high temperatures that is observed in graphite and carbon

fibers. This could be due to two effects. First, the level of crystallinity in the SWNT's could be lower than that of high-quality graphite and carbon fiber samples, so that defect scattering dominates the thermal conductivity, as in low-quality carbon fiber samples. However, the high thermal conductivity determined in section 7.3 argues against this interpretation. Another possibility is that the low dimensionality of nanotubes affects the scattering: in 1-D, scattering is suppressed because it is impossible to conserve both energy and momentum if the phonon bands are not perfectly linear. Further experimental study of the high-temperature thermal conductivity of SWNT's should help elucidate this point.

7.8 Thermal Conductivity of Multiwalled Tubes

Because multiwalled tubes are larger than SWNT's, and have a number of concentric walls, we expect that the effects of reduced dimensionality in these materials will be significantly reduced. To test this hypothesis, the thermal conductivity a number of MWNT samples was measured. The samples were slices cut from a 'boule' (the growth on the cathode in the carbon arc) which was found to have a high concentration of MWNT's. Measurements were performed by the same comparative method as was used in the previous study.

Figure 7.11 shows the thermal conductivity of a MWNT sample from 300 K to 8 K. The bulk thermal conductivity of MWNT samples was determined to be $\approx$ 65 W/m-K at room temperature. The data are plotted on a logarithmic scale (base 10) to highlight the temperature dependence of κ. The data below 150 K can be fit by a straight line, indicating a power-law temperature dependence. The slope of this line gives an exponent of 1.8.

Thus multiwalled tubes behave much like graphite, except that they display a $T^{1.8}$ temperature dependence instead of $T^{2.3}$, as is reported for graphite. This behavior is consistent

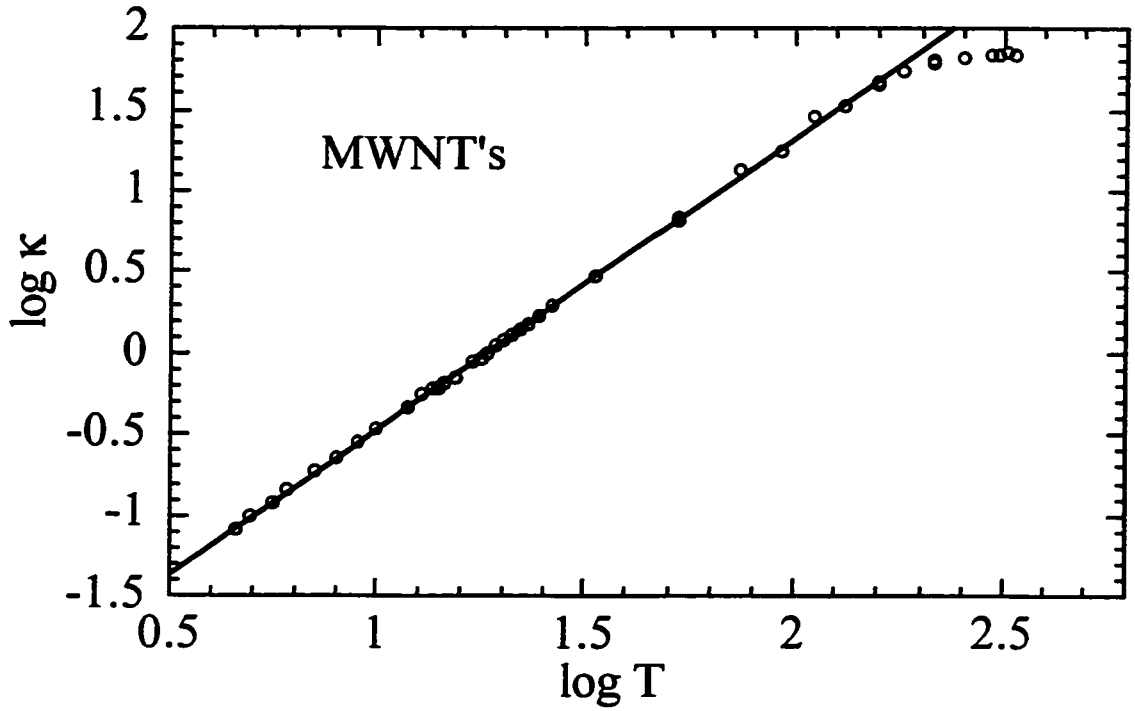

Figure 7.11 Thermal conductivity of multiwalled nanotubes

with the observed larger diameter of MWNT's compared to SWNT's: running the model developed in section 7.6 for a tube of 5-nm diameter produces a thermal conductivity which shows approximately $T^{1.9}$ temperature dependence over the measured temperature range, in good agreement with the observed data. Furthermore, the low-temperature behavior of the MWNT's reinforces the conclusion that the linear $\kappa(T)$ of SWNT' s at low temperature is an effect of dimensionality: because the MWNT's have a larger diameter, they should show one-dimensional behavior only at temperatures below those of the above measurement. On the other hand, if the linear $\kappa(T)$ were an effect of disorder or

sample morphology, it should appear in both SWNT and MWNT samples. We also note that the measured $\kappa(T)$ of MWNT's plateaus above 150 K, just as it does in graphite, indicating that the phonon mean free path is similar in the two materials. It was mentioned above that the lack of a similar plateau in the $\kappa(T)$ of SWNT's could be due to either their reduced dimensionality or a larger degree of disorder in SWNT's compared to graphite. Since MWNT's and SWNT's should have a similar degree of crystallinity, the observation of a plateau in the $\kappa(T)$ of MWNT's lends strength to the first scenario.

Chapter 7 References

1. Y. S. Touloukian, P. E. Liley, and S. C. Saxena, *Thermal conductivity: nonmetallic liquids and gases* (IFI/Plenum, New York, 1970).

2. R. S. Ruoff and D. C. Lorents, Carbon **33**, 925-30 (1995).

3. J. E. Fischer, H. Dai, A. Thess, *et al.*, Physical Review B (Condensed Matter) **55**, R4921-4 (1997).

4. C. Kittel, *Introduction to solid state physics* (Wiley, New York, 1996).

5. J. Heremans and C. P. Beetz, Jr., Physical Review B **32**, 1981 (1985).

6. J. E. Parrott and A. D. Stuckes, *Thermal conductivity of solids* (Pion, London, 1975).

7. J. Yu, R. K. Kalia, and P. Vashishta, J. Chem. Phys **103**, 6697 (1995).

8. R. Nicklow, N. Wakabayashi, and H. G. Smith, Physical Review B **5**, 4951 (1972).

9. J. W. Mintmire and C. T. White, Carbon **33**, 893-902 (1995).

10. Noriaki Hamada, Shin-ichi Sawada, and Atsushi Oshiyama, Physical Review Letters **68** (1992) 1579-1581

11. L. X. Benedict, S. G. Louie, and M. L. Cohen, Solid State Communications **100**, 177-80 (1996).

Chapter 8.

Postassium-Intercalation of Individual SWNT Bundles

8.1 Motivation

Soon after the bulk synthesis of high-quality samples of SWNT bundles, it was discovered that these bundles can be intercalated with a number of materials, in a process analogous to the intercalation of C_{60} and graphite. So far, the list of intercalants includes the alkali metals K, Rb, and Cs, and Br and I. TEM studies[1] have shown that the intercalants occupy the interstitial sites between the parallel tubes in a bundle. In each case, intercalation of mats of SWNT's results in the reduction in the resistivity of the material[2], typically by a factor of order 10. In addition, intercalation suppresses the low-temperature resistivity upturn in observed in SWNT mats. In most samples, the metallic-nonmetallic crossover temperature T^* decreases by tens of K, but some samples have been reported to be metallic down to 4.2 K. Because bulk samples contain so many different types of SWNT's, and because the role of inter-tube connections is still unclear, it is difficult to draw conclusions about the intercalation-induced changes in the SWNT electronic structure from experiments on bulk samples. Therefore, we attempted to repeat these experiments on individual SWNT ropes. These experiments, which are ongoing, were carried out in collaboration with Marc Bockrath in the McEuen group.

8.2 Devices for Electrical-Transport Measurements of Individual SWNT's and SWNT Bundles

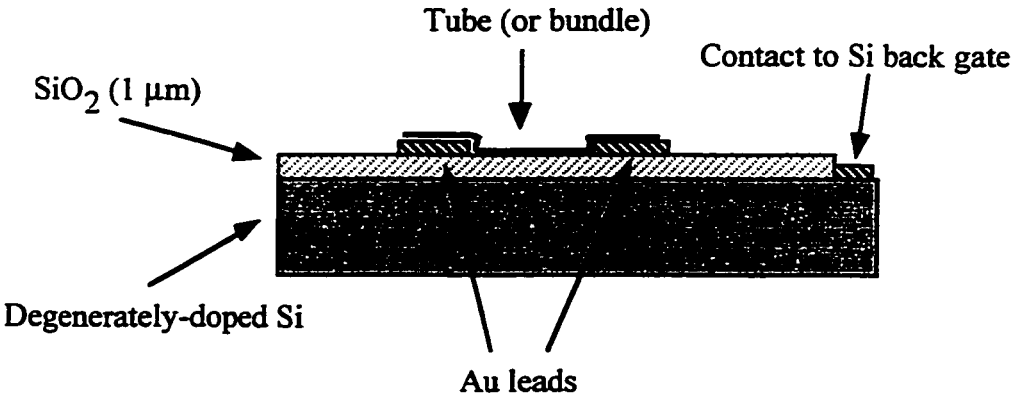

Figure 8.1 Two-probe electrical measurement of individual SWNT's

As was mentioned in chapter 6, a number of techniques have been developed to make electrical contacts onto individual SWNT's and SWNT bundles. For this experiment, the samples were measured using a device diagrammed in figure 8.1. A series of parallel Au electrodes were patterned, using electron-beam lithography, on a piece of a degenerately-doped silicon wafer with a 1-μm oxide layer on the top surface. Small amounts of SWNT material were dispersed in Dichloroethylene (DCE) by one hour of sonication. The dispersion was then placed onto the substrate, and quickly rinsed with isopropyl alcohol. Tubes, with their high surface area-to-volume ratio, adhere quite strongly to the substrate. Therefore, any tubes which are were in contact with the substrate when the solvent was rinsed away remained in place. The device was then tested to see if any tubes have made electrical contact between neighboring electrodes; the process was repeated until a sufficient number of tubes had been contacted. The device was subsequently examined with an atomic force microscope (AFM) to determine whether the electrical contacts were due to single tubes, single bundles, or multiple tubes/bundles: all of

the following measurements were performed on single bundles consisting of on the order of ten tubes, as determined from profiling using the AFM. Finally, after the device was characterized with AFM, it was glued into a standard chip cartridge and leads are wire-bonded to the cartridge, so that the device could be mounted onto a number of different measurement stations.

8.3 Electrical Measurements of Individual SWNT Bundles

Because the degenerately-doped silicon wafer has metallic conductivity, a SWNT bundle mounted as in figure 8.1 forms a three-terminal device: a bias voltage can be applied between the two gold electrodes, and a gate voltage can be applied using a contact to the silicon wafer. We measured current through the device as a function of applied bias at constant gate voltage, and as a function of gate voltage at a constant small bias ($eV < k_BT$).

Because of the small size of SWNT devices, a number of precautions must be taken to avoid damaging the tubes. First, the current which passes through the device must be kept small enough. An ordinary resistance measurement, in which a constant current is passed through the device and the voltage is measured, is risky: if the tube has a high resistance, the current supply tries to supply the specified current by increasing the applied voltage, which can 'blow up' the device. Therefore, we used a voltage source and measured the current passing through the device with a current amplifier. The voltage was normally kept in the mV range. The second danger to the SWNT devices is static buildup: a small potential across the electrodes can cause too large a current to pass through the tubes, or cause the tubes to be electrostatically repelled from the substrate. Therefore,

when not being measured, all leads were grounded. Finally, induced EMF's are also dangerous; all leads were carefully shielded. The specific steps taken to safely measure the SWNT devices will be detailed below.

8.4 Experimental Setup

The two classes of SWNT intercalation compounds each pose difficulties for performing measurements on intercalated bundles. Br- and I- intercalated SWNT bundles are air-stable, but Br and I are highly corrosive and will react with the gold leads to the sample. The alkali metals will not react with gold, but alkali-metal-intercalated SWNT's are air-sensitive. We decided to study alkali-intercalated tubes, and therefore designed an apparatus to perform the intercalation and measure the sample in a sealed evacuated vessel.

Figure 8.2 shows the two-part vessel used to intercalate individual SWNT devices. The SWNT device cartridge is inserted in a holder made of ceramic and 16 gold pin sockets. The socket is held at the end of a stainless steel tube which is threaded to accept a temperature-sensor assembly. The tube is hard-soldered into a steel plug, along with another, thin, tube which is used as a wire feedthrough. The plug is then soldered onto a 1" steel VCR fitting. Wires are attached to the gold pins using silver epoxy, fed through the thin tube, and soldered onto a 16-pin socket; torr seal epoxy is used to make a vacuum seal where the wires exit the small tube. The other part of the assembly consists of sections of 3/4" and 1/2" pyrex tube, with the 3/4" tube joined to a 3/4" steel tube at a glass-to-metal seal. The steel tube is welded onto a 1" VCR fitting. The cartridge with the SWNT devices was plugged into the gold pins, and the two halves were joined in a vac-

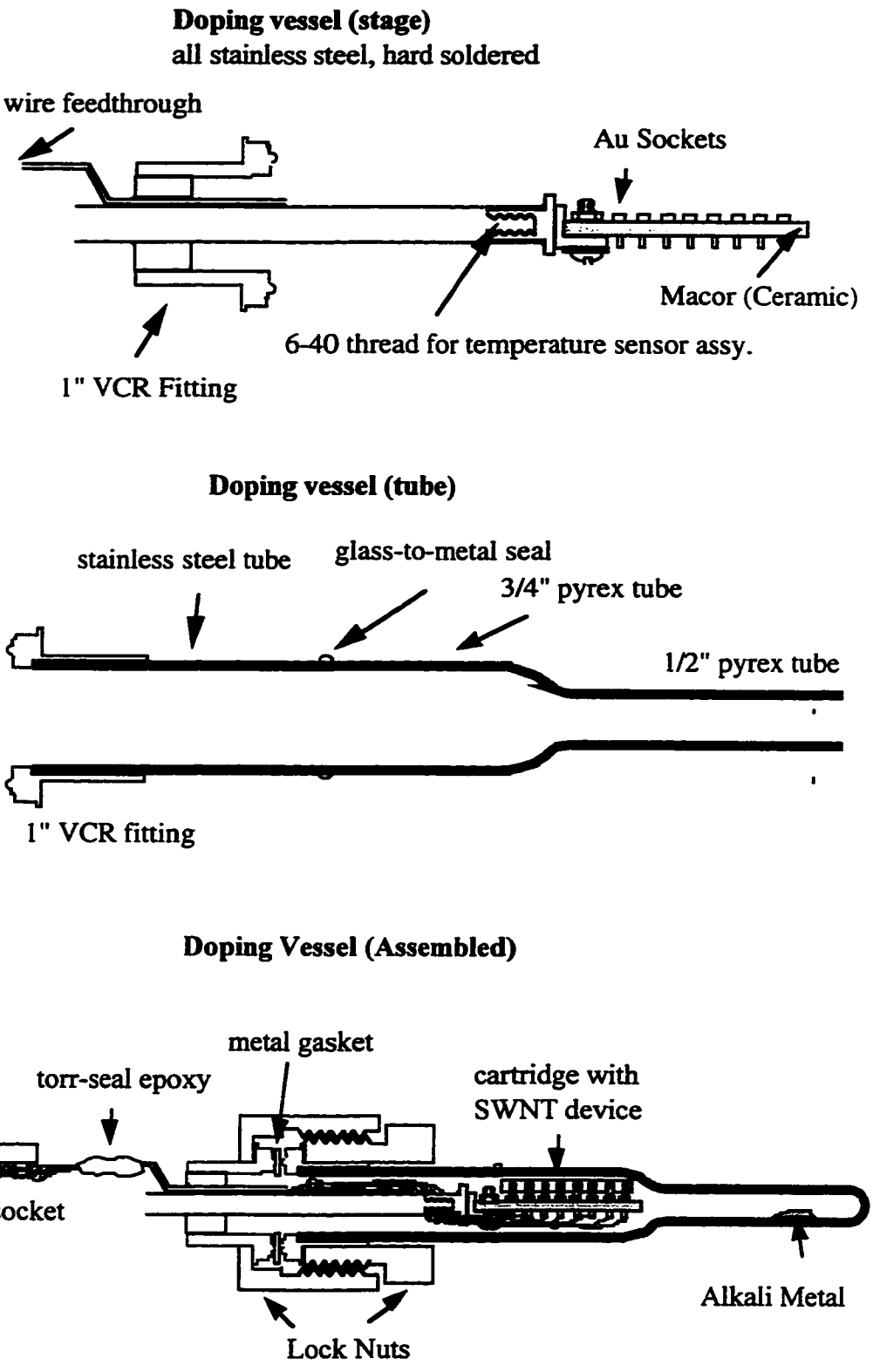

Figure 8.2 Vessel for alkali-metal intercalation of SWNT bundles

Figure 8.3 Sealed intercalation vessel

uum-tight seal using a metal gasket and two locking nuts. The assembly was leak-tested after the halves were joined.

After initial measurements, the assembly was wrapped in heater tape and baked out at 200 °C under dynamic vacuum, then loaded into an inert-atmosphere glove box, where alkali metal (in this study, potassium was used) was inserted into the glass tube. The tube was then sealed under dynamic vacuum. For doping, two sections of heater tape were wrapped around the vessel: one at the sample end and one at the alkali end. The temperatures of the two sections were monitored with thermocouples, and the temperature near the sample was monitored with a third thermocouple, mounted into a threaded insert which screws into the socket behind the sample.

To protect the setup from induced EMF's, all elements were carefully shielded. The doping vessel was wrapped in grounded aluminum foil, and the wires were fed into a grounded shielded box with BNC outputs. The heater tape was powered using dc power supplies rather than the usual ac temperature controllers; the heater tapes were attached to the power supplies, and the power supplies turned on, before wrapping the tapes around the apparatus, in order to avoid inductive pickup from current spikes.

8.5 Electrical Measurements Before Intercalation

Generally, SWNT devices either behave as metals or semiconductors; we will present the results of attempts to potassium-intercalate one of each type of device. Metallic devices are characterized by a relatively high conductivity and very little sensitivity to gate voltage; figure 8.4 shows the conductance vs. gate voltage of the metallic device used in this study. Semiconducting devices, on the other hand, display a smaller conductivity

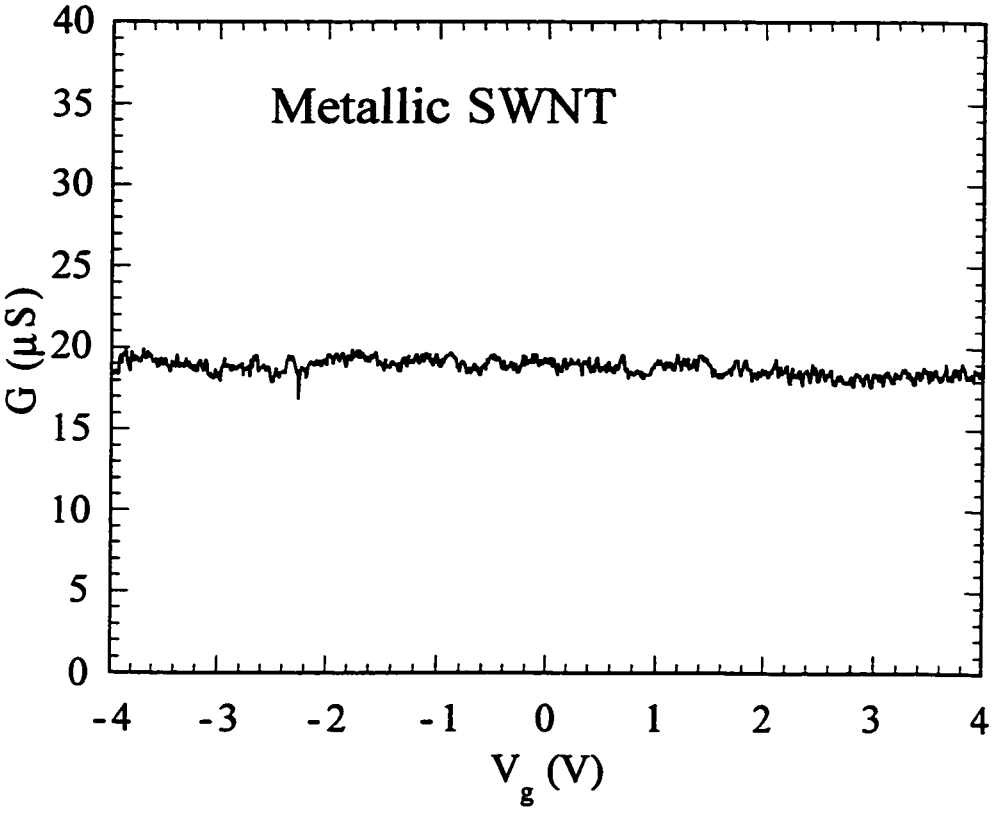

Figure 8.4 Conductivity vs. gate voltage of a metallic SWNT device

which is highly sensitive to gate voltage[3]. Figure 8.5 shows a similar plot for a semicon-

ducting tube: its conductance increases exponentially with decreasing gate voltage from V_g= +8 V to V_g = -5 V, at which points it saturates to a maximum value. Figure 8.6 repre-

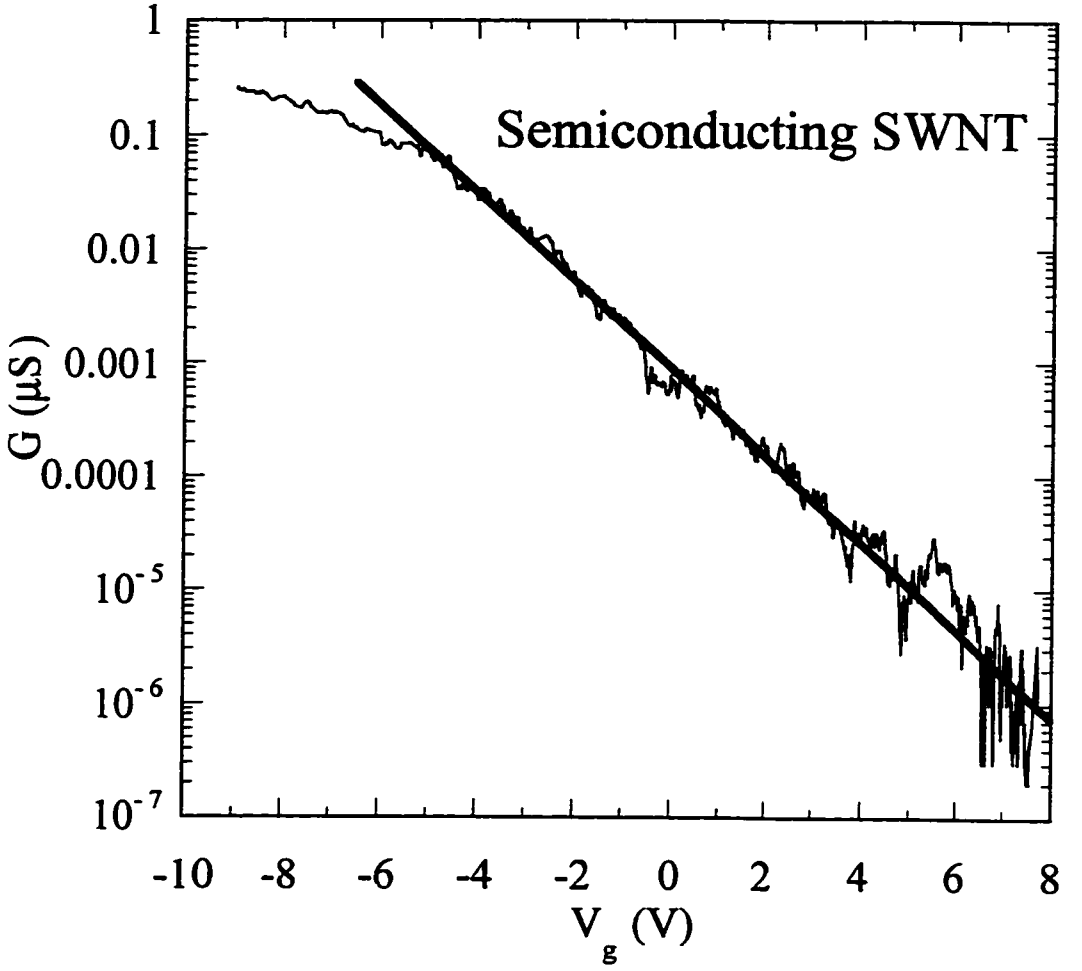

Figure 8.5 Conductance vs. gate voltage of a semiconducting SWNT

sents the transport characteristics of the semiconducting SWNT device used in this study. It has very small conductance at zero or positive gate voltage, as is shown by the I-V curve at V_g= 0. At negative gate voltage, on the other hand, the conductance increases dramati-

cally, as is shown by the I-V curve at $V_g = -9V$. This behavior is typical of semiconducting SWNT devices: all show a similar p-type gate voltage dependence.

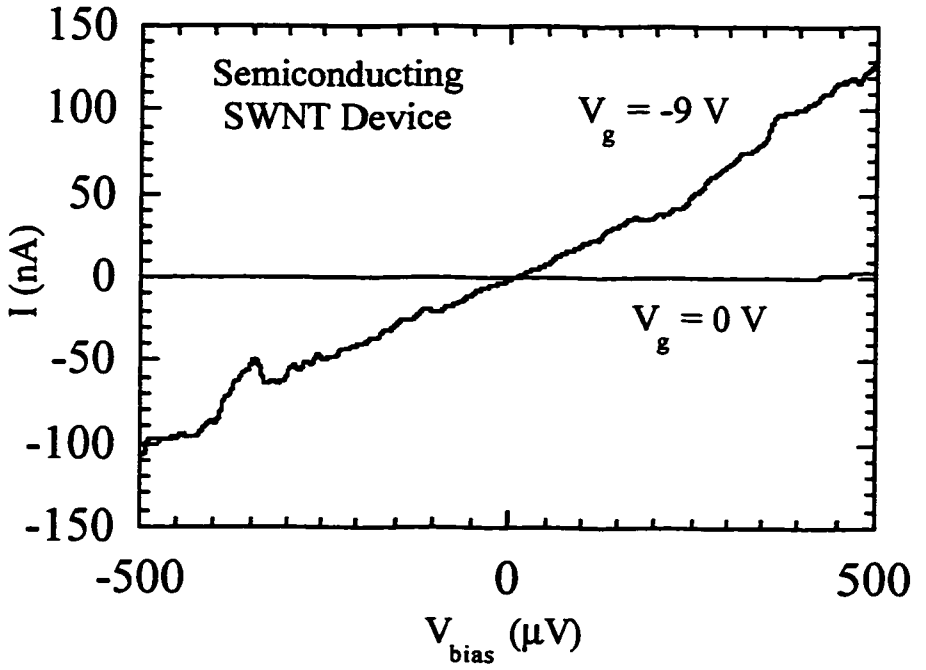

Figure 8.6 I-V curves of a semiconducting SWNT device at $V_g = 0$ and -9 V.

Figure 8.7 shows the $V_g = 0$ low-bias conductance of the semiconducting SWNT device upon baking in dynamic vacuum. As the system warms and reaches a final temperature of 200 °C, the conductance of the device decreases dramatically to almost unmeasurable levels at zero gate voltage; the conductance increases at negative gate voltage and the device thus remains p-type. The metallic device, on the other hand, did not exhibit a substantial change in conductance when heated. We believe that the observed change in behavior upon baking is evidence that SWNT bundles may already be intercalated in air, perhaps with oxygen or water. It is interesting to note that this result is consistent with the

change in the thermopower of bulk samples upon similar treatment.

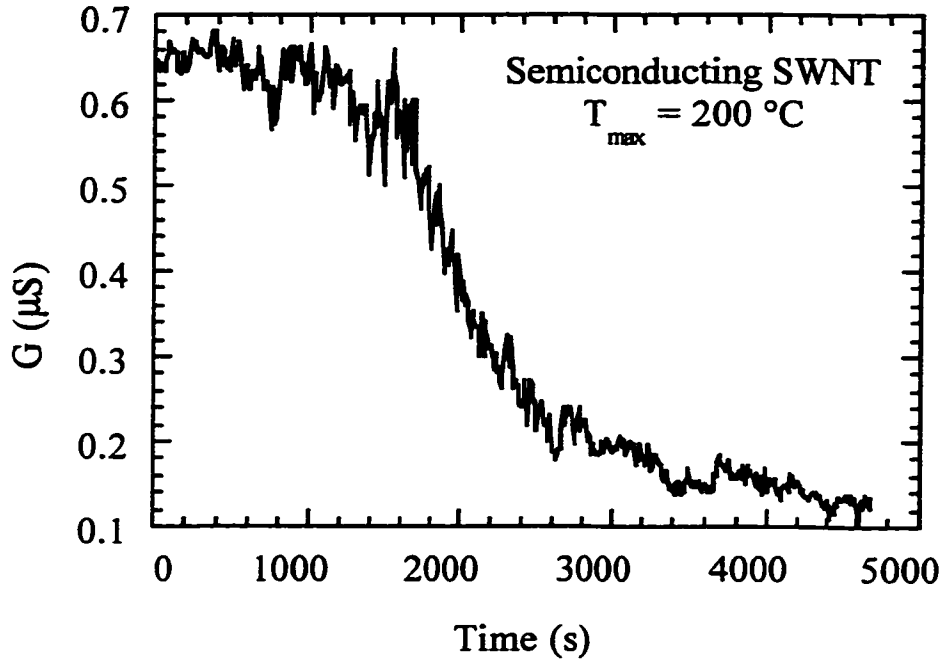

Figure 8.7 Conductance vs. time of a semiconducting SWNT device during baking at 200 °C.

8.6 Electrical Characteristics of Intercalated SWNT Bundles

Figure 8.8 shows the low-bias, zero-gate-voltage conductance vs. time of the semiconducting SWNT bundle as it is intercalated with potassium. In this case, the sample was held at 250 °C and the potassium was ramped up to a maximum temperature of 200 °C. As the potassium reached its maximum temperature (at t ≈ 1.5 h.), the conductance of the SWNT bundle increased dramatically and continued to rise for over an hour. At this point, the K and sample were cooled slowly, reaching room temperature at t ≈ 5 h. Upon cooling, the conductance of the device remained significantly higher than the conductance before intercalation. In contrast to the dramatic changes observed in the semiconducting

device, the metallic device showed little effect from intercalation.

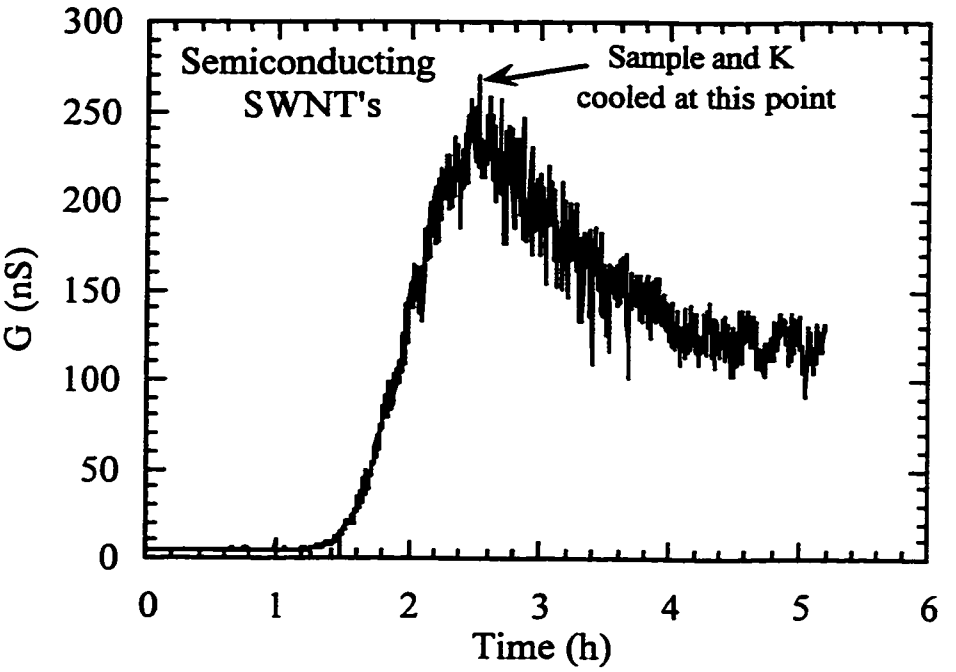

Figure 8.8 Conductance of a SWNT device upon K-intercalation

Figure 8.9 shows the room-temperature behavior of the intercalated semiconducting SWNT bundle as a function of applied gate voltage. The gate-voltage dependence has been reversed: the device is now n-type, showing a larger conductance at positive V_g. This change in gate-voltage dependence is strong evidence that the intrinsic behavior of the SWNT bundle, rather than the character of the SWNT-gold contacts, is being changed by potassium intercalation. Once again, no changes in the behavior of the metallic bundle were observed upon intercalation.

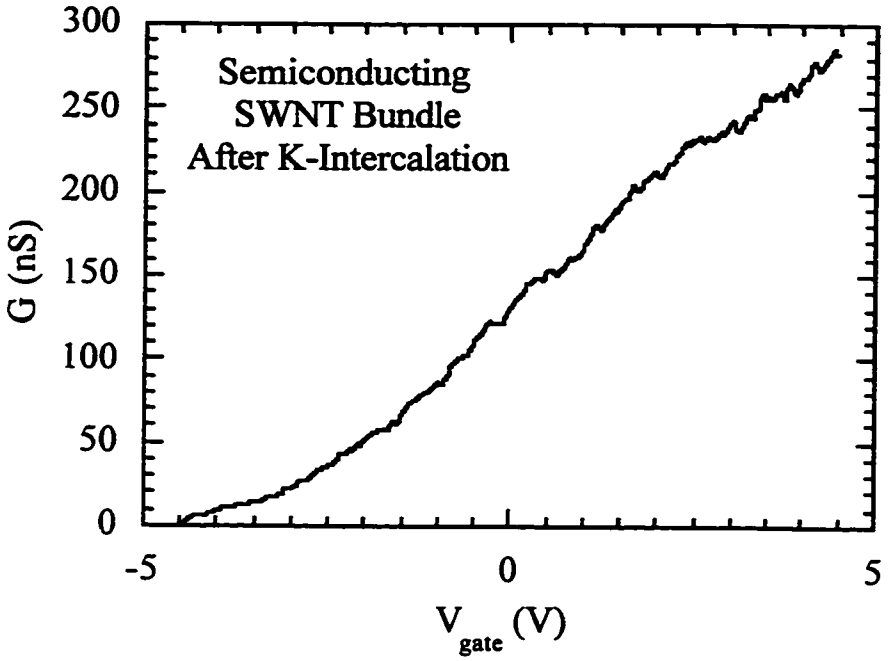

Figure 8.9 Conductance vs. gate voltage of a K-intercalated semiconducting SWNT bundle

8.7 Interpretation of Results

Although the microscopic details of the conduction process in SWNT devices will probably prove to be quite complicated, the gate-voltage-dependent behavior has been qualitatively interpreted using a semiclassical band-bending model[3]. We depict the details of the model below in figure 8.10. Figure 8.10 (a) shows the electron energy bands of the electrodes and a semiconducting tube before they are put in contact. The work function of a tube is 4.5 eV, vs. 5.7 eV for the Pt electrodes used in ref. 3, and 5.1 eV for the Au electrodes used in this study. Therefore, the valence band edge of the tube lies above the Fermi level of the electrodes. When the tube is placed in contact with the electrodes (through a low-conductance tunnel junction on each side), the bands of the tube bend

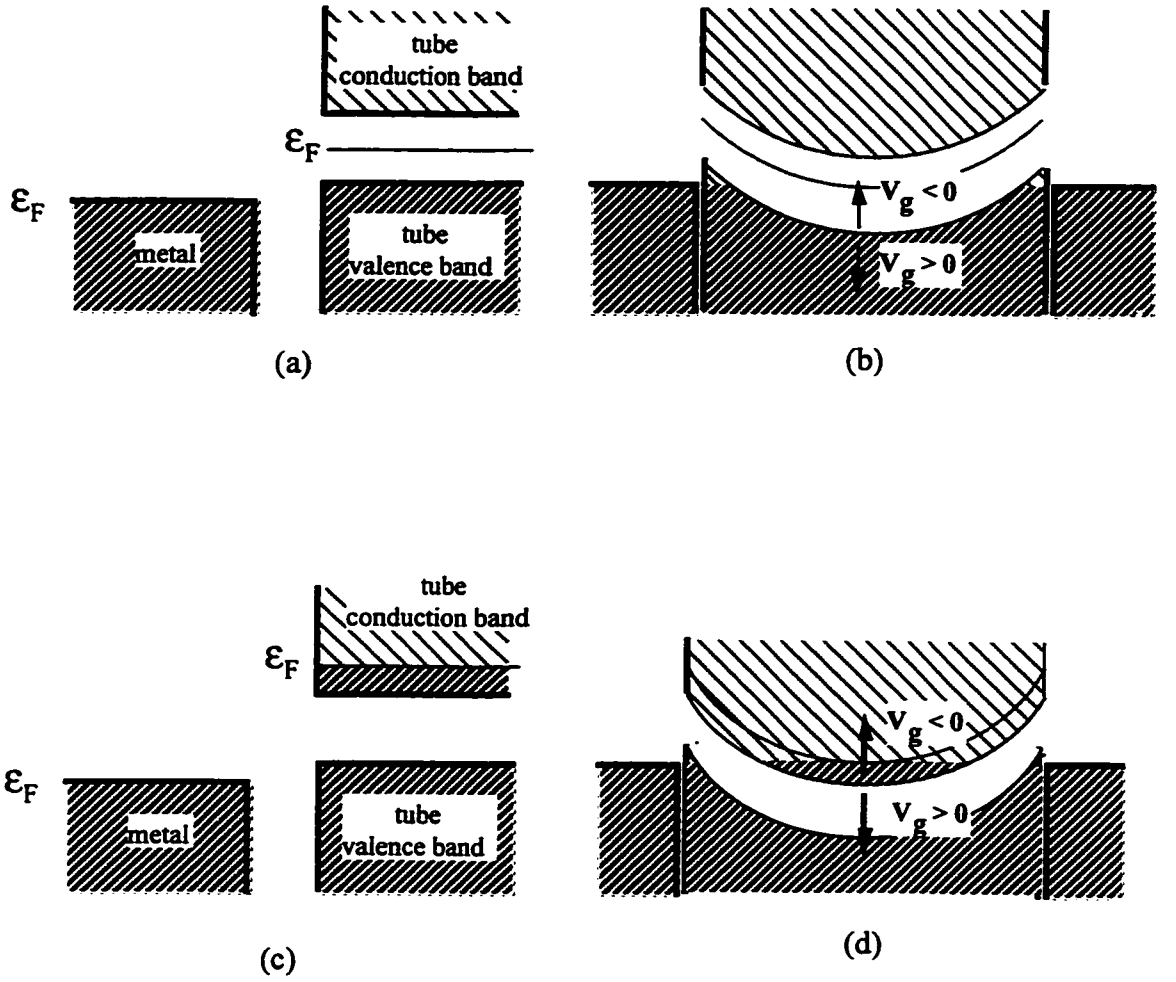

Figure 8.10 Band diagrams of undoped (a,b) and doped (c,d) nanotube devices

downward in order to match the tube Fermi level with the Fermi level of the electrodes, as is depicted in figure 8.10 (b). The areas of the tube near the electrodes become metallic, because the states above the Fermi level are emptied. Between these areas, the downward bending of the bands causes the center region of the tube to be insulating: electrons must tunnel from one side to the other. An applied gate voltage will shift the bands in the center region, while leaving them unaffected near the electrodes due to screening. Thus a nega-

tive gate voltage, which will move the bands upward, reduces the height and spatial extent of the tunnel barrier and increases the conductivity of the device. A positive gate voltage, on the other hand, will decrease the conductivity of the device.

The doped tube device is depicted in figure 8.10 (c) and (d). Alkali-metal doping donates electrons to the tube and moves the Fermi level into the conduction band. As before, the bands bend downward in the area between the electrodes. In this case, however, the center of the tube becomes metallic, and is separated from the area near the electrodes by tunnel barriers. As the doping level increases, the Fermi level of the tube moves upward, resulting in smaller tunnel barriers and an increased conductivity, consistent with the observed behavior (figure 8.7). Similarly, a positive gate voltage bends the bands downward and shrinks the tunnel barriers, while a negative gate voltage enlarges the tunnel barriers; the doped device is therefore n-type, as was observed.

Chapter 8 References

1. S. Suzuki, C. Bower, and O. Zhou, Chemical Physics Letters **285**, 230-234 (1998).

2. R. S. Lee, H. J. Kim, J. E. Fischer, *et al.*, Nature **388**, 255-7 (1997).

3. Sander J. Tans *et al.*, Nature **393**, 49-52 (1998)

Appendix A.

Experimental Techniques for Thermopower and Thermal Conductivity Measurement

A.1 Measurement of Thermopower

The thermoelectric power of a material is defined as

$$S = \frac{E}{\nabla T}. \tag{A.1}$$

In measuring TEP, one applies a temperature gradient to the sample and measures the voltage which is induced by the temperature difference. Because the geometrical factors for determining the temperature gradient from the temperature difference are the same as those for determining the electric field from the voltage difference, TEP is geometry-independent, and can be calculated by

$$S = -\frac{\Delta V}{\Delta T} \tag{A.2}$$

A stage for measuring thermopower, therefore, must apply a temperature difference to a sample, measure that temperature difference, and measure the voltage across the sample. The stage we built for measurement of TEP is diagrammed below (fig. A.1).

The stage consists of a copper base which has 16 gold pins attached with thermally conducting stycast epoxy. The pins are placed in holes with .100" spacing, so that they fit in a standard chip holder. We made a mount for both the Heli-trans cryostat and a gas flow

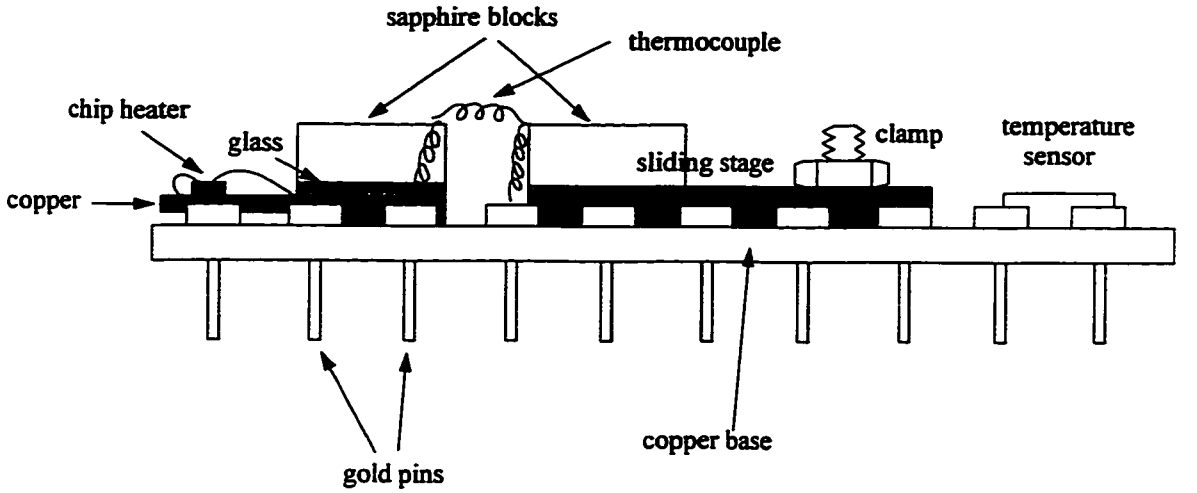

Figure A.1 Stage for Measurement of Thermopower

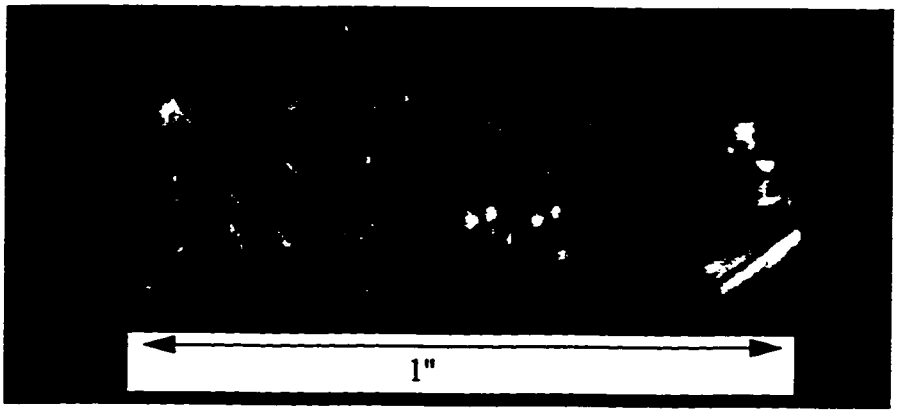

Figure A.2 Thermopower Stage

cryostat to hold these standard stages. On the TEP stage are two sapphire blocks: one is fixed, while the other is on a sliding copper stage, so that the gap between the two blocks can be changed. The fixed block is not attached directly to the base, but sits on a piece of copper and sandwiched between two thin glass cover slips. This arrangement is to allow for the heating of the block: a small chip heater is affixed to the copper sheet, which then heats the sapphire through the upper layer of glass. In this way, the high thermal conductivity of the copper compared to that of the glass ensures that the sapphire will be heated

uniformly. The glass below the copper sheet provides a low thermal conductivity connection to the copper base, so that the stage can be heated, but provides a good enough connection to allow the block to cool quickly when the heater is turned off. The layers are connected with stycast: we had tried to use silver epoxy, which can withstand a higher temperature, but found that it was susceptible to cracking off upon cooling due to the differing thermal contraction of the copper and glass. Stycast is designed for attaching glass to metal (it has an intermediate thermal expansion) and does not crack.

The temperature difference between the two sapphire blocks is measured with a type E (chromel-constantan) differential thermocouple. It is usually advantageous to have a thermocouple with as small a thermal conductance as possible. This minimizes the effect of thermal contact resistance and also ensures that heat is not being drained from the sapphire blocks through the thermocouple. Therefore, we employed two strategies to reduce the thermal conductance. First, the thermocouple is made of thin (.0005") wire. Second, the wire was effectively made longer by coiling it, using a 2 mil wire as a form. The thermocouple wires were bonded together using a spark-bonding technique. This was done by making a set of tweezers with wires soldered to them, which were then attached to a DC power supply set at approximately 12 volts. The thermocouple wires were picked up with the tweezers at the ends, and then touched in an 'X' pattern. With luck, the wires spark bond at the junction and the sections of the wires being held by the tweezers burn off. We found that it was advantageous to then reinforce the spark-bonded junction with silver epoxy or stycast.

The sample is mounted between the two sapphire blocks with silver paint. Carbon nanotube samples, because of their flexibility, could be mounted directly between the

blocks. With fragile samples such as the AC_{60} crystals, on the other hand, differing thermal contraction of the sample and stage can crack the sample when it is cooled; in this case, it is best to connect the sample to one of the blocks with thin bent gold wires to absorb the stress. Care must be taken to ensure that the gold wires have a much higher thermal conductance than the sample, so that the measured temperature drop reflects the temperature drop across the sample. From the sapphire blocks, gold wires are then connected to two pins on the base to measure the voltage.

The gold wires and the sample form a differential thermocouple which can be compared to the type E thermocouple. The thermopower of the sample will then be given by

$$S_{sample} = \frac{\Delta V_{sample}}{\Delta V_{thermocouple}} \times S_{thermocouple} + S_{Au} \qquad (A.3)$$

In principle, it is possible to simply apply a constant temperature gradient as the probe is cooled, and then measure the voltage across the sample to obtain the thermopower. However, this method does not work in practice. One finds that, even with no applied temperature gradient across the sample, one measures a voltage across it, especially when the stage is changing temperature rapidly. This offset is mostly due to the thermopower of the wires connecting the low-temperature stage to the outside. To overcome the problem of voltage offsets, it is necessary to employ some sort of AC technique. The simplest is to stabilize at a given temperature and measure the voltages on the thermocouple and sample with no temperature gradient, and then with a temperature gradient on. This, however, requires constant attention, and is slow, because the temperature must be stabilized at each point. Therefore, we developed a way of doing the measurement in a

continuous fashion.

A.2 'R vs. T with TEP' Software

To measure TEP continuously, we created a LabView program entitled 'R vs. T with TEP', based on the existing 'R vs. T' program. In order to provide a continuously-changing temperature gradient across the sample, a low-frequency (around .002 Hz) ac voltage is applied to the differential heater. The software continuously collects sample and thermocouple voltages, which are usually measured with nanovoltmeters. After collecting a specified number of data points, the software plots V_{sample} vs. $V_{thermocouple}$ and finds the best-fit slope to the data; this slope is then used to calculate the TEP according to equation A.3. Finally, the software saves the collection of raw data points in a separate file, appends the calculated TEP to a master file, and begins to collect a new set of data.

To measure thermopower using the 'R vs. T with TEP' program, the user first configures LabView to measure the voltage of two samples (usually with nanovoltmeters), with the thermocouple as sample 1 and the sample voltage as sample 2 (the order is important here). Figure A.3 shows the settings for the nanovoltmeters (in this case, a Keithley 181 for the thermocouple and a 182 for the sample)

After the samples and temperature measurement are set, the user goes to the 'init TEP' menu, as shown in figure A.4. First, the user chooses an output folder for the data; this is done by writing a *file* with the desired name, which is then turned into a folder. In this folder will be stored the files of raw data, as well as a file entitled 'TEP_data', which contains the master file of the calculated thermopower vs. temperature. Next, a thermocouple data file (which gives the thermopower vs. T of the differential thermocouple) and

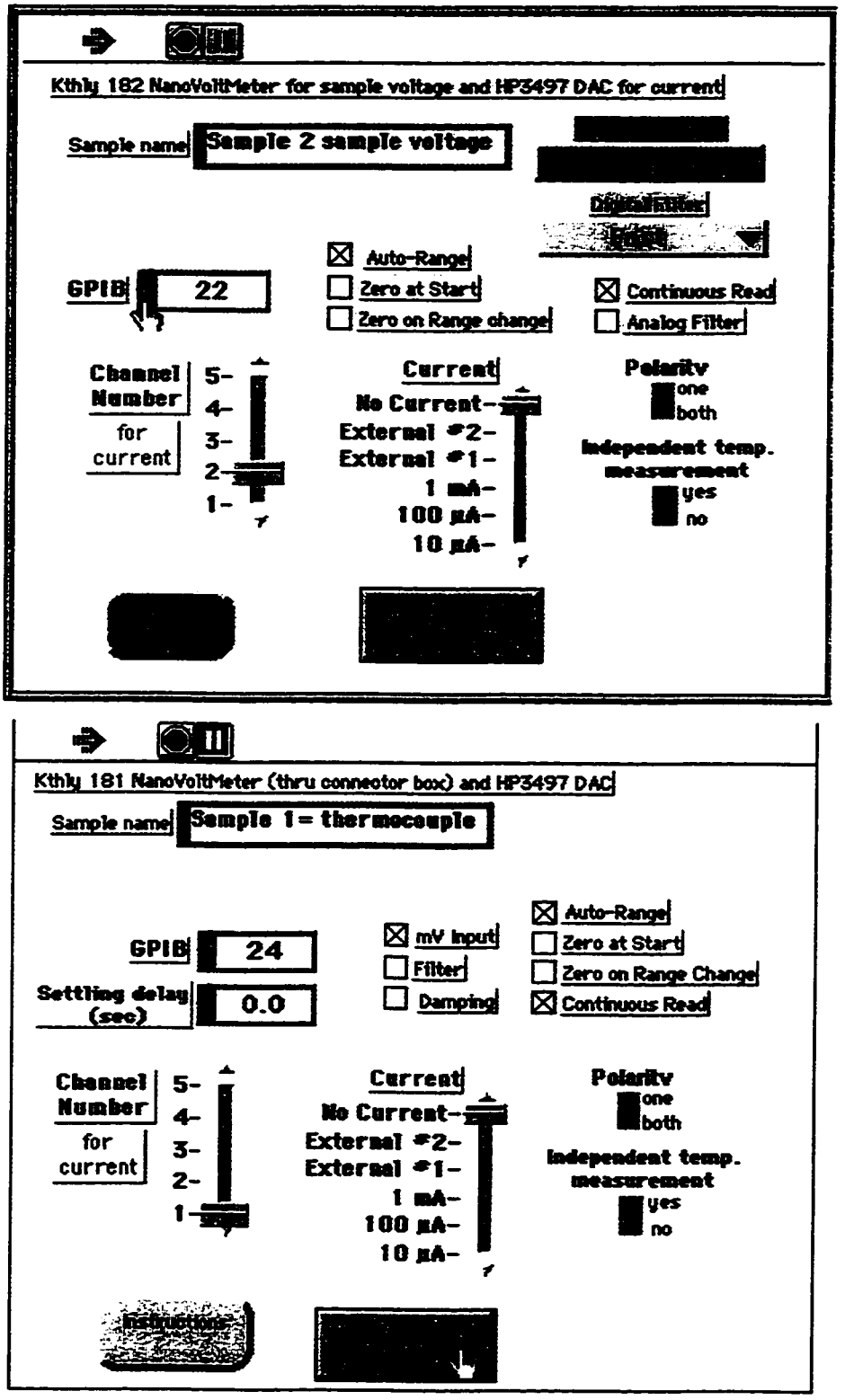

Figure A.3 Nanovoltmeter settings for TEP measurement. The thermocouple voltage is set to sample #1, and the sample voltage is set to sample #2.

a 'gold' data file (which gives the thermopower of the leads to the sample vs. T) are chosen. Finally, the user specifies how many individual voltage data points will be used to calculate each thermopower data point.

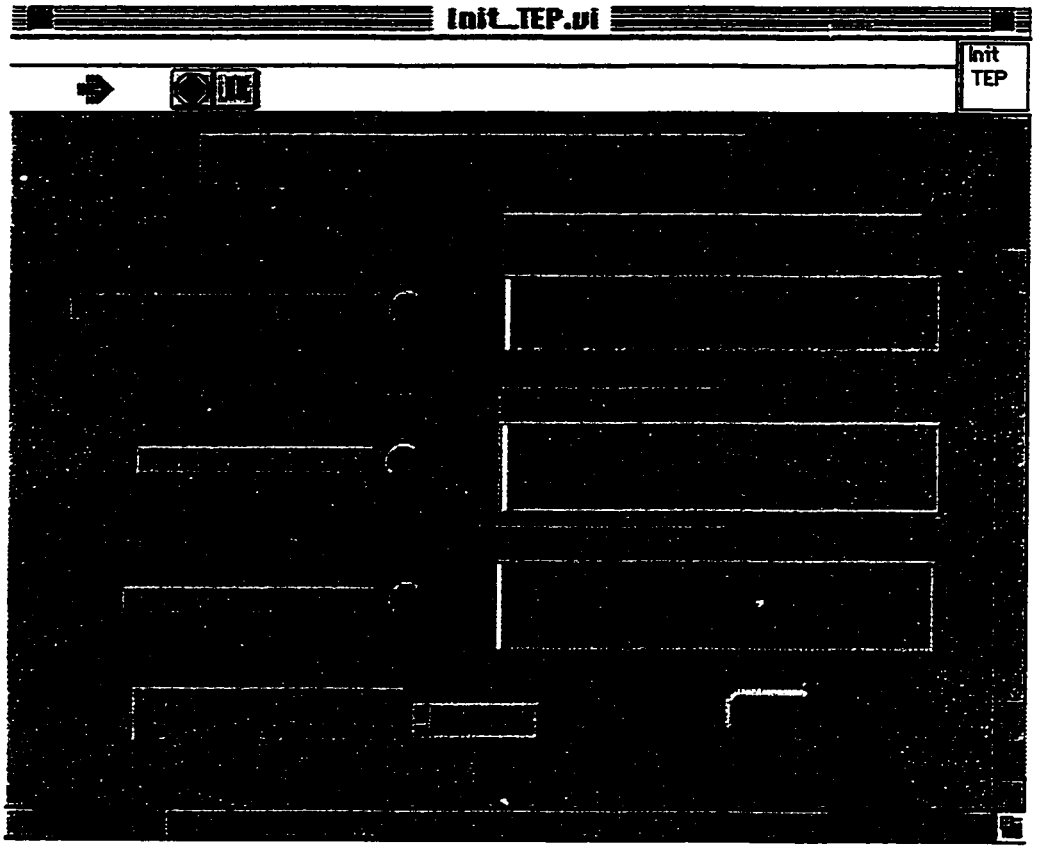

Figure A.4 Initialization of the TEP data-taking parameters

Figure A.5 shows a sample set of TEP data as it is being taken. The thermocouple voltage, set as sample #1, is plotted vs. time in the first graph, while the sample voltage is plotted in the second. When these two sinusoidal voltages are plotted against each other, the result is a straight line (unless the frequency is too high--in that case delays will cause the line to become an ellipse), as shown in the third graph. When the specified number of points per TEP calculation is reached, the program automatically calculates the TEP, saves

the raw data, clears the existing raw data, and starts taking data again.

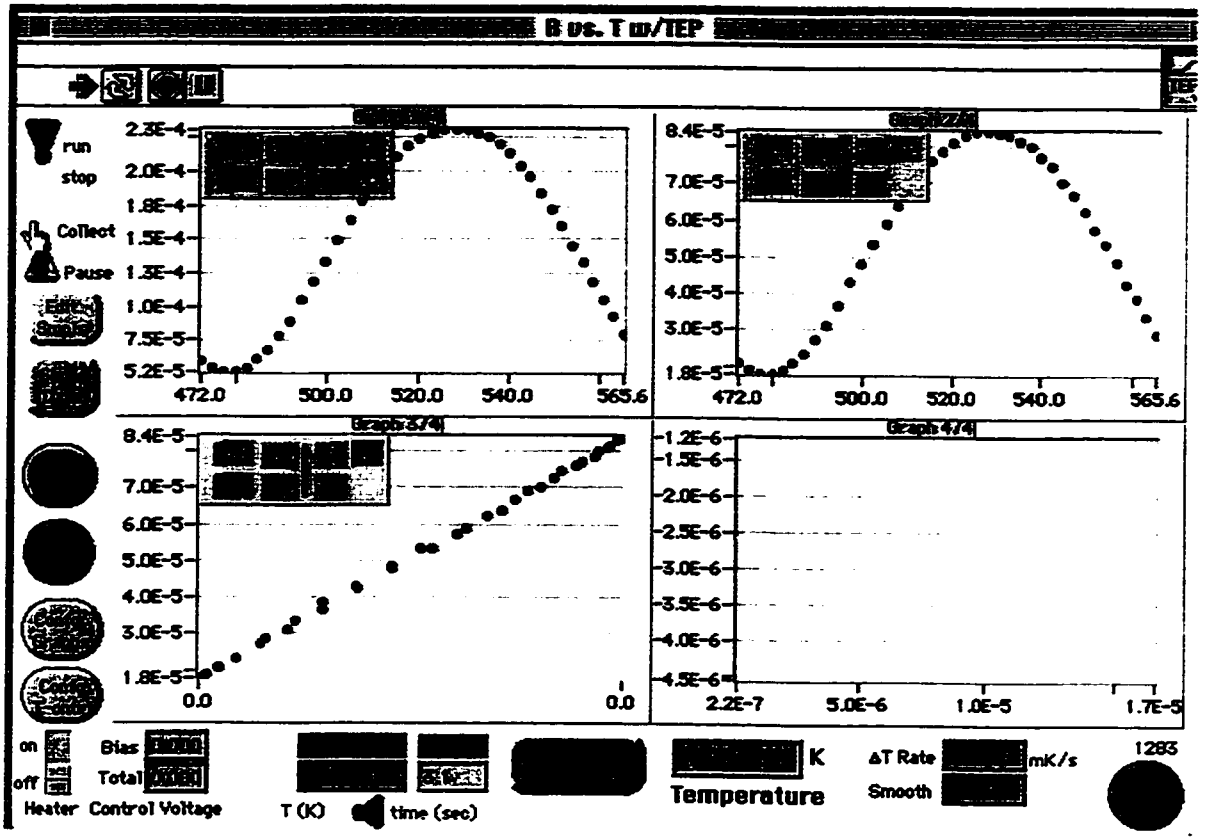

Figure A.5 The 'R vs. T with TEP' vi. Graph #1 shows the voltage on the thermocouple, graph #2 shows the voltage on the sample, and graph #3 shows the sample voltage plotted vs. the thermocouple voltage.

A.3 Measurement of Thermal Conductivity

We have measured thermal conductivity using the comparative method. In this technique, the sample is mounted in series with a constantan rod with known thermal conductivity. Once again, we built a stage based on the modular 'chip' design used for the TEP probe; the stage is diagrammed below. A heater mounted on the constantan rod provides a heat current which flows through the constantan rod and the sample. The setup then can be modeled as a simple series circuit, with the thermal conductivity of the sample

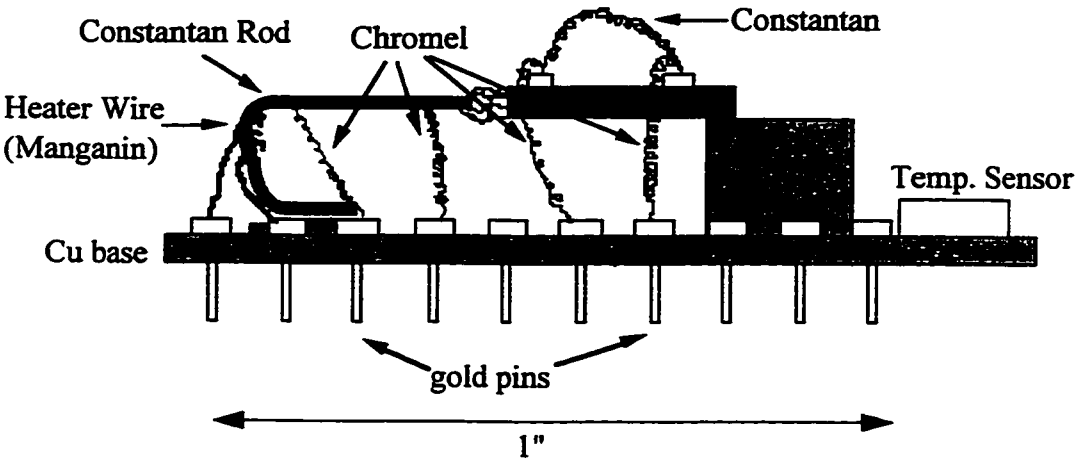

Figure A.6 Stage for Thermal Conductivity Measurement

given by

$$G_{sample} = G_{constantan} \times \frac{\Delta T_{constantan}}{\Delta T_{sample}} \tag{A.4}$$

In order to measure the temperature drop across the constantan rod, chromel wires are spark-bonded to it, so that the three parts form a type E differential thermocouple. Likewise, the temperature drop across the sample is measured by attaching a differential thermocouple to it. Mounting the thermocouple is usually the most difficult part of preparing the sample. First, the thermocouple itself must be spark-bonded and bent into the right shape. Then, the thermocouple must be attached to the sample so that they have good thermal contact but are electrically insulated. We found that there were two good ways to do this. One was to coat the thermocouple junctions with stycast, and then attach (either with stycast or silver paint) the stycast to the sample. The other was to attach very small chips of sapphire to the sample with silver paint or epoxy, and then mount the thermocouple to the sapphire with silver paint or epoxy. Mounting the sample on the stage is also difficult: it is almost always necessary to provide stress relief by attaching the sample to

either the constantan rod or the heat sink with bent annealed gold wires.

Since the comparative method assumes an equal heat flow through the sample and the constantan rod, it is important to minimize all heat leaks. To minimize conduction through the thermocouples, they were made out of .0005" wire, and coiled (using a .002" wire as a template) to maximize their length. Finally, a small radiation shield was attached to the chip to minimize the effects of any 'hot' spots in the measurement probe.

Thermal conductivity can, in principle, be measured using the same scheme as was used for thermopower. In fact, we used the same 'R vs. T with TEP' program. There are only a few differences in implementing the software, as listed below.

1. The sample thermocouple must be measured as sample 1, and the constantan rod thermocouple as sample 2.
2. Instead of comparing to a known thermopower, we are comparing to a known thermal conductivity. Therefore, a file containing the thermal conductivity of the constantan rod vs. temperature is used in place of the thermocouple file.
3. There is no additive factor in calculating the thermal conductivity. Therefore, a file with all zeros is used in place of the 'gold' thermopower file.

In actually doing the measurement of thermal conductivity, it is unfortunately not possible to employ a quasi-AC technique as was done for the thermopower. The thermal time constants of the system are too long, and because the sample and rod are at different parts of the thermal circuit, they can lag each other by many seconds, and even display oscillatory behavior. We found that the best way to get a good measurement was to do things manually. First, the probe is stabilized at a given temperature, or programmed to ramp slowly enough that the offsets in the nanovoltmeters change slowly (the last digit

should only change at a rate of a couple Hz.). Next, a given number of data points are taken with the differential heater off, to measure the fixed offsets in the thermocouple voltages. Then the differential heater is turned on, and, with the data collection paused, the system is again allowed to equilibrate. This usually takes at least a minute or more at high temperature, less at low T. At this point, a number of data points are again taken. Finally, the heater is turned off and the system is allowed to re-equilibrate, so that another set of background points can be taken. We usually used a 5-10-5 scheme, taking two sets of five background points (so that any linear drift in the offset will average out) and ten points with the heater on. Figure A.7 shows the raw data for a typical thermal conductivity measurement. Graph 1 shows the voltage of the thermocouple across the sample vs. time, showing five points taken with the heater off, a pause of thirty seconds, ten points taken with the heater on, another pause, and then five more points taken with the heater off. Graph 2 shows the same data for the thermocouple across the constantan rod, while graph 3 shows the two data sets plotted against each other; the program will fit a straight line to the data and use the slope to calculate the thermal conductance of the sample.

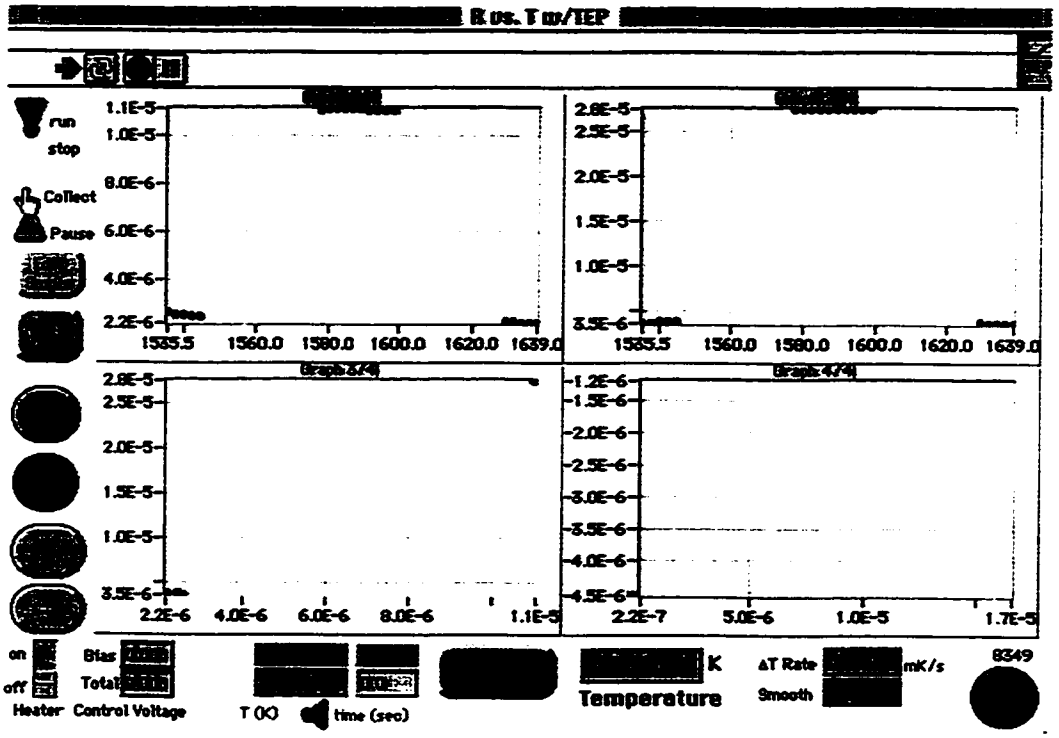

Figure A.7 The 'R vs. T with TEP' vi, used for measurement of thermal conductivity. Graph 1 shows the voltage of the sample thermocouple vs. time, graph 2 shows the constantan rod thermocouple voltage, and graph 3 shows the two voltages plotted against each other. The user must stop the data taking to wait for the system to equilibrate while the heater power is turned on or off.

Appendix B.-

Synthesis of Isotopically-Enriched C_{60}.

B.1 Motivation

Nuclear Magnetic Resonance (NMR) is a powerful tool for probing the electronic and crystal structure of materials. In particular, NMR has helped illuminate many of the aspects of the AC_{60} materials, such as the low-temperature antiferromagnetic ordering and the possible differences in structure between KC_{60} and the Rb and Cs materials. Unfortunately, NMR requires nuclei with a net magnetic moment, which in carbon means carbon-13. Natural-abundance carbon contains approximately 1% ^{13}C, which means that signal is coming from only 1% of the carbon in the material. For many measurements, particularly on small samples, this low level of signal is not sufficient. Increasing the collection time is one possibility, but doing so also increases the amount of noise present, so that the signal-to-noise ratio increases only as the square root of the collection time. Increasing the isotopic enrichment of the material, on the other hand, increases the signal without increasing the noise, so the signal-to-noise level rises linearly with enrichment. Comparing the two strategies, we see that enrichment is generally the more effective strategy: increasing the enrichment by a factor n is equivalent to increasing the collection time by a factor n^2.

Because our group had experience in and equipment for the synthesis of isotopi-

cally-enriched C_{60}, we entered into collaboration with two NMR groups, that of Henri Alloul at the University of Paris and that of Alex Pines at Berkeley. The synthesis work for the Pines group was done in collaboration with Ben Gross.

Our group had previously developed a method for producing high-purity 99% ^{13}C-enriched material for studies of the carbon isotope effect in Rb_3C_{60}. To burn the ^{13}C material in the arc chamber, it first had to be turned into small rods which were strong enough to hold in place. This was done by a hot vacuum pressing technique, in which a small amount of ^{13}C powder, enclosed in a quartz tube, was pressed between two tantalum rods under vacuum; a progressively higher electrical current was passed through the powder until it fused into a small rod. This method was highly effective, but had three major drawbacks for the production of the relatively larger amounts of material necessary for the NMR experiments. First, small amounts of impurities would react with the quartz tube at high temperatures, etching the quartz and making extraction of the pressed rod highly difficult. Batches of ^{13}C had to be specially ordered and screened for impurity concentration. A second problem was that the pressed rods were quite small, having a weight of less than one gram, and took a long time (two hours or more) to press. This made synthesis of large amounts of enriched C_{60} prohibitively time-consuming. Finally, we wanted to arc the enriched material and then 'recycle' the soot that was left after fullerene extraction, so that we could make maximum use of the expensive ^{13}C. The hot pressing method did not work for this. The soot was not highly conducting upon initial pressing, but when gently heated small areas would suddenly increase in conductivity; these areas would heat rapidly and release large amounts of trapped gases. In spite of the dynamic vacuum applied

to the system, the apparatus would explode at this point.

B.2 Production of Rods of Enriched ^{13}C

As was discussed above, the main difficulty in synthesizing enriched C_{60} is to produce dense, strong rods of enriched material. The easiest method is to simply drill a hole in a 1/4" graphite rod and fill the hole with ^{13}C powder. This has a number of drawbacks. First, it is difficult to pack the powder to a high enough density. The best method for increasing the density proved to be mixing the powder with solvent (acetone or toluene) and then pressing the mixture into the graphite rod, either mechanically or by centrifugation. In the process, most of the solvent would be forced out of the powder through the porous graphite rod, resulting in a densely packed powder in the hole. Nevertheless, this method still proved to be less than ideal. The density achieved was still significantly lower than that of the surrounding graphite, and the enriched powder did not form C_{60} as well as the hard graphite rod, presumably because the powder has a tendency to fly out of the rod in larger particles before vaporizing.

In an effort to press rods only out of the desired material, a number of methods were tried. Hard pellets could be formed by a three-step process of pressing in a metal die, cold isostatic pressing (in which the sample is enclosed in a rubber balloon and pressed in oil to 170,000 psi), and then hot isostatic pressing (at 1400 °C in 20,000 psi of Argon). However, it proved difficult to make large rods by this method, because rods produced in the first step would break into pieces too easily. In addition, the method was quite cumbersome, and in the end could not produce large rods. Pressing using binders such as

polyethylene glycol proved ineffective as well. One successful method was to mix the ^{13}C into a graphite cement which could then be formed into rods or packed into thin tubes of graphite. These rods, when cured, were quite strong. However, it was difficult to get a high enrichment (>5%) with this method, because very little ^{13}C powder could be mixed in with the graphite cement. In addition, the rods had to be sintered at high temperature before arcing (this was done in the arc chamber by passing a large current through the rod under dynamic vacuum) to burn off the binders in the cement. These binders, when burned, tended to contaminate the chamber and generally muck up the process.

Because of all of the difficulties with the above methods, we finally returned to the hot pressing method to produce large enriched rods. However, because obtaining rods with the highest possible purity was not important, we were able to modify the setup to eliminate the associated problems mentioned previously. Figure B.1 diagrams the apparatus used to press large carbon rods. Carbon powder (it should be finely ground using the planetary ball mill at LBL) is packed into a 6" long 3/8" diameter graphite rod with a 1/4" hole drilled down its center, first by hand and then, to achieve the maximum compression, using gentle pressure on the hydraulic press. The 3/8" inch graphite rod is then machined down (plug the ends so that the powder does not fall out) to an O.D. of 5/16"-- a thicker graphite rod will not reach a high enough temperature for the carbon power to sinter into a rod. The graphite rod is then placed into a 3/4" quartz tube. The quartz tube is held by vacuum feed-thrus which allow two 1/4" tantalum rods to be inserted into the graphite rod to press the carbon. The apparatus is then mounted on a bathroom scale on the hydraulic press. Current leads from an arc-welder power supply are attached to the copper bases, and a rough vacuum line (with a thermocouple gauge) is attached to the pumping port.

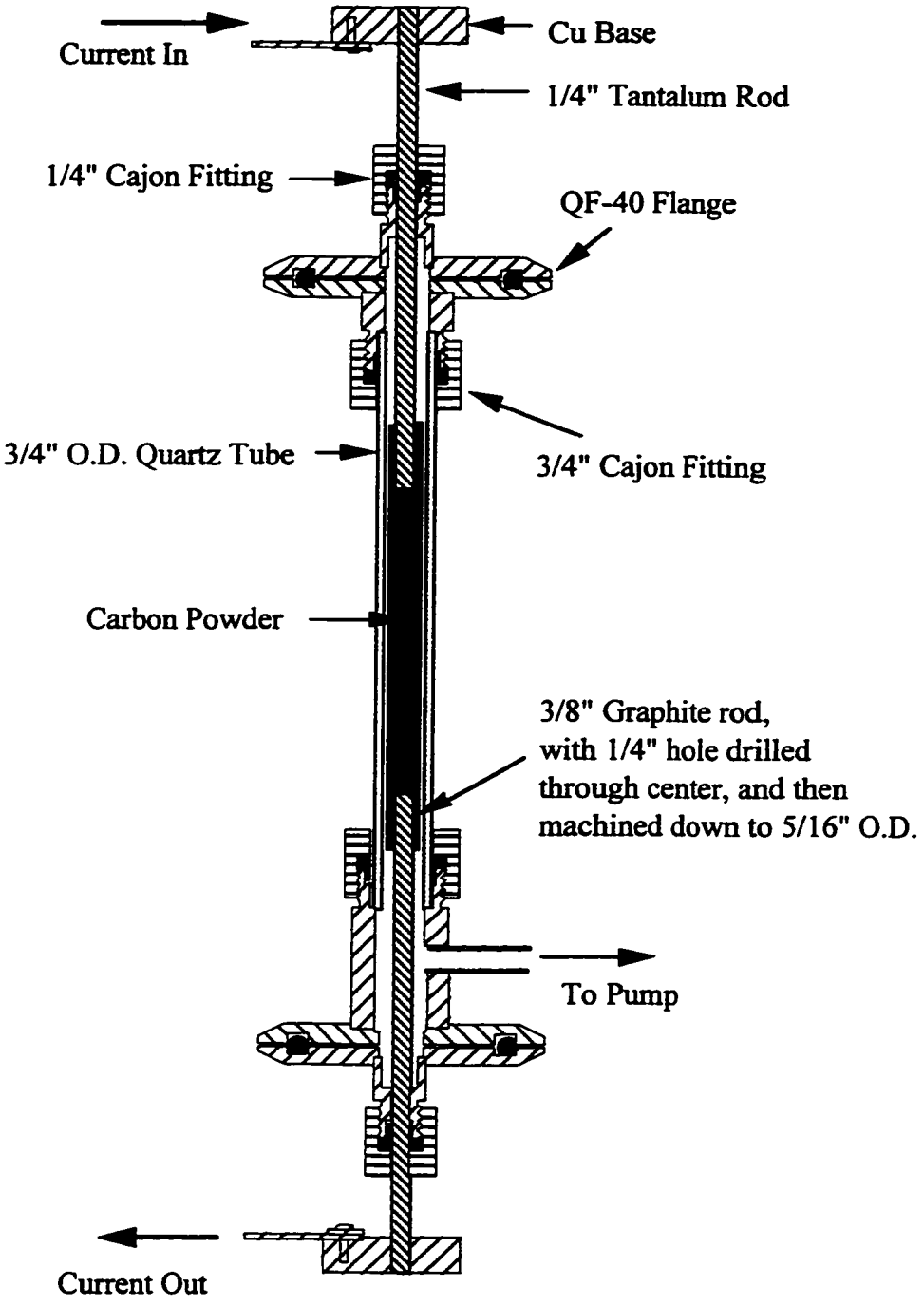

Figure B.1 Apparatus for hot vacuum pressing of carbon

The system is evacuated to 1-200 mtorr, at which point 80 pounds of force (measured with the bathroom scale) is applied. The carbon powder is then heated by passing a current through the powder and graphite rod. The current should be set on the lowest possible set-

ting first, turned off when the pressure rises above a few hundred mtorr, and then turned back on when the pressure drops. The heating cycle should be repeated with gradually increasing current, until by the final cycle the current should reach >200 A, and the graphite rod will glows bright white. As the carbon powder compresses, the force on the scale will drop, and should be maintained using the hydraulic press. Figure B.2 shows a picture of the setup before heating and then during the final heating stage. After the final heating stages, the pressure should be reduced and the heating repeated in order to anneal the pressed rod. Finally, the sample is removed from the graphite sheath, either by pressing or by carefully cutting away the graphite with a razor blade.

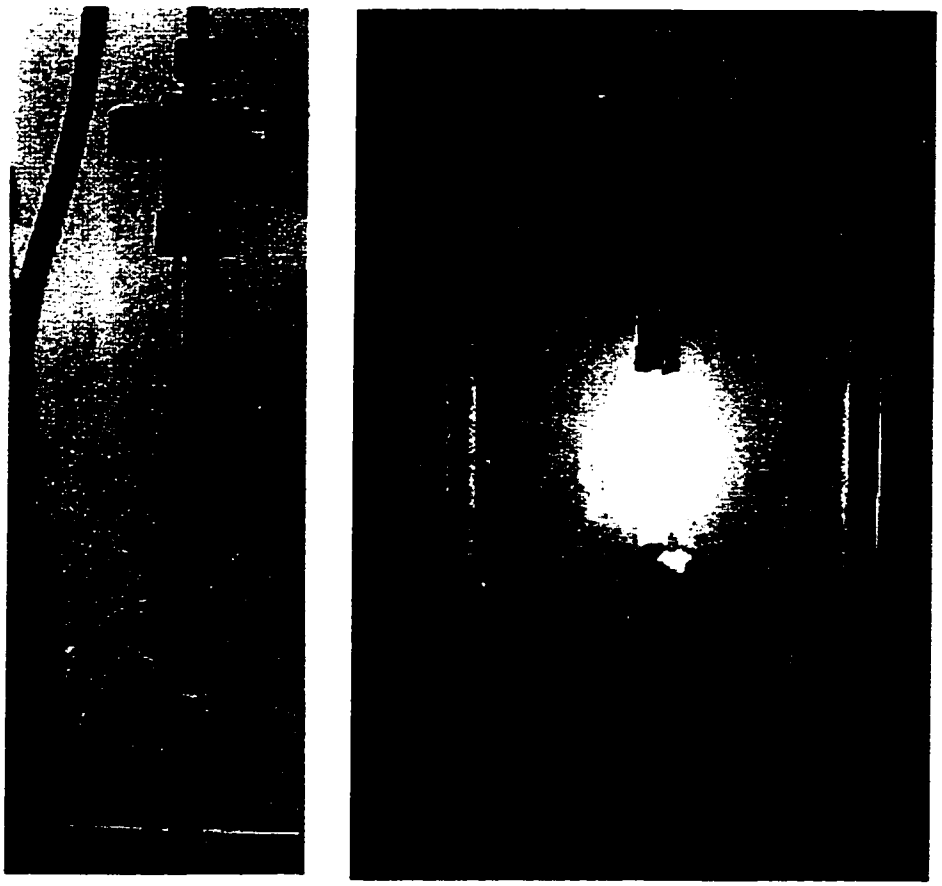

Figure B.2 Apparatus for hot-pressing carbon. Left, at room temperature; right, at maximum heating current (>200 A)

Using the hot-pressing method, we have been able to make carbon rods as long as three inches, with a mass of as much as four grams. In addition, soot from the arc chamber can be re-used after fullerene extraction. The problem of reaction of impurities with the quartz tube is also removed--the quartz is not in direct contact with the carbon, and therefore does not impede the removal of the pressed rod.

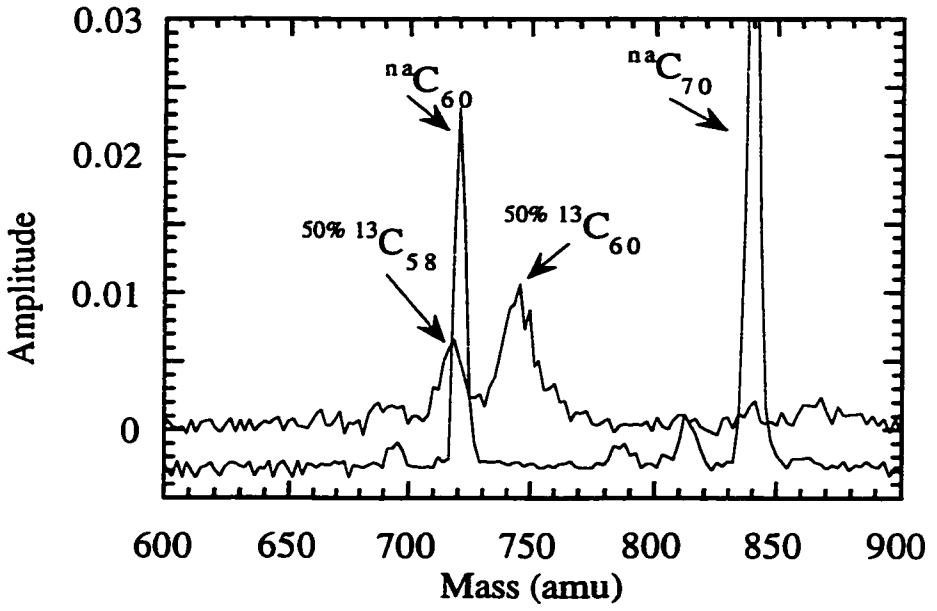

Figure B.3 Mass spectrum of natural abundance C_{60}/C_{70} and enriched C_{60}

Figure B.3 shows a mass spectrum of the extracted crude fullerene soot from a typical synthesis run. This sample was synthesized from a 50/50 mixture of ^{13}C and natural-abundance graphite powder, which were finely ground and mixed in a planetary ball mill. The natural-abundance C_{60} peak appears at 720.6 (due to the existing ^{13}C in natural abundance carbon), while the enriched C_{60} peak appears at 749.5. This corresponds to 29 ^{13}C

atoms per ball, in agreement with the expected enrichment. Other peaks (such as the one labeled C_{58}) in the spectrum of the enriched material are due to fragmentation of the ball due to the laser; a higher laser power was required to obtain the spectrum for the enriched run, and thus resulted in more fragmentation.

IMAGE EVALUATION
TEST TARGET (QA-3)

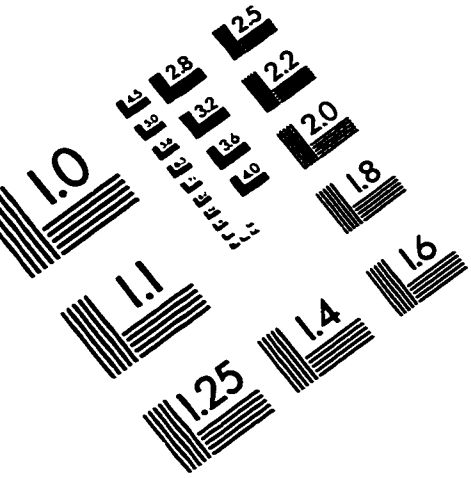

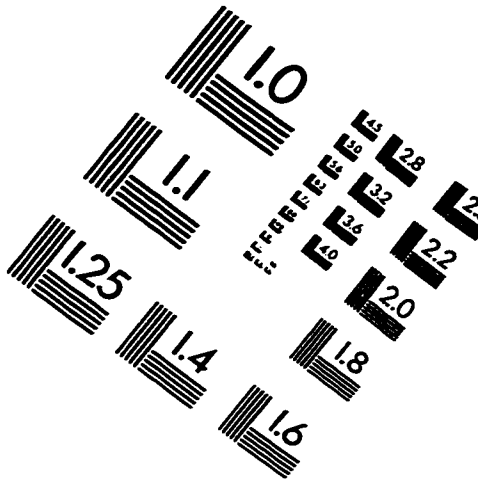

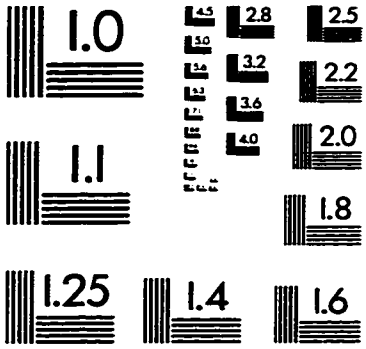

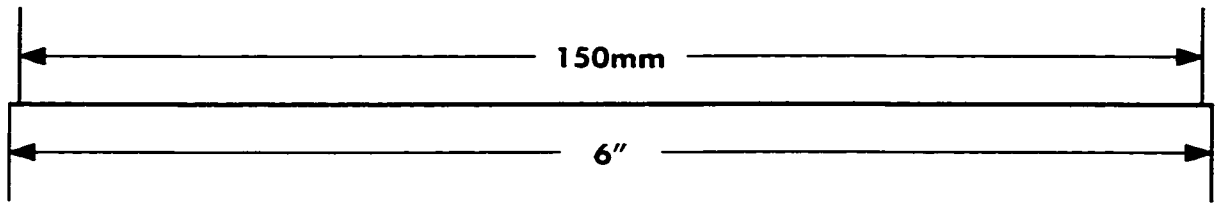

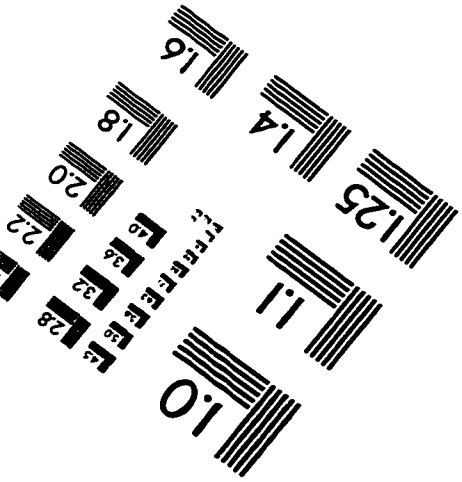

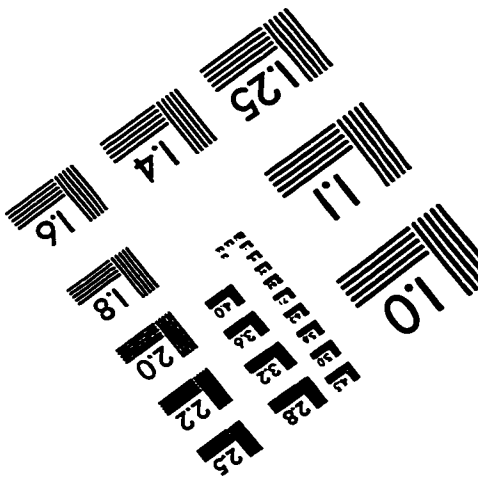

APPLIED IMAGE, Inc
1653 East Main Street
Rochester, NY 14609 USA
Phone: 716/482-0300
Fax: 716/288-5989